ABSTRACT

Title of Document: DEVELOPMENT OF NANO-PATTERN
                                           RECOGNITION AND CORRELATION
                                           TECHNIQUE FOR DEFORMATION
                                           MEASUREMENT OF NANO-SCALE
                                           STRUCTURES

                                           Hongbo Bi, Doctor of Philosophy, 2008

Directed By: Professor Bongtae Han, Mechanical Engineering

An imperative need exists for deformation data from interconnects of silicon devices. The need for nano-scale measurements becomes more urgent as the interconnect technology approaches the 50 nm node and beyond. The reliability of devices is determined largely by thermal and mechanical deformations of interconnect layers during manufacturing and operation. These are inferred by computational analysis, but informed physical analysis is vital to measure the variables and to guide and verify the computations. Deformation measurements are needed urgently in the nanometer range. What is needed is in-plane displacement measurements that are accurate within a fraction of nanometers, together with sub-micron spatial resolution.

In recent years, several techniques have been proposed to document nano-scale deformations. They include electron-beam moiré (EBM), nano-scale moiré interferometry, SEM/TEM/AFM digital image correlation (DIC), and speckle interferometry with electron microscopy (SIEM). None of the existing techniques

provide both the accuracy/sensitivity (sub-nanometer) and spatial resolution (sub-micron), which are required for the analysis of nanostructures.

The objective of this thesis is to develop a new deformation measurement technique to cope with the limitations of each existing technique: A hybrid method is proposed to achieve the goal. The proposed method called *Nano-Pattern Recognition and Correlation Technique* (N-PRCT) uses regularly oriented nano-scale structures that are fabricated on the surface of the specimen. After obtaining the SEM pictures of patterns on the region of interest before and after loading (deformation), the conventional low-pass filter combined with a de-blur filter (Wiener Filter) are applied to eliminate the noise during SEM imaging effectively.

A unique practice of E-beam lithography is proposed and implemented to fabricate regularly oriented patterns required for the N-PRCT technique using PMMA as an E-beam resist. The proposed scheme utilizes the standard SEM for imaging to fabricate the patterns without the need of specially designed E-Beam lithography system, which makes the implementation of N-PRCT practical. Yet, the proposed procedure can produce gauge lengths (approximately 150 nm) than those produced by a commercial E-beam lithography system

The proposed method is used to determine the thermally-induced deformations of a passivation layer in a flip-chip package. The regular patterns (115 nm in diameter) are produced on the polished cross-section, and the package is subjected to a thermal loading inside SEM using a specially designed thermal conduction stage. Thermal deformations with the displacement measurement accuracy of less than 0.1 nm are obtained in a field of view of 7 μm. The results

show a shear strain concentration at the interface between the passivation layer and the adjacent metal pad.

DEVELOPMENT OF NANO-PATTERN RECOGNITION AND CORRELATION TECHNIQUE FOR DEFORMATION MEASUREMENT OF NANO-SCALE STRUCTURES

By

Hongbo Bi

Dissertation submitted to the Faculty of the Graduate School of the
University of Maryland, College Park, in partial fulfillment
of the requirements for the degree of

Doctor of Philosophy
2008

Advisory Committee:
Professor Bongtae Han, Chair
Professor Abhijit Dasgupta
Professor Patrick McCluskey
Professor Peter Sandborn
Professor Sung Lee

Acknowledgements

Table of Contents

List of Tables

List of Figures

Chapter 1: Introduction

1.1 Motivation/Objective

Reliability analysis of microelectronics devices is the ever-existing effort for electronic device manufactures. The information obtained from stress/strain analysis and life cycle prediction is to be used to guide and optimize the electronic device design and manufacturing process. Due to the complex mechanical/thermal loading and boundary conditions, simplifications and uncertainties cannot be completely avoided in computational modeling methods [1-3]. Therefore, experimental techniques are highly required; these techniques should be able to provide accurate results for stress/strain studies for microelectronic devices. Moiré and microscopic moire interferometry [4-11] has been well developed in the past decades and successfully used to document the deformation caused by temperature change or/and mechanical loading in microelectronic devices.

Along with the efforts to enhance the performance of microelectronic devices (i.e., faster speed/higher clock frequency), smaller feature sizes of transistors and higher circuit density as well as new materials are being pursued. Numerous studies to characterize the intrinsic mechanical properties of materials, including material and interfacial strength, have been conducted in recent years. Yet it is not known how much deformation the new microelectronic devices will experience during manufacturing and operation. The critical questions are reliability and failure. The physical deformation information is crucial to guide the device structure design and the material selection.

Deformation measurements are needed in the nanometer range to address the above issue. The need for nano-scale measurements becomes imminent as nano-scale components and interconnects are realized in actual devices.

In recent years, several techniques have been proposed to document nano-scale deformations. They include electron-beam moiré (EBM) [12-16], SEM/TEM/AFM digital image correlation (DIC) [18-40] and speckle interferometry with electron microscope (SIEM) [41-42], etc.

However, none of the above techniques can provide both the accuracy/sensitivity and spatial resolution that are required for nano-scale displacement measurement. A new full-field in-plane displacement measurement technique for nano-scale structures with measurement accuracy/sensitivity of sub-nanometer on a few microns length scale is required. This is the motivation of this dissertation.

1.2 Literature review: Existing Techniques

In recent years, several techniques are proposed to document the deformation required for nano-scale structures. In this section, these techniques and their limitation are discussed.

1.2.1 Electron Beam Moiré

Electron Beam Moiré (EBM) was first proposed by Dally and Read [12, 13] to provide high spatial resolution beyond optical microscopes using visible light, and

later practiced by other researchers [14-16]. It is basically an in-plane geometric moiré technique using the scanning electron microscope (SEM).

Moiré fringes are formed by the superposition of two amplitude gratings, each of which is comprised of opaque bars and clear spaces. The relationships between the moiré fringes and grating lines can be determined simply by geometry [17]. For the case of pure rotation, the shaded triangle in Figure. 1-1a gives, for small angles, $g/2 = \theta G/2$, where the grating pitch g and the fringe pitch G are defined in the figure. Thus, for small pure rotations,

$$G = \frac{g}{\theta} \tag{1}$$

In terms of frequency, the relationship is

$$F = f\theta \tag{2}$$

(a)   (b)
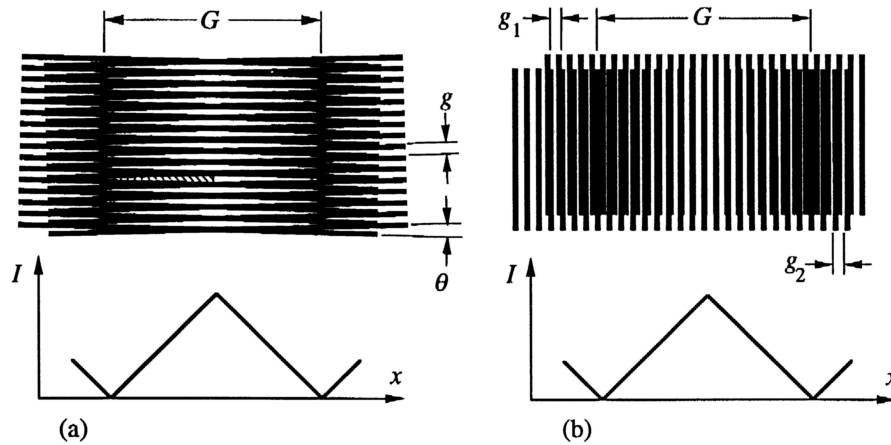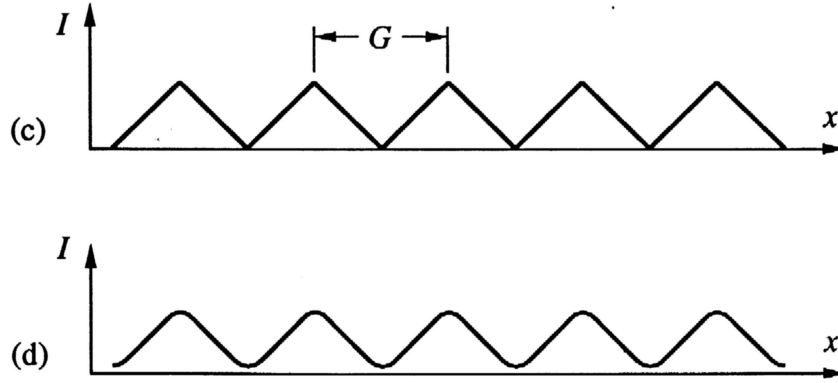
Figure 1-1 (a) Illustration of Moiré fringe caused by pure rotation (b) Illustration of Moiré fringe caused by frequency difference (c) Moiré fringes triangular intensity distribution when the emergent light is averaged over the pitch of the coarser grating. In (d), the rounding is caused by averaging over several pitches. [17]

Note that the fringes of pure rotation (Figure 1-1a) lie perpendicular to the bisector of angle θ, or nearly perpendicular to the lines of the gratings.

For pure extension (Figure 1-1b) there is one more line in the finer grating than in the coarser one, for each moiré fringe. Thus, the pitch of the moiré fringes is given by

$$G = ng_2 = (n+1)g_1 \tag{3}$$

where n and g_2 are the number and pitches of the coarser grating, respectively, that fall within G; $n+1$ and g_1 are the number and pitches of the finer grating, respectively, that fall within G. By eliminating n this reduces to

$$\frac{1}{G} = \frac{1}{g_1} - \frac{1}{g_2} \tag{4}$$

4

and in terms of frequency, the relationship is

$$F = f_1 - f_2 \qquad (5)$$

where f_1 and f_2 are the frequencies of the finer and coarser gratings, respectively. The fringes of pure extension lie parallel to the grating lines.

In practice of the in-plane geometric moiré, one of the gratings is fixed in space (called "reference grating"), and the second grating deforms together with the specimen (called "specimen grating"). It is to be noted that the initial frequency of the specimen grating is identical to that of the reference grating. Then the displacement can be determined from the fringe orders by the following simple relationship

$$U = \frac{1}{f} N_x \ , \qquad V = \frac{1}{f} N_y \qquad (6)$$

where U, V are the displacement in the x and y directions; N_x, N_y are the corresponding fringe orders; and f is the frequency of the reference grating. In the fringe patterns, the contour interval is $1/f$. The sensitivity is its reciprocal (i.e., the number of fringes generated per unit displacement). Consequently, the sensitivity is limited by the number of lines and the E-beam moiré was proposed to cope with the limitation.

The E-beam moiré uses a small diameter beam of electrons (100 to 200 nm) to sensitize a several hundred nanometers thick layer of electron resist [13]. The line patterns are produced by etching the sensitized resist. Figure 1-2 shows an example of specimen grating used in E-beam moiré. The frequency of a specimen grating, f_g,

is determined by the scanning frequency and scanning area per scanning frame [14]. It can be expressed as

$$f_g = \frac{number \cdot of \cdot scanning \cdot lines}{height \cdot of \cdot scanning \cdot area} \times magnification \qquad (7)$$
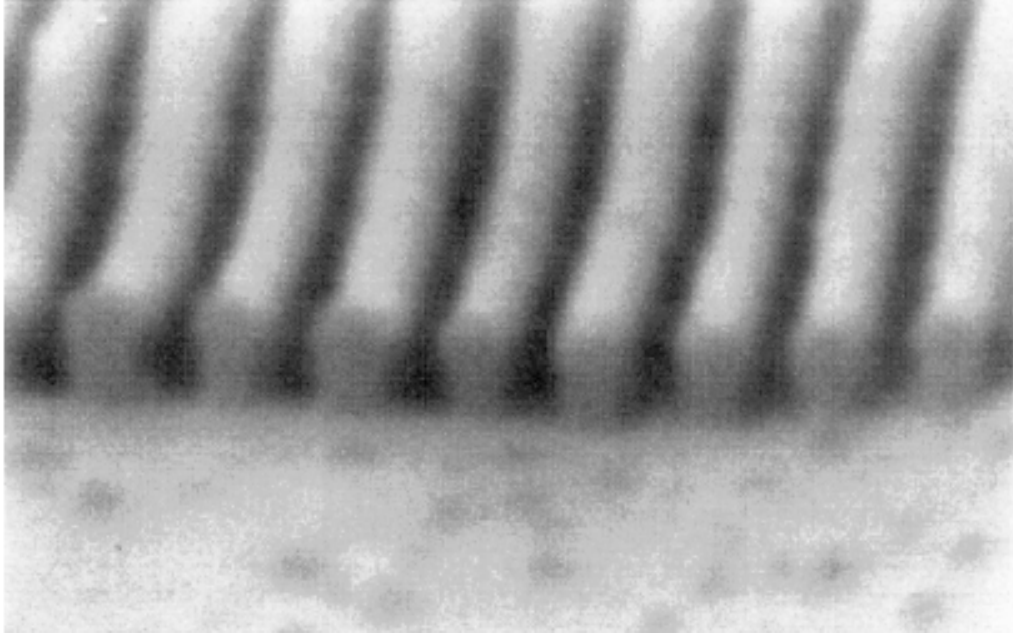
Figure 1-2 SEM image of lithographic specimen grating [14]

Moiré fringes appear when the specimen grating (line arrays) is observed in the scanning electron microscope. The raster scanning frequency of SEM is the same as that of line arrays produced on the specimen. The electron beam scanning acts as the reference grating and it interacts with the specimen grating to form moiré fringe patterns. Then the displacement can be determined by Eq. 6.

Since the E-beam moiré fringe is produced by the spatial frequency mismatch between the specimen grating and the raster scanning lines, it will be affected by the diameter of the electron beam and the detailed topography of the lines on the

specimen.   The current E-beam lithography technique can readily offer a specimen grating with a frequency of 5,000 lines/mm [13,15], providing a contour interval of 200 nm/fringe in a region of interest of approximately 30 μm by 30 μm [12-14]. The sensitivity is substantially lower than that required for nano-structural deformations.

Although specimen gratings with a higher frequency (higher than 10,000 lines/mm) are possible in theory, it would be extremely difficult to make a uniform grating with such a high frequency due to the instability of the E-beam.   It is to be noted that non-uniformity of the grating will produce undesired fringe patterns at the non-loading condition.   In addition, a smaller diameter of E-beam required for the high frequency grating fabrication results in a higher exposure dose, which can damage or burn the resist layer and leave an ambiguous grating.   The ambiguous specimen grating produced by the extreme exposure dose is shown in Figure 1-3.
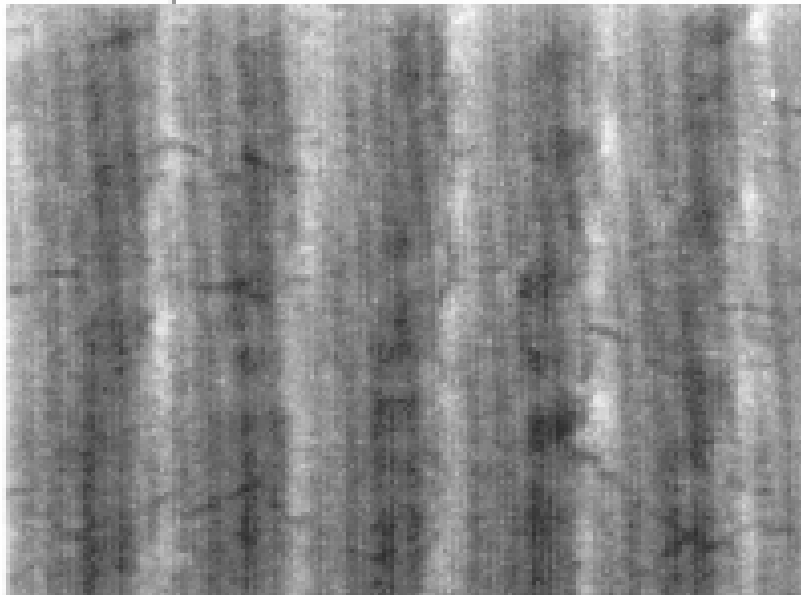
Figure 1-3 Specimen grating due to higher dose [14]

Like the conventional in-plane geometric moiré, a specimen has to be rotated by 90° to obtain both U and V displacement fields. The exact 90° rotation is not possible in practice, which results in errors in shear strain measurement. In addition, the technique requires a continuous grating layer on the specimen surface, which requires a thicker resist layer. The technique actually measures the deformation of the surface of the grating although the deformation of the surface of the specimen is desired. This difference can be significant when the specimen grating is not sufficiently thin compared to the size of underlying structures of interest [17].

1.2.2 AFM/STM/SEM Digital Image Correlation Technique

Digital image correlation (DIC) has become an widely accepted method for measuring in-plane displacements and displacement gradients (strain) [18-20]. The DIC technique is an amplitude-based measurement technique and relies on the existence of a distinct grayscale pattern in a region. The region is composed of a subset of pixels around a location where deformations are to be computed. DIC is performed between subsets in the reference configuration and their counterparts in the deformed configuration. Correlation determines the displacement of center point of each subset. Displacement information can be obtained when all of the matching subset pairs are found.

1.2.2.1 Fundamentals of Digital Image Correlation

The objective of image correlation is to find the matching of one subset from an image of an object's surface before deformation/loading to a subset in an image of the object's surface taken after deformation/loading. And this point to point mapping from the un-deformed (reference) image to the deformed image can produce the displacement map of the object's surface. In order to provide features for the matching process, the surface of the object must have "random" patterns that produce varying intensities of diffusely reflected light from its surface.

The imaging process of the imaging system converts the continuous intensity field reflected from the surface $O(X,Y)$ into a discrete field $I(X,Y)$ of integer intensity levels. In a charge-coupled device (CCD) camera, this transformation occurs when the light incident on a sensor (commonly known as a pixel) is integrated over a fixed time period. The rectangular array of sensors in a CCD array converts the continuous intensity pattern into a discrete array of integer intensity values. This conversion process for analog single to digital signal includes following functions [19].

(a) $O(X,Y)$ denotes the continuous intensity pattern for the un-deformed object,

(b) $O'(X,Y)$ is the continuous intensity pattern for the deformed object,

(c) $I(X,Y)$ is the discretely sampled intensity pattern for the un-deformed object and

(d) $I'(X,Y)$ is the discretely sampled intensity pattern for the deformed object.

The process of deformation in two dimensions is shown schematically in Figure 1-4 [19].
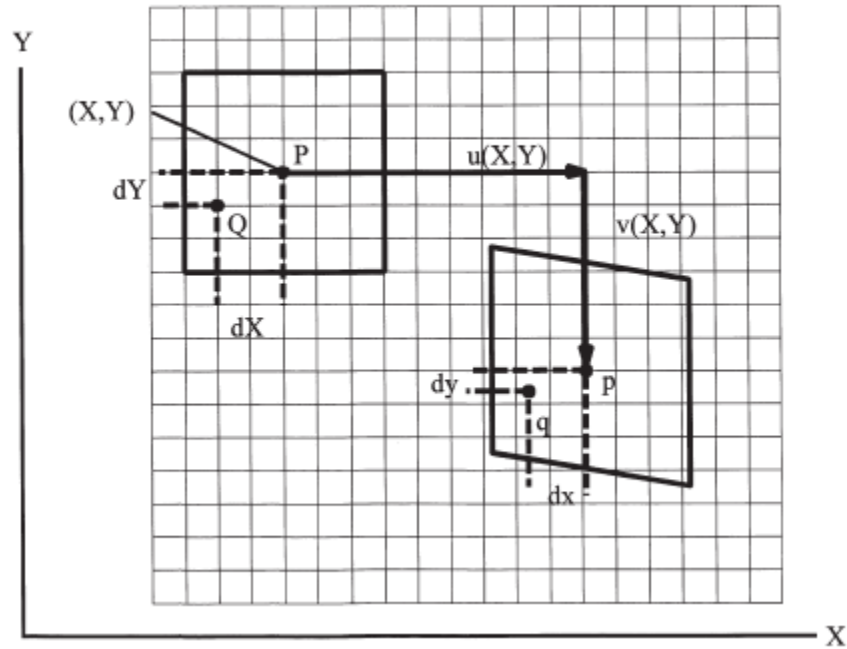
Figure 1-4 Schematic of deformation process in two dimensions [19]

It is important to note that the basic principle of the digital image correlation method is that points in $I(X,Y)$ and $I'(X,Y)$ are assumed to be in one-to-one correspondence with points in $O(X,Y)$ and $O'(X,Y)$, respectively. Thus, one can use $I(X,Y)$ and $I'(X,Y)$ to determine the displacement field for the object $O(X,Y)$ and $O'(X,Y)$.

In order to determine the point to point matching from the images before and after deformation/loading, segmenting the image before loading into small subsets is required. (X,Y) is the center coordinates of subset in the image before deformation as shown in Figure 1-4. The discretely sampled intensity pattern at points P and Q, located at center of subsets (X,Y) and $(X+dX,Y+dY)$, respectively, can be expressed as:

$$I(P) = I(X,Y), \qquad I(Q) = I(X+dX,Y+dY) \tag{8}$$

where (dX,dY) represents small distances in the (X, Y) coordinate system. In the image before deformation, dX and dY are integer pixel values, at this time, no interpolation is required.

After deformation of an object, points P and Q are deformed into positions p and q, respectively (Figure 1-4). It is very important to note that p and q may locate between integral pixel locations. To accurately locate the position of p and q, interpolation technique is required. Assuming that the intensity of a pattern recorded after deformation is related to the un-deformed pattern by the object deformations, the coordinates of the center point of subset after deformation can be described in terms of the un-deformed coordinates, X,Y, and the displacement vector field, $\{u(X,Y),v(X,Y)\}$ as $x = X + u(X,Y)$, $y = Y + v(X,Y)$.

Therefore, the intensity of p and q can be expressed as [19]:

$$I'(p) = I'(x, y) = I'[X + u(X,Y), Y + v(X,Y)]$$

$$I'(q) = I'(x+dx, y+dy) = I'[X + dX + u(X + dX, Y + dY),$$
$$Y + dY + v(X + dX, Y + dY)]$$
$$= I[X + u(X,Y) + (1 + \frac{\partial u}{\partial X})dX + \frac{\partial u}{\partial Y}dY, \tag{9}$$
$$Y + v(X,Y) + (1 + \frac{\partial v}{\partial X})dX + \frac{\partial v}{\partial Y}dY]$$

Assuming that the subset is sufficiently small so that the displacement gradients are nearly constant throughout the region of interest, each subset undergoes uniform strain resulting in the parallelogram shape for the deformed subset as illustrated in Figure 1-4. The matching subset can be found using the following correlation function that contains the six unknown parameters: $u, v, \frac{\partial u}{\partial X}, \frac{\partial u}{\partial Y}, \frac{\partial v}{\partial X}, \frac{\partial v}{\partial Y}$.

$$C = 1.0 - \frac{\sum\limits_{i=1}^{N}\sum\limits_{j=1}^{M} I(X_i, Y_j) I'[X_i + u(X_i, Y_j), Y_j + v(X_i, Y_j)]}{\sum\limits_{i=1}^{N}\sum\limits_{j=1}^{M} \{I^2(X_i, Y_j) I'^2[X_i + u(X_i, Y_j), Y_j + v(X_i, Y_j)]\}^{1/2}} \tag{10}$$

A set of values of $u, v, \frac{\partial u}{\partial X}, \frac{\partial u}{\partial Y}, \frac{\partial v}{\partial X}, \frac{\partial v}{\partial Y}$ which minimizes the magnitude of C is assumed to represent the best estimates of the subset's displacement and strain components. It is to be noted that the magnitude of C is zero for a perfect match and one for a complete mismatch, providing a quantitative measurement of the accuracy of the match between un-deformed and deformed subsets.

Currently a wide range of optimization methods has been used to obtain the optimal value for C; they include Newton-raphson, coarse-fine, and Levenburg – marquardt [19] methods. The iteration process [19] to obtain the six parameters that produces a minimum value of C is:

1. Obtain an initial estimate of center point translation for the subset of interest from visual inspection of the images.

2.   Allow the gradients to be non-zero and perform a full, six-parameter search process to minimize the value expressed in equation (10).   The values of u, v and the displacement gradients which minimize *C* are the optimal estimates for the displacements and displacement gradient.

3.   Using the results from the previous subset as the initial guess, repeat step 2 for the next subset.

4.   Repeat step 2 and 3 until data is obtained throughout the region of interest.

DIC technique assumed a first-order, linear approximation of the deformation mapping.   This approximation holds reasonably well when the size of the subset is small (on the order of a few pixels at each side of a square); however, a distinct gray-scale pattern might not exist in this small region, and thus it is difficult to perform image correlation to find the deformations.   A subset region of a relatively large size, on the order of tens of pixels at each side of a square, could possess a distinct gray-scale pattern necessary for image correlation; however, linear deformation mapping in the relatively large subset region might not be appropriate, and instead one must use higher order deformation mapping.   Undesirably, however, this will involve more gradient datum to be determined by iterative convergence methods that can also lead to loss of accuracy [18-20].   It should be noted that with the existence of large distortions, the specified area is liable to lose its perceptiveness in recognizing the target area.   In such case, the detection of displacements may wander off and hence the accuracy of this method would be reduced significantly.

1.2.2.2 Extension of DIC in AFM/STM/SEM Domain

Theoretically, there is no limitation in spatial resolution for digital image correlation. In addition, the displacement sensitivity is directly related to the pixel in the digital images, and thus the displacement resolution can be increased continuously by using imaging system with higher magnifications such as Atomic Force Microscope (AFM) [21,22], Scanning Tunnel Microscope (STM) [23,24], and Scanning Electron Microscope (SEM) [25,26].

In the AFM DIC [27,28], the displacement field was obtained by comparing surface topologies of un-deformed and deformed image of specimens, acquired by an AFM. Surface roughness produced by gold sputtering served as random patterns for correlation. Similar to the AFM DIC, STM images produced by a specially designed STM were utilized to document the deformation fields [29-31].

During imaging, the AFM/STM tip is only about 10 Å away from the specimen surface so the contact between tip and surface can occur. This produces random noises in the images before and after loading. Drifting associated with the piezoelectric material used in the AFM/STM also contributes to the random noise. In addition, the scanning time of AFM/STM is usually long and it is difficult to obtain AFM/STM images repeatedly. This noise and lack of repeatability limits the AFM/STM digital image correlation to only simple mechanical loading condition.

As the Scanning Electron Microscope (SEM) has become readily available, researchers have attempted to use the SEM images for DIC to record the nano-scale deformation [32-40]. The sputtered gold on the specimen surface is used as random patterns required for DIC. The SEM has a high speed scanning rate, which makes it

attractive for applications with DIC.   However, high amplitude and high frequency random noise usually appears in the SEM images.   The noise is unavoidable due to the inherent instability of the E-Beam column during scanning and the relative low signal-to-noise ratio of the detector.   In general, it is not possible to separate the noise from the patterns that DIC uses for correlation because both signals are random in nature and the frequency of noise and useful signal are similar.   In Chapter 2, the effect of SEM noise on DIC will be discussed in detail.

1.2.3 Speckle Interferometry with Electron Microscope

Similar to digital image correlation technique, Speckle Interferometry with Electron Microscope (SIEM) [41-42] also uses the random pattern as the media to realize the displacement measurement.   SIEM is also an amplitude-based measurement technique.   Two images of random patterns of a specimen, before and after deformation/loading, are captured by Scanning Electron Microscope (SEM). Two series of small subset or sub-image are obtained by evenly segmenting the two images taken before and after deformation.   The displacement between the corresponding pair of sub-images is assumed to be uniform.

Figure 1-5 shows the data processing procedure of SIEM to obtain the displacement from the corresponding sub-image pair.   This procedure includes two steps of Fast-Fourier Transform (FFT).   The first-step Fast-Fourier Transform achieves the complex spectra of the sub-images in the images before and after deformation, respectively.   The resultant spectrum is then constructed; the phase of the resultant spectrum is the phase difference of the two spectra and its amplitude is

the square root of the amplitude product of the two spectra. The second-step Fast-Fourier Transform process is conducted on the resultant spectrum, which generates a signal peak in the second spectral domain. The local displacement vector between the sub-images in the images taken before and after deformation/loading is determined uniquely by the crest position of the signal peak [41-42]. The displacement fields are then obtained by analyzing all the corresponding sub-image pairs.
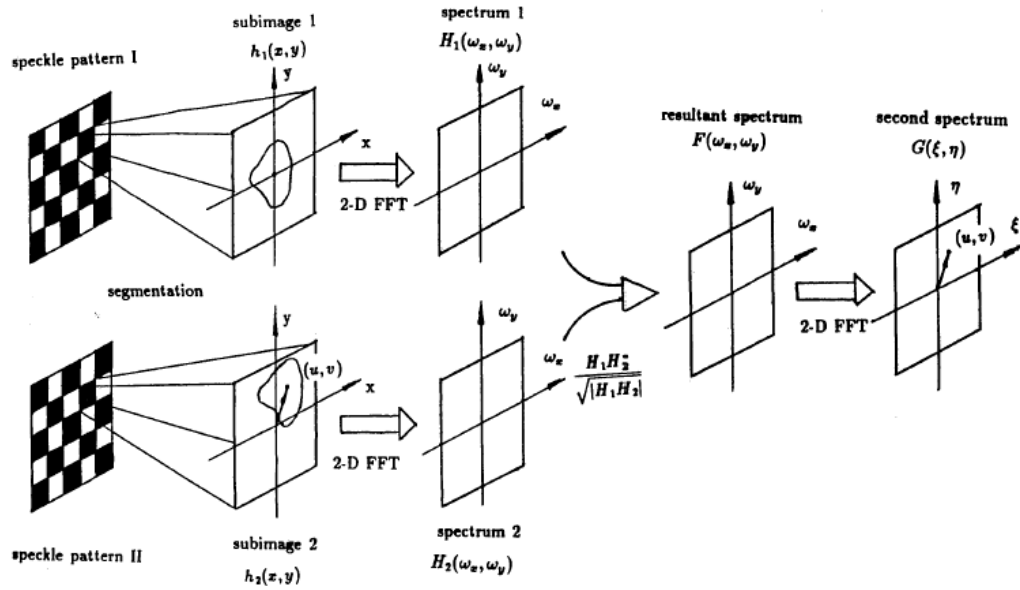
Figure 1-5 Data processing procedure of SIEM [41]

In SIEM, the uncorrelated noise can be diluted slightly during two-step FFT processing. However, SIEM is still sensitive to the noise and the effect of noise on measurement accuracy/sensitivity is obvious. Before data processing, images are needed to be segmented into the sub-images. For better correlation, an individual segment is desired to have more random patterns, which helps to insure the

16

corresponding pair of segments in the images taken before and after deformation/loading includes more common patterns [42]. This requires larger size of sub-image. Inherently, larger sub-image results in the sub-image distortion. This distortion causes the movement (error) of signal peak that will affect measurement accuracy/sensitivity dramatically.

Therefore, in nano-scale domain displacement measurement, SIEM cannot provide the required measurement accuracy/sensitivity. And SIEM is not suitable for the displacement measurement with highly localized deformation.

1.3 Objectives of the thesis

a) To study the current techniques and their limitations, which were proposed to document the nano-scale deformations in small regions of interest and understand. This will offer a better understanding of requirements for nano-scale deformation measurement. The required deformation measurement technique should be able to provide the displacement measurement accuracy/sensitivity of fraction of nanometer on a few microns length scale.

b) To develop a procedure to characterize the high frequency random noise during scanning electron microscope (SEM) imaging and quantitatively evaluate the effect of SEM noise on digital image correlation (DIC). This will offer a better understanding of the limitations of the SEM based DIC. Results will help understand the requirements for a proposed measurement technique using SEM.

c) To develop a new full-field in-plane displacement measurement technique to cope with the limitations of currently available techniques. The proposed technique should be insensitive to the high frequency SEM random noise inherently involved during SEM imaging. Therefore low frequency signal (pattern) in the digital image has to be used as the media to realize the displacement measurement. Regularly oriental structures can satisfy this requirement. The proposed technique should also provide sufficient displacement measurement accuracy/sensitivity and spatial resolution required for the nano-scale deformation measurement.

d) To develop a method to fabricate the regularly oriented nano-scale structures on the specimen surface; the structures or patterns are utilized as the media to realize displacement measurement for the proposed displacement measurement technique. The proposed pattern fabrication method should be capable of producing the patterns with different size ranging from sub-100 nm to micron scale in diameter. This will make the application of proposed displacement measurement technique possible on the region of interest from a few microns to tens of microns scale.

e) To study the nano-scale deformations of microelectronic package using the proposed displacement measurement technique.

A brief overview of dissertation organization is discussed in the next section.

1.4 Dissertation Organization

In this dissertation, Chapter 1 introduces the motivation through reviewing the currently available techniques, which were proposed to document the nano-scale deformations.

Chapter 2 discusses the characterization of SEM noise and its effect on the digital image correlation technique. A complete procedure to characterize the high frequency random noise during SEM imaging is developed. The SEM noise level is proved to be related to the imaging parameters (electron accelerated energy, spot size etc.). SEM noise for mid-range magnification (a few hundred microns scale) imaging setup (30 keV, spot size 3) and for high-range magnification (a few microns scale) imaging setup (30 keV, spot size 1) are characterized. Applicability of the conventional random noise reduction schemes is also discussed. Using the computer simulated ideal random pattern, the effect of SEM noise on the accuracy of digital image correlation technique is quantified in terms of displacement field and strain field. This chapter has been submitted as a research paper to Experimental Mechanics.

Chapter 3 focuses on the development of full-field in-plane displacement measurement technique: *Nano-Pattern Recognition and Correlation Technique* (N-PRCT). Each step of image processing procedure in N-PRCT is explicated. The displacement measurement accuracy/ sensitivity of N-PRCT is also discussed in this chapter. A preliminary experimental result is shown in this chapter and verifies the feasibility of N-PRCT.

Chapter 4 discusses the nano-scale thermal deformation measurements of microelectronics circuits by N-PRCT. The E-beam sensitized materials selection and specimen preparation procedure are discussed. A novel practice of E-bema lithography is proposed to fabricate regularly oriented structures on the object surface. The proposed method utilizes the standard SEM to fabricate the pattern without the need of specially designed E-Beam lithography system, which makes the implementation of N-PRCT practical. Yet, the proposed procedure can produce gauge lengths (approximately 150 nm) than those produced by a commercial E-beam lithography system Thermal loading setup for the experiment conducted in the SEM chamber is discussed in this chapter. This chapter is going to be submitted as an invited research paper to Journal of Strain Analysis for Engineering Design.

Chapter 5 contains a summary of the technical contribution and future work. It provides the directions in which the current work will be extended.

Chapter 2: On the Effect of SEM Noise at Extreme Magnifications on the Accuracy of Displacement Fields Obtained by DIC[1]

ABSTRACT

Random noise inherently present in SEM images at extreme magnifications is characterized. The noises caused by two major sources (read-out system and E-beam stability) are quantified experimentally using a defocused SEM configuration. A theoretical/experimental analysis is conducted to ascertain that the random noise cannot always be suppressed by the conventional high frequency random noise reduction schemes when it exists in an ideal pattern for the Digital Image Correlation (DIC) technique. The effect of the inherent noise on the accuracy of the SEM-based DIC is quantified for deformation fields with a uniform strain as well as a strain gradient.

2.1 Introduction

In recent years, numerous deformation measurement techniques utilizing the scanning electron microscope (SEM), most notably SEM-based digital image correlation (DIC) [32-39], have been proposed for nano-scale deformation analyses.

---

[1] This chapter has been submitted as a research paper to *Experimental Mechanics* under the title "On the Effect of SEM Noise at Extreme Magnifications on the Accuracy of Displacement Fields Obtained by DIC", by H. Bi and B. Han.

The SEM was a preferred imaging system for the high magnification required for the analyses because of its simple specimen preparation and imaging procedure compared to other non-optical high magnification techniques.

The DIC technique is an amplitude-based measurement technique, which should be distinguished from phase-based measurement techniques. The former utilizes the grey level of distinct patterns in a region and performs correlation between the images before and after loading to produce a displacement field. The latter utilizes the phase information of light (e.g., interferometric techniques) and produces an output signal as a form of harmonic functions whose arguments are linearly proportional to displacements. Consequently, amplitude-based measurement techniques are essentially more sensitive to intensity fluctuations and random noise of digital images. This is precisely the reason why an extremely stable imaging system and light source are required for successful implementation of DIC [18-20].

In general, phase-based measurement techniques offer a much higher signal-to-noise ratio in the output displacement fields, but they are not difficult or often impractical for light sources with wavelengths below the visible spectrum. The advantages and disadvantages of displacement measurement techniques are summarized in Table 2-1.

Although the SEM offers the required magnification (i.e., spatial resolution) for the nano-scale deformation analyses, distortion and random noise in SEM images are unavoidable. The effect of distortions has been discussed extensively by many researchers, most notably by Sutton et al. [34-37], and numerous calibration

algorithms to compensate the distortion have been proposed [34, 40]. Yet the effect of the random noise has not been addressed and this is the motivation of the present study.

The frequency of the random noise is typically on the same order of the random patterns used in DIC. If the random noise cannot be removed effectively, the displacement uncertainties can make the SEM-based DIC unsuitable for measurements of deformations with local displacement gradients. The objective of this paper is to characterize the random noise present in SEM images and to quantify the effect of the noise on the accuracy of SEM-based DIC.

Table 2-1 Advantages and disadvantages of displacement measurement techniques

	Phase-based technique	**Amplitude-based technique**
Displacement	The phase information produces an output signal whose arguments are linearly proportional to displacements.	The grey scales are used to perform correlation between the images before and after loading, which produces a displacement field.
Intensity	Phase is not affected directly by the background intensity.	Intensity fluctuation directly affects displacement fields; light source has to be extremely stable.
Random noise	High frequency random noise (e.g., electronic noise of CCD) can be readily separated from relatively low frequency phase signal.	Difficult to remove random noise; a camera with extremely high S/N ratio has to be used to cope with the problem.
Imaging device	Difficult or even impractical to implement with short wavelength below the visible spectrum.	No theoretical limitations with imaging devices.

2.2 Characterization of Random Noise

The random noise in SEM images is caused by inherent instability of E-Beam during scanning as well as the signal-to-noise ratio of the detector. The possible causes of the noise during SEM imaging are summarized in Table 2-2 [26]. A set of controlled experiments were performed to characterize the noise quantitatively using a commercial E-SEM (FEI; Quanta 200).

Table 2-2 Sources of noise during SEM imaging [26]

Noise source	Description	Related setup parameters
Primary electron beam noise	The number of primary electrons hitting the specimen during a given pixel time (dwelling time) is statistically distributed.	Voltage, spot size, dwelling time
Secondary electron beam noise	The number of secondary electron produced by primary electrons during a given pixel time (dwelling time) is statistically distributed.	Primary electron noise, dwelling time
Detector and readout noise	Noise introduced by detector and readout system.	Detector, readout system

2.2.1 Detector and Readout Noise

With a typical SEM configuration, the electron signal is captured by a detector. The photomultiplier voltage is automatically adjusted to produce a measurable electrical signal. This can be regarded as a variable gain since it changes with the strength of the initial electron signal. If a spot size is increased at this point, the photomultiplier voltage will be decreased automatically in proportion to the ratio

between two spot sizes. The analog-digital converter (ADC) samples the electric signal at a constant sampling rate over the dwell time after the signal is amplified by the preamplifier. The value calculated for pixel integration is stored for the corresponding pixel on the image. The attractive voltage (or contrast option) can be adjusted to produce an image with desired contrast. The contrast is also a variable gain, which amplifies the signal and noise by a constant.

The detector and readout noise was characterized first. The SEM images were taken before the E-beam was turned on. Two spot sizes were used, and the SEM preset a gain for each spot size; Spot size 1 (0.4 nm) and Spot size 3 (1 nm).

The results from the SEM read-out are shown in Figure 2-1 and 2-2 for Spot size 1 and 3, respectively. It should be noted that the bias control (intensity) was adjusted until the mean intensity became approximately the middle value of the 8 bit grey level. The output image and the output signal distribution along the centerline are shown in (a) and (b). The output signal averaged over the vertical direction is shown in (c), which is a clear indication of the random nature of the noise signal.

Table 2-3 Statistical results of detector and readout system noise

Voltage, spot size	Mean (bias)	Standard deviation
30 kV, Spot size 1	128.2	14.4 ± 0.8
30 kV, Spot size 3	129.4	3.7 ± 0.3

The noise amplitude can be defined as the deviation from the average background intensity (mean or bias). The noise amplitude and the corresponding standard deviations were calculated using the average value determined from (c).

The noise distributions are shown in (d), which shows a normal distribution. The mean values and the averaged standard deviations are summarized in Table 2-3, where the variations in the standard deviation were obtained from 20 independent measurements. The average standard deviations of Spot size 1 and 3 are 14.4 and 3.7, respectively.

(a)

(b)

(c)

(d)
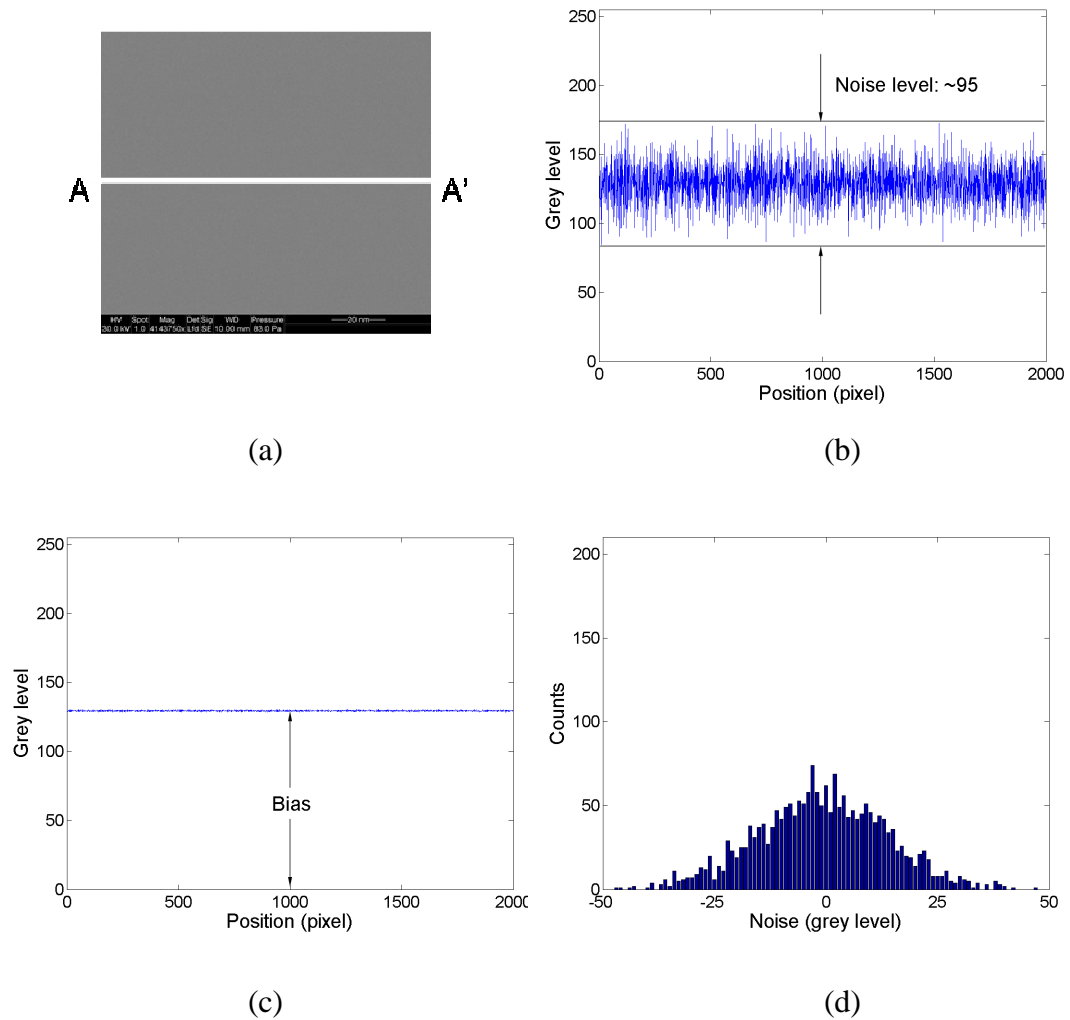
Figure 2-1 SEM noise produced by the detector and readout system at high magnification; 30 kV, spot size 1 (0.4 nm). (a) SEM image when E-beam is

turned off, **(b) intensity plot along AA', (c) averaged signal over horizontal lines,**

and (d) histogram plot of noise.

(a)   (b)

(c)   (d)
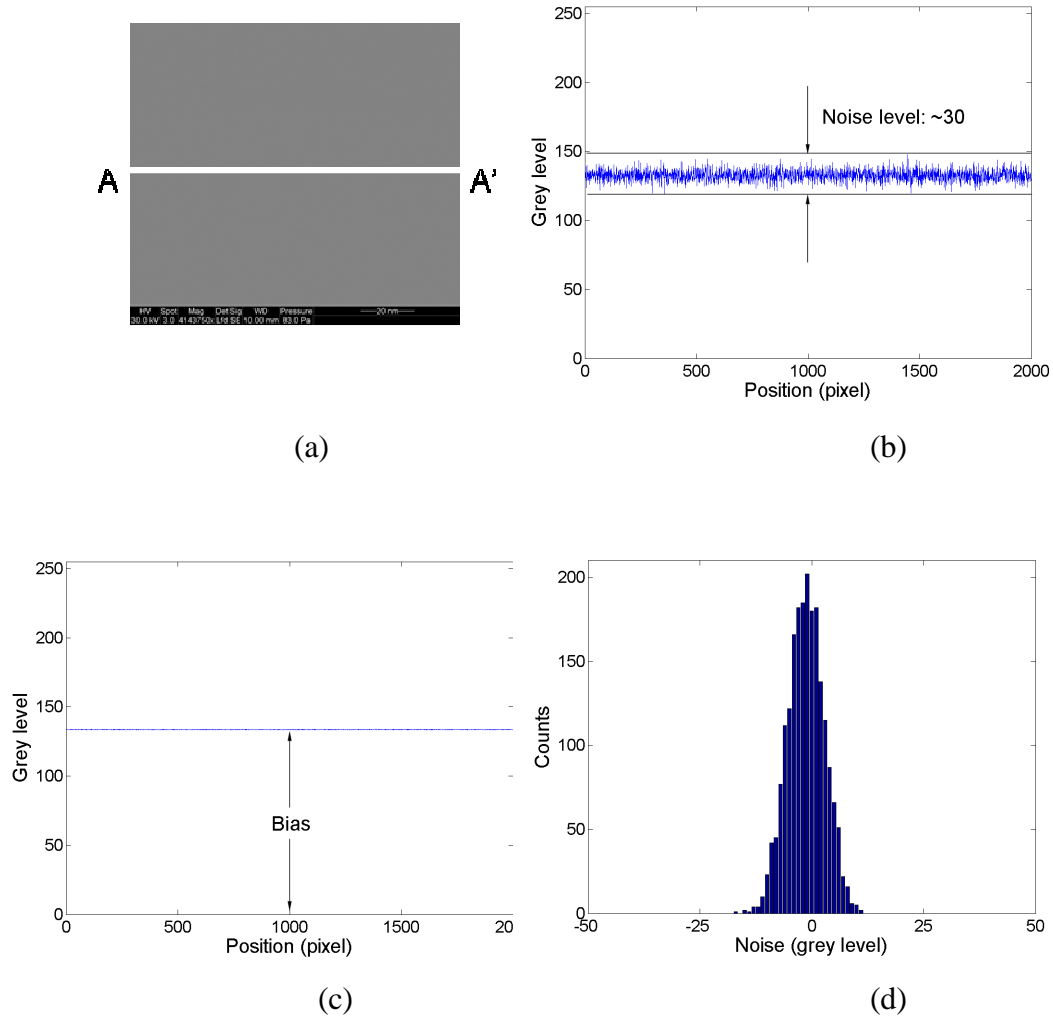
Figure 2-2 SEM noise produced by the detector and readout system at high magnification; 30 kV, spot size 3 (1 nm). (a) SEM image when E-beam is turned off, (b) intensity plot along AA', (c) averaged signal over horizontal lines, and (d) histogram plot of noise.

2.2.2 Contribution of Electron Beam to Noise

An optical flat coated with a vacuum-deposited gold layer ($\approx$ 2 nm) was used to investigate the effect of E-beam instability on the noise. The optical flat had flatness less than $\lambda/20$ over an area of 10 mm by 10 mm and should produce a constant SEM signal within the area.
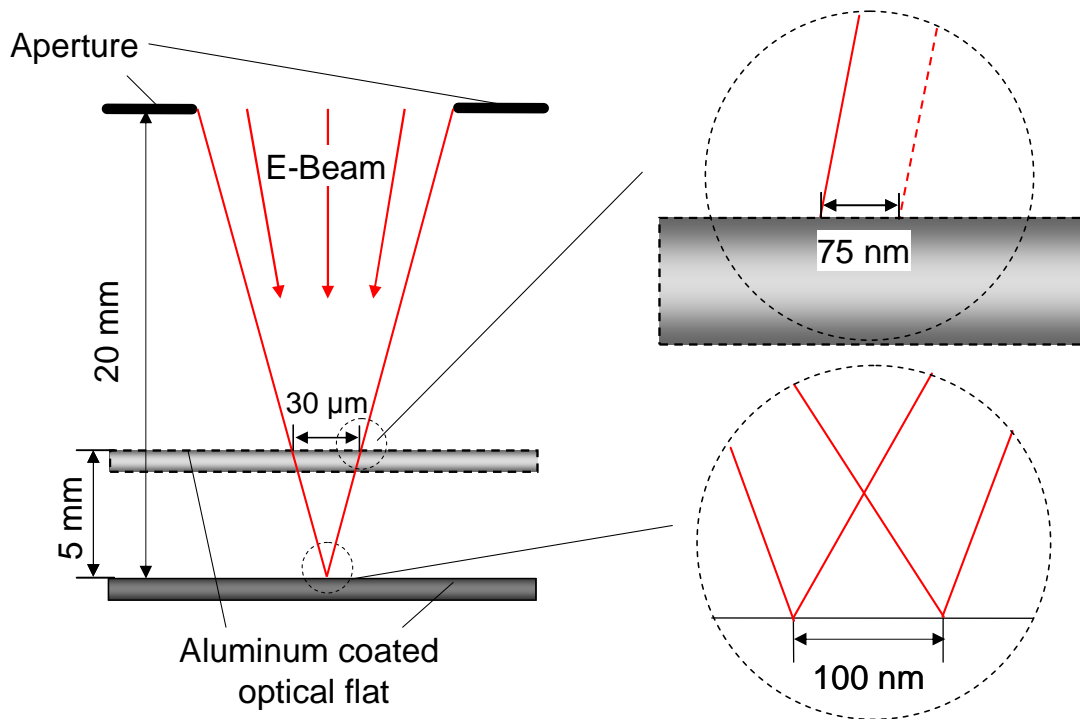
Figure 2-3 Schematic illustration of an experimental set up using the defocused E-beam.

In order to include the noise caused only by instability of the E-beam (no effect from drifting), the signal was recorded by a setup illustrated in Figure 2-3. In the setup, the E-beam was focused first on the specimen surface. The specimen was

then translated in the vertical direction by approximately 5 mm. The translation defocused the E-beam and the beam illuminated a region of around 30 μm. Then the SEM image was taken at the very high magnification (a field of view 100 nm) using the two different spot sizes. As illustrated in the insert of Figure 2-3, the amount of the beam movement during rastering is 75 nm, which is only a small fraction of the illuminated area (30 μm). Consequently, the number of electrons collected by the detector is affected only by the instability of the E-beam, regardless of the nano-scale surface anomalies and the amount of drifting.

The intensity distribution along the centerline and the noise distribution are shown in Figure 2-4a and b for Spot size 1 (0.4 nm) and 3 (1 nm), respectively, which represents the total exhibition noise (noise exhibited as grey level in an SEM image). The mean values and the averaged standard deviations obtained from 20 independent measurements are summarized in Table 2-4. The average standard deviations of Spot size 1 and 3 are 17.2 and 4.7, respectively. The noise level is only slightly higher compared with the detector and readout noise, indicating that the random noise produced by the detector and readout system is dominant.

Table 2-4 Statistical result of combined noise during SEM imaging

Voltage, spot size	Mean (bias)	Standard deviation
30 kV, Spot size 1	128.9	17.2 ± 1.1
30 kV, Spot size 3	129.0	4.7 ± 0.4
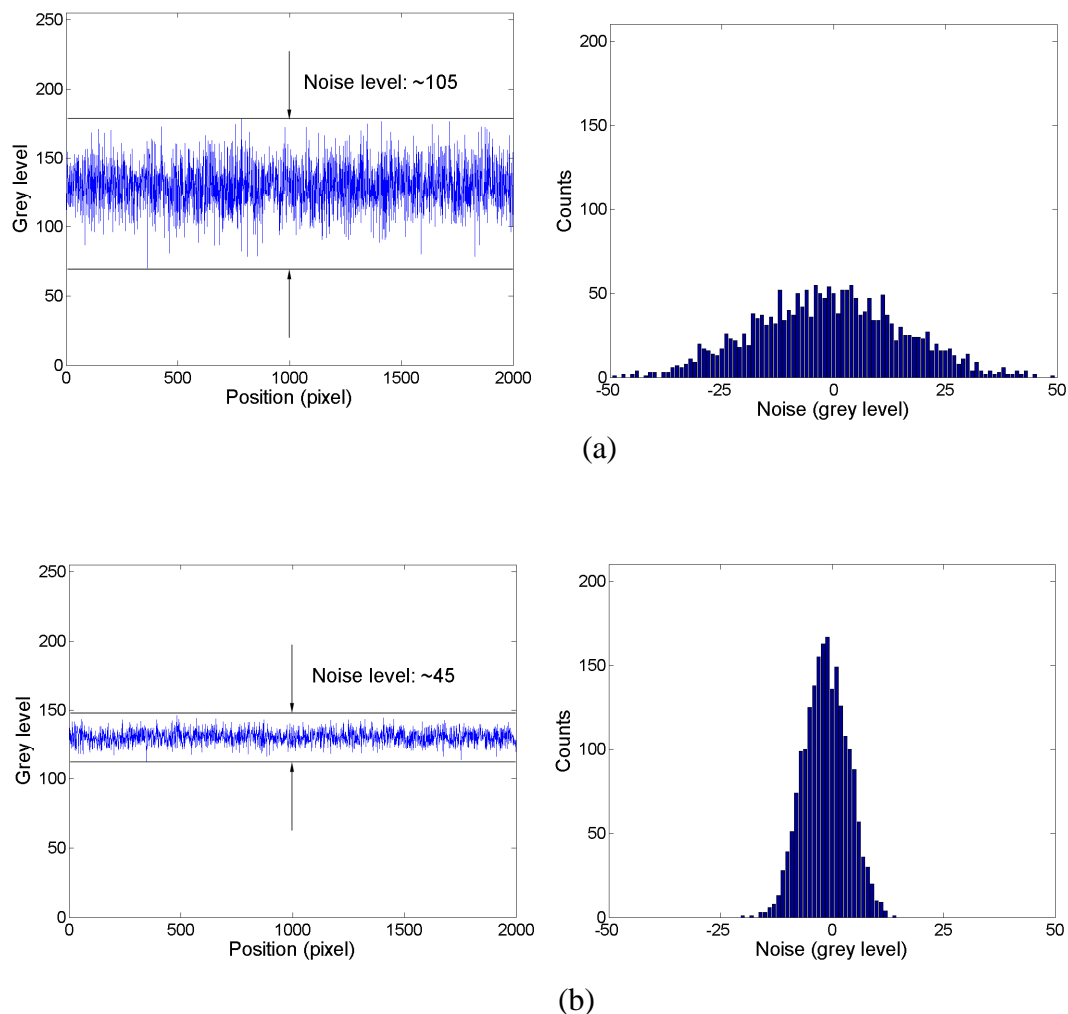
Figure 2-4 SEM noise obtained by the setup shown in Figure 2-3. (a) Intensity plot of SEM image at high magnification (30 kV and spot size 1), (b) histogram plot of the noise of (a), (c) intensity plot of SEM image at low magnification (30 kV and spot size 3), and (d) histogram plot of the noise of (c).

2.3 Applicability of Conventional Random Noise Reduction Schemes

Two conventional high frequency random noise reduction schemes are implemented to investigate how effectively the random noise can be suppressed when it exists in an ideal pattern for the Digital Image Correlation (DIC) technique.

2.3.1 Low Pass Filter (Spatial Averaging)

The most popular scheme to reduce the random noise is spatial averaging (low pass filter). The low pass filter can be described in the frequency domain using the two-dimensional fast Fourier transform (FFT). The two-dimensional FFT is defined as [43]

$$F(u,v) = \frac{1}{MN} \sum_{i=0}^{M-1} \sum_{j=0}^{N-1} G(i,j) e^{-i2\pi(\frac{ui}{M}+\frac{vj}{N})} \tag{11}$$

where (i, j) is the pixel coordinate in the spatial domain, $G(i, j)$ is the grey level of the pixel at position (i, j) in the spatial domain, and the exponential term $e^{-i2\pi(\frac{ui}{M}+\frac{vj}{N})}$ is the base function corresponding to each point $F(u,v)$ in the frequency domain; (u,v) is the coordinate in the frequency domain. Equation (11) can be interpreted as "the amplitude and phase of each point $F(u,v)$ is obtained by multiplying the spatial image with the corresponding base function and summing the results." The equation clearly indicates that the spatial averaging can only be used when the frequency of the signal is much lower than that of the noise; otherwise the original signal can be distorted significantly.

A computer-generated digital image is utilized to investigate the applicability of the low pass filter. The random noise simulating the SEM noise with only Spot

size 1 is considered.   A detailed procedure to produce an ideal DIC pattern can be found in Appendix.

(a)

(b)

(c)

(d)
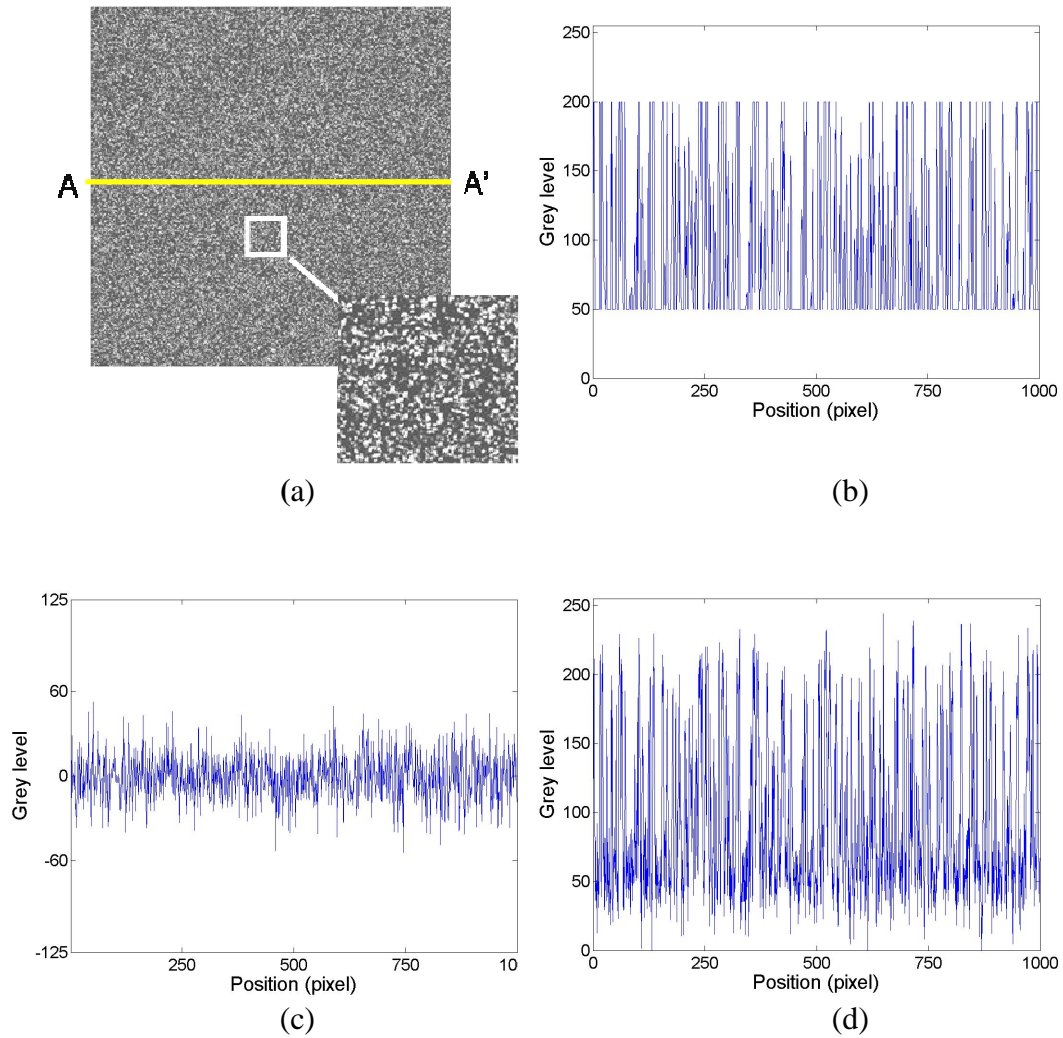
Figure 2-5 (a) Ideal random pattern, (b) intensity plot along AA' in (a), (c) random noise simulating the high magnification case (30 kV and spot size 1), and (d) intensity plot along AA' after the random noise (c) is added to the ideal pattern (a).

Figure 2-5(a) shows a 1000×1000 pixel digital image containing computer-generated ideal 3×3 random patterns. The intensity distributions along the centerline is shown in Figure 2-5(b). The random noise simulating the real SEM noise of Spot size 1 is shown in (c) and the intensity distributions along the centerline after adding the noise is shown in (d).

The results of spatial averaging using a 3×3 low pass filter are explained in the frequency spectrum. The frequency spectra of the ideal pattern and the ideal pattern with the noise are shown in Figure 2-6(a) and (b), respectively. The ideal pattern with the random noise processed by the low pass filter is shown in (c).

In order to investigate the effect of the low pass filter, the original intensity was subtracted from the processed image, and the result is plotted in (d). Although the high frequency noise was reduced substantially, the high frequency of the original image was also affected significantly. The net result is virtually the same level of random noise after the low pass filter. Consequently the DIC will suffer from this noise.

(a)   (b)

33

(c)   (d)
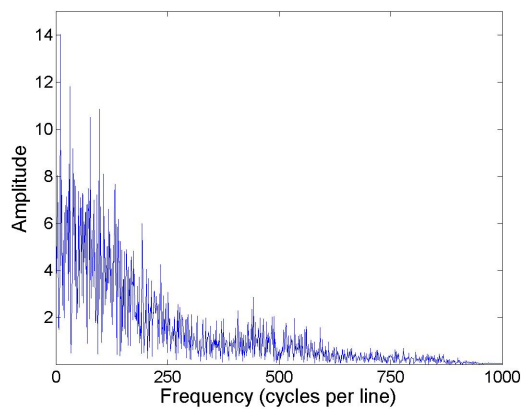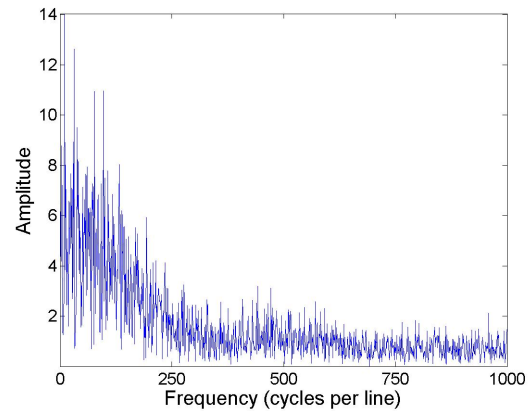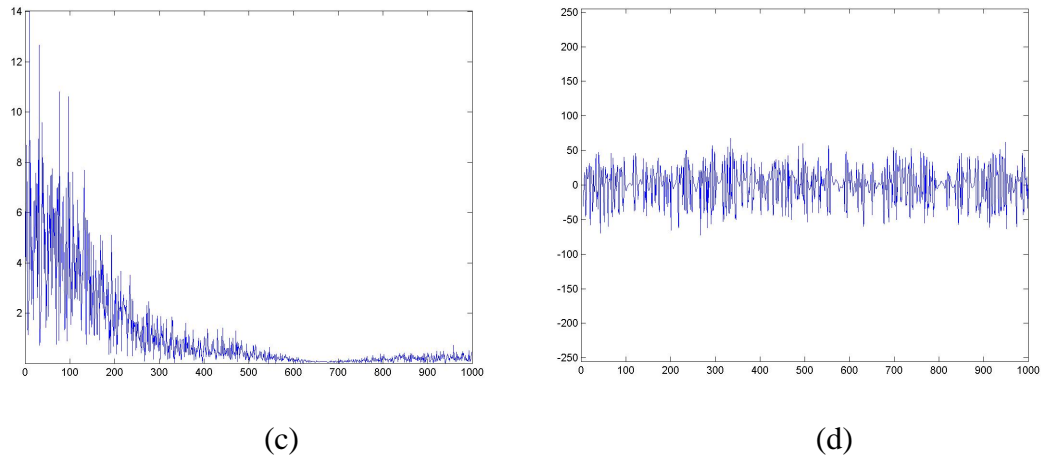
Figure 2-6 (a) FFT plot of the ideal random pattern (Figure 2-5b), (b) FFT plot of random pattern with the noise (Figure 2-5d), (c) FFT plot of the random pattern with noise after processed by the low pass filter, and (d) error in grey level obtained by subtracting the original ideal random pattern from the pattern after the low pass filter.

2.3.2 Time Averaging

Time averaging is an effective scheme to suppress random noise. The procedure includes recording the same image multiple times and averaging them to remove the random noise. The scheme is very effective for an ideal condition where the imaging system is stable during the entire period of recording multiple images.

During SEM imaging, however, the identical images of the same area are difficult to obtain due to the inherent instability of scanning process (unrepeatable raster). The SEM has significant drifting during scanning in the direction perpendicular to the scanning direction. The amount of drifting is random and the

34

relative magnitude is inversely proportional to the field of view; i.e., the effect of drifting on image distortion increases as the field of view decreases (or the magnification increases).

(a)

(b)

(c)

(d)
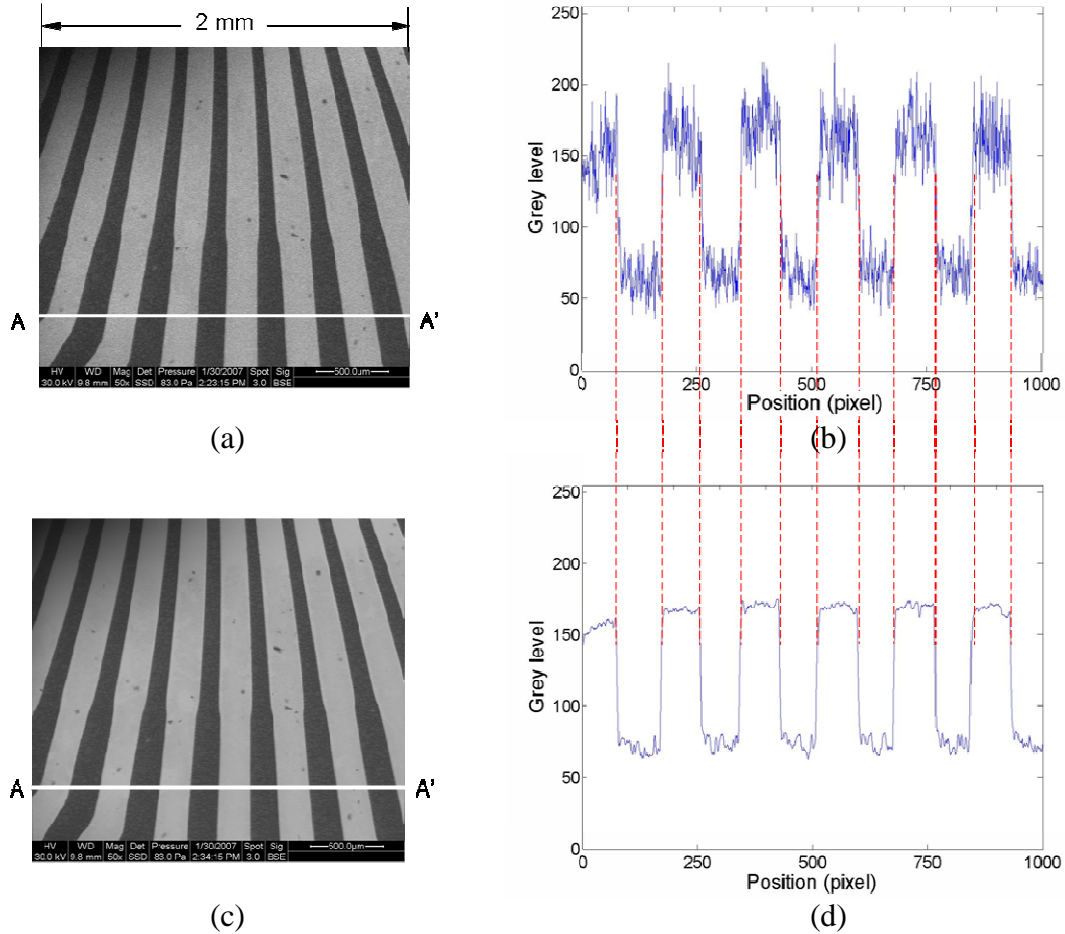
Figure 2-7 Illustration of time-averaging at a large field of view. (a) SEM image, (b) intensity plot along AA' in (a), (c) SEM image after time-averaging, and (d) intensity plot along AA' in (c).

Two examples are shown to illustrate this effect. The first example contains vertically oriented metallic structures embedded in a polymeric material in a

relatively large field of view (approximately 2 mm).   The setup parameters include Spot size of 3 and voltage of 30 kV.   The original image and the intensity distribution along line AA' are shown in Figure 2-7(a) and (b).   The same image was captured 10 times and then the images were averaged.   The resultant pattern and the intensity distribution along the same line are shown in Figure 2-7(c) and (d).   The boundaries of the metal structures are not the affected by the time averaging process, yet the reduction of noise is evident.

The second example uses the nano-template patterns.   They are nano-scale pores of Alumina grown on a single-crystal Al substrate [44].   Images at a high magnification (a small field of view, approximately 5 μm) were taken 10 times and then were averaged.   The setup parameters include Spot size of 1 and voltage of 30 kV.   The representative image and the averaged image are shown in Figure 2-8(a) and (b), respectively.   The intensity distributions along a small portion of center line (line AA') before and after time averaging are plotted in Figure 2-8(c).

The level of distortion of the original signal is substantial despite the reduction of the random noise.   The results clearly show that time-averaging should not be used for the patterns when the magnification is high.   The drifting can distort the random patterns for DIC significantly during time averaging.   This is a problem existing *uniquely* with the SEM operated at high magnifications.

(a)   (b)

(c)
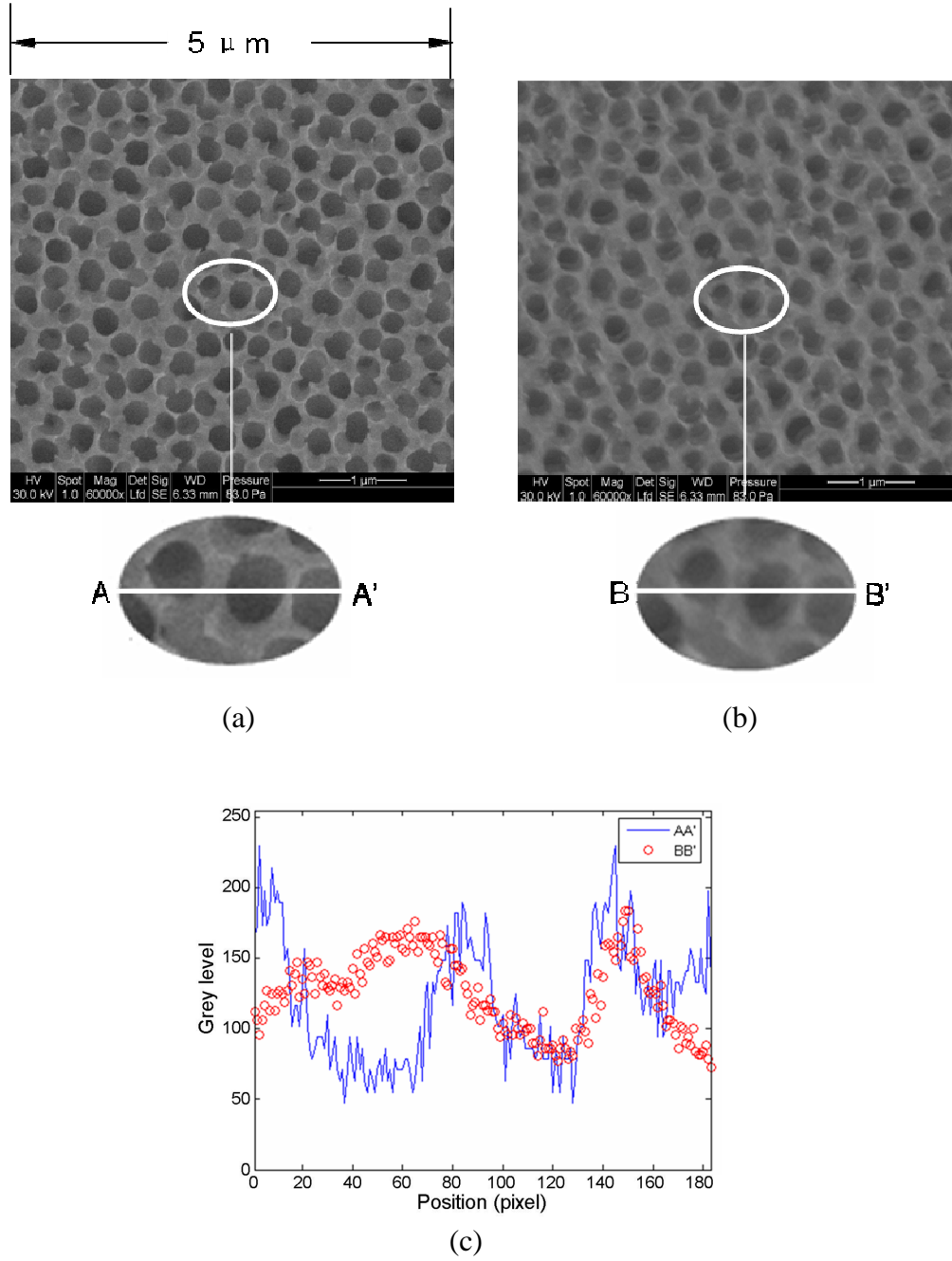
**Figure 2-8 Illustration of time-averaging at a small field of view.   (a) SEM
image, (b) SEM image after time-averaging, and (c) intensity plots along AA.**

2.4 Effect of Random Noise on Accuracy of DIC

None of the existing schemes can effectively separate the random pattern from the random noise. Numerical simulations are conducted to investigate the effect of random noise in the SEM images on the accuracy of displacement fields produced by DIC and strain fields by a post-processing.

An infinite plate with a hole subjected to uniaxial tension is selected for the simulation. The problem and the ideal random pattern applied to the region of interest (1000×1000 pixel) are shown schematically in Figure 2-9(a). In the simulation, a uniaxial tension loading, p, of $100 MPa$ is applied to an aluminum plate with a hole ($E = 70 GPa$ and $\upsilon = 0.33$). The displacement fields can be expressed as [45]:

$$u_r = \frac{pr}{2E}\left\{(1-\upsilon)+(1+\upsilon)\left(\frac{R}{r}\right)^2 + \left[4\left(\frac{R}{r}\right)^2+(1+\upsilon)-(1+\upsilon)\left(\frac{R}{r}\right)^4\right]\cos(2\theta)\right\} \quad (12)$$

$$u_\theta = -\frac{pr}{2E}\left[2(1-\upsilon)\left(\frac{R}{r}\right)^2+(1+\upsilon)+(1+\upsilon)\left(\frac{R}{r}\right)^4\right]\sin(2\theta) \quad (13)$$

$$u_x = u_r \cos\theta - u_\theta \sin\theta \quad (14)$$

$$u_y = u_r \sin\theta + u_\theta \cos\theta \quad (15)$$
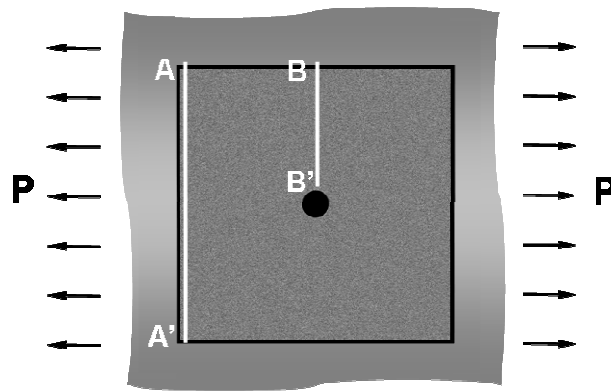
(a)
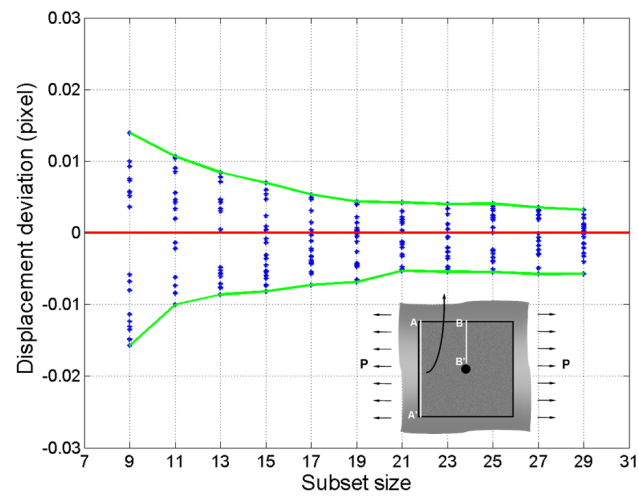
(b)
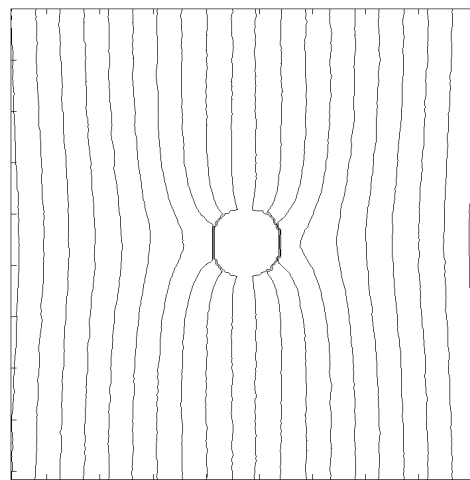
(c)
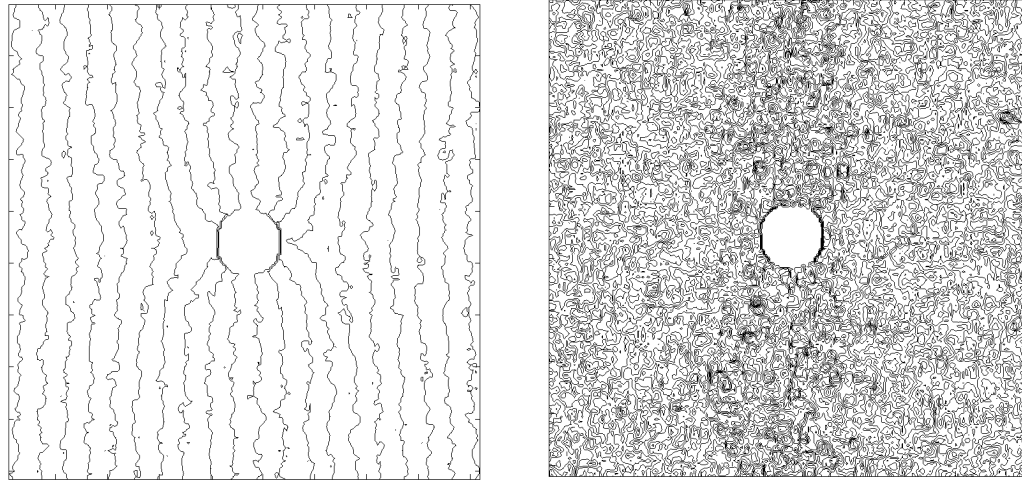
(d)

(e)
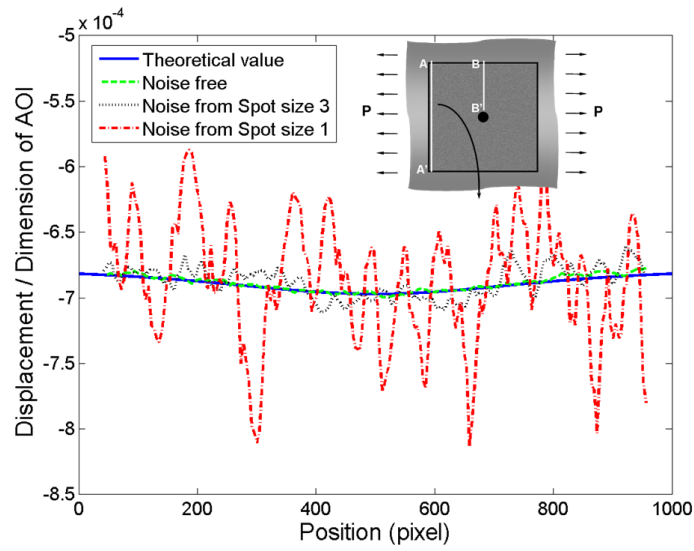
(f)

Figure 2-9 (a) Infinite plate subjected to a uni-axial tension and (b) deviations from the theoretical displacements along AA' as a function of the subset size. The x-direction displacement contour plots obtained from (c) the noise-free image, (d) the SEM noise simulating the low magnification (spot size 3), and (e)

the SEM noise simulating the high magnification (spot size 1) where a contour interval is 0.05 pixel.   (f) Displacement distributions along line AA' in (a).

2.4.1 Displacement Field

In the DIC technique, the displacement accuracy is directly related to a subset size.   A larger subset is capable of providing more varying intensities, which is desirable for image correlation.   However, the subset should be sufficiently small so that the displacement gradients within it should satisfy the correlation assumption.

In order to determine the proper subset size, displacement fields were obtained using various subset sizes (9 to 29).   In the simulations, a step size of 10, the cubic B-spline interpolation, and the affine transformation were used.   The displacements along line AA' in Figure 2-9(a) was virtually constant and they were utilized for the selection process.   The displacements obtained from the DIC were compared with the theoretical values (Eq. 22).   The deviations from the theoretical values are plotted in Figure 2-9(b) as a function of the subset size, where the lines indicate the upper and lower bounds of deviations.   It is to be noted that for each subset, a total of 20 data points were used in the plot.   As expected, the magnitude of the displacement errors decreases as the subset size increases.   When the subset size reaches 21, the error converges to a value smaller than the theoretical limits of 0.01 pixel claimed in Ref. [19].   The subset size of 21 was used for all subsequent calculations.

The x-direction displacement contours obtained from the noise-free image is shown in Figure 2-9(c), where a contour interval is 0.05 pixel.   The random noise

equivalent to the SEM noise of Spot sizes 3 and 1 were generated and added to the noise-free image. The DIC results of Spot sizes 3 and 1 are shown in Figure 2-9(d) and (e), respectively. The noise increased substantially with the SEM random noise. The distinct contours are no longer visible in Figure 2-9(e), which indicates that the displacement error exceeds the contour interval.

Displacements along line AA' in Figure 2-9(a) are virtually uniform. They are utilized to illustrate the errors more quantitatively. Figure 2-9(f) shows the displacement plots along line AA' for all four cases. The level of displacement errors (dashed red line) caused by the noise simulating Spot size 1 is extremely large and the original trend of the displacement is no longer discernable.

2.4.2 Strain Field

Strains can be determined from the displacement gradient. Similar to the subset size, a gauge length used in determination of the displacement gradient governs the strain distribution. A larger gauge length results in a smoother strain distribution but it may reduce the magnitude of the maximum strain significantly due to the averaging effect. A smaller gauge length can potentially provide a more accurate strain distribution. However, the strains become much more susceptible to the displacement error, which may result in excessive strain errors.

A gage length of the hole radius (50 pixel) was used to illustrate the effect of the noise on the strain distribution. The strain plot obtained from the theoretical displacement field (i.e., the gage length of one pixel) is shown in Figure 2-10(a). The corresponding strain plots determined from the DIC displacement fields using the

gage length of 50 pixels are shown in (b)-(d) for the ideal patterns with no noise, the

noise of Spot size 3 and the noise of Spot size 1, respectively.   The increased errors

in the strain plots are evident.   The strain trend is barely seen in Fig, 2-10(c) but it is

not possible to discern the true strain field in Figure 2-10(d).

(a)   (b)

(c)   (d)
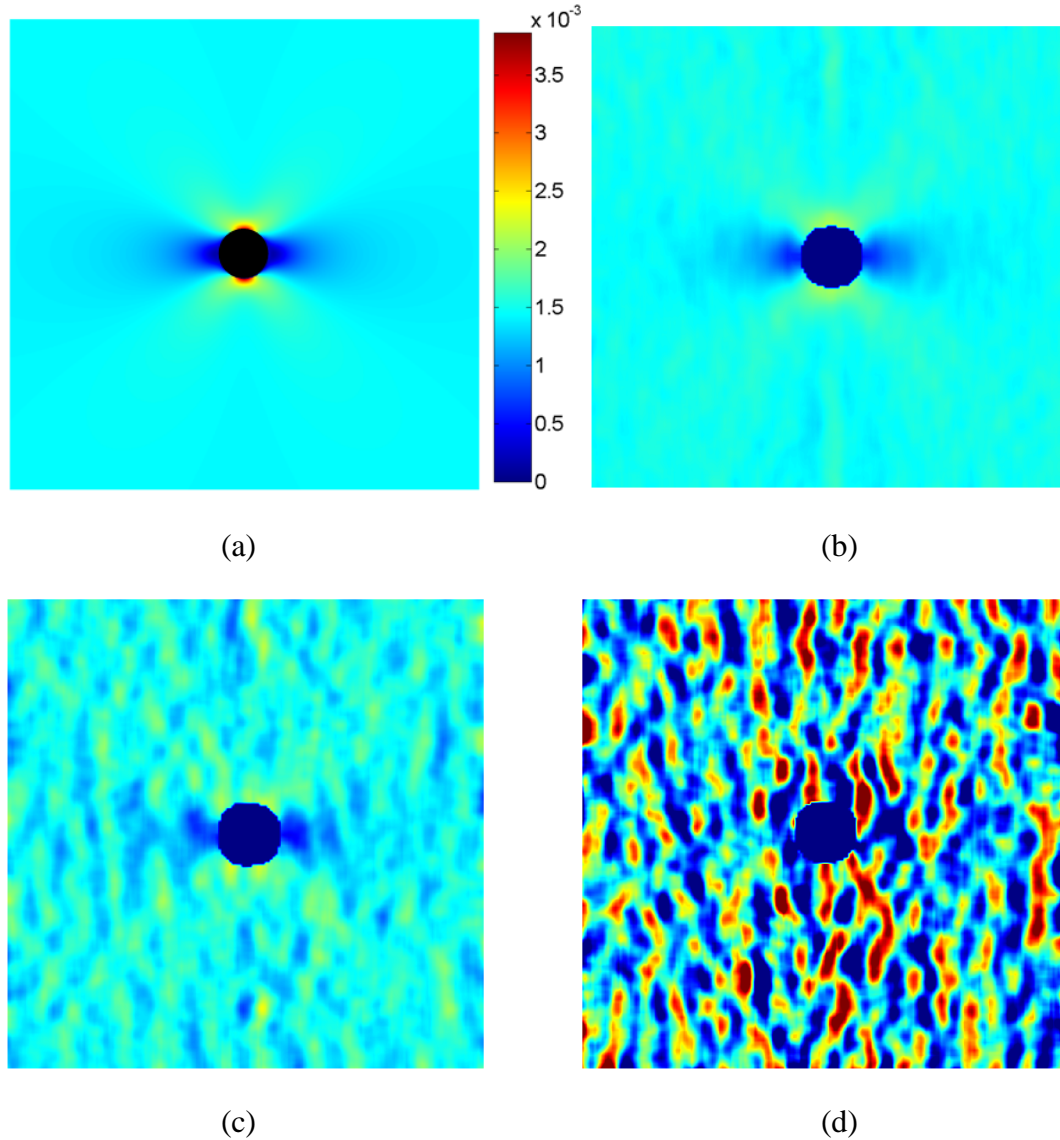
Figure 2-10 (a) Strain plot obtained from the theoretical displacement field.

The corresponding strain plots determined from the DIC displacement fields of

the ideal patterns with (b) no noise, (c) the noise of spot size 3, and (d) the noise

of spot size 1.
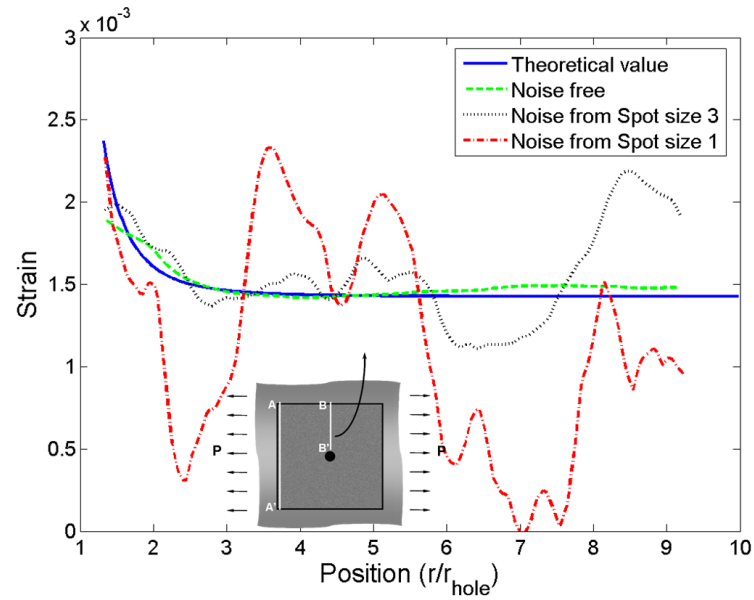
(a)
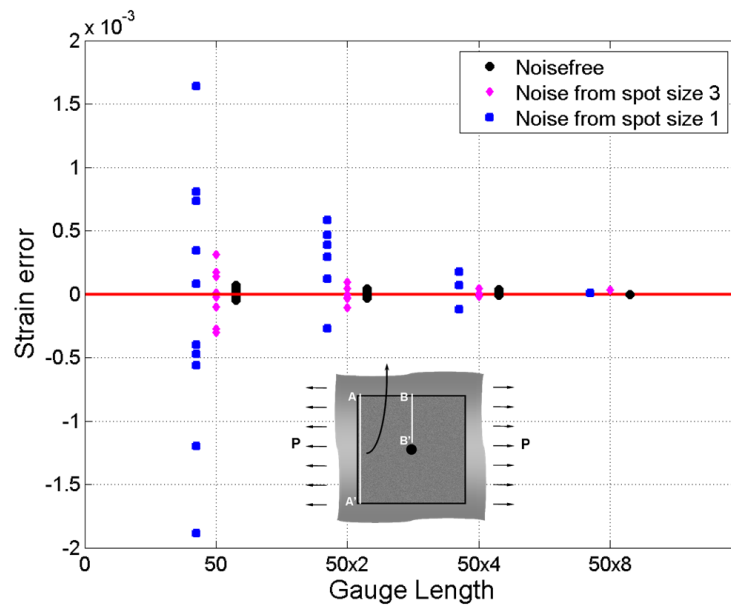
(b)

Figure 2-11 (a) Strain distribution along line BB' in Figure 2-9a, and (b) average strain calculated along line AA' in Figure 9a using different gage lengths.

Strains along line BB' in Figure 2-9(a) have the largest gradient. They were utilized to illustrate the strain errors more quantitatively. The strain distributions along line BB' are shown in Figure 2-11(a). The blue and green solid lines show the theoretical strain distribution and the strain distribution from the noise free pattern, respectively. The noise free pattern shows reasonable agreement with the theoretical strain except the reduced maximum strain which was caused by averaging over a large length. The strain obtained with the Spot size 3 noise (dashed-black line) also shows a reasonable distribution while the trend of the strain distribution was hardly discernable in the strain obtained with the Spot size 1 noise (dashed-red).

The average strain was also calculated along line AA' using different gage lengths. The strains obtained from the DIC were compared with the theoretical values, and the deviations from the theoretical values are plotted in Figure 2-11(b) as a function of the gage length. As expected, the magnitude of the strain errors decreases as the gage length increases. When the gage length is larger than 400 pixels (nearly half the region of interest), the error becomes virtually zero regardless of the random noise. The results confirm that applications that deal with uniform strains can still be handled by the SEM-based DIC regardless of the magnifications.

2.5 Conclusion

The random noise inherently present in SEM images at extreme magnifications were characterized and quantified experimentally. It was found that the noise was caused mainly by the detector and read-out system. A theoretical/experimental analysis proceeded to examine the applicability of two conventional random noise reduction

schemes (low pass filtering and time-averaging) to suppress the simulated random noise in an ideal pattern for the DIC technique. The results indicated that neither scheme could eliminate the noise effectively. The effect of this inherent noise on the accuracy of the SEM-based DIC was then quantified for deformation fields with a uniform strain as well as a strain gradient. The results clearly showed why it is difficult to implement the conventional DIC technique with the SEM with extremely high magnifications, especially when a displacement field with a non-uniform gradient is sought.

Appendix: Ideal Random Pattern for DIC

Random patterns are required for the DIC technique. A nearly ideal random pattern can be produced on the specimen surface by spaying it with white paint. An ideal random pattern should provide as many varying intensities as possible. In addition, the pattern size must be sufficiently small to ensure that the subset shape function is effective during the correlation processing [46]. The following procedure describes how to produce a 3 x 3 ideal random pattern simulating the spray paint, which is illustrated in Figure A1.

<u>Undeformed configuration</u>

Step 1: Determination of the center pixels of a 3×3 pixel pattern:

Random numbers ranging from 0 to 1 are generated and assigned to each pixel. The pixels containing the random numbers smaller than 1/9 are selected as the center pixels; i.e., for a digital image of $m \times n$ pixels, the number of the center pixels is

approximately $\dfrac{m \times n}{9}$. Adjacent pixels have random numbers smaller than 1/9 are

allowed in the simulation. This simulates two (or more) patterns that are connected

to each other.

Step 2: Assignment of grey levels to the pixels of a 3×3 pixel pattern: The maximum

grey level (G_{white_level}) is assigned to the center pixel (pixel (2,2) in Figure 2-A1)

simulating a pixel completely covered by the white paint. The grey levels of the

surrounding 8 pixels, $G(i, j)$, are given by the following relationship
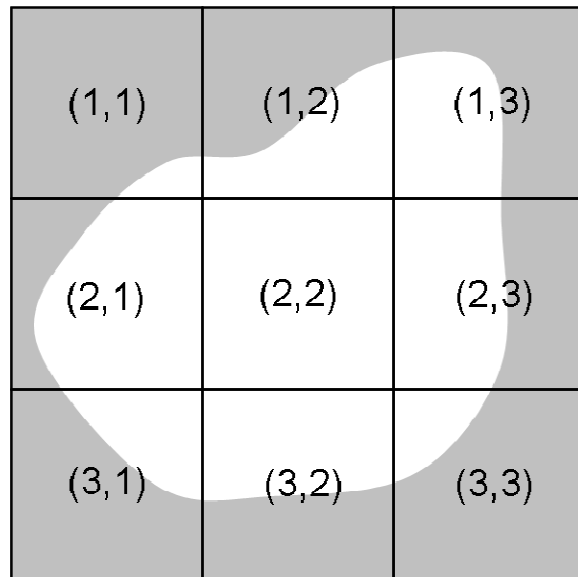
$$G(i, j) = P_{ij} \times G_{white\_level} + (1 - P_{ij}) \times G_{black\_level} \quad \text{for } i, j = 1 \text{ to } 3 \text{ except } i, j = 2$$

$$(2A\text{-}1)$$

where P_{ij} are random numbers, ranging from 0 to 1; G_{black_level} is the grey level of a

pixel simulating an area with no paint. In order to accommodate the random noise

in the simulation, G_{white_level} and G_{black_level} are 200 and 50, respectively.

Step 3: Repeat step 2 until the proper grey level are assigned to all the pixels.

Deformed configuration

The pixel at (i, j) in the undeformed configuration moves to position

$(i + u_i, j + u_j)$ in the deformed configuration, where u_i and u_j are the x and y

direction displacements defined by Eqs. (14) and (15). The sub-pixel calculation

(interpolation) is required since $(i + u_i, j + u_j)$ is not an integer. The bi-cubic

interpolation method is applied to obtain the grey level of the sub-pixel

position $(i + u_i, j + u_j)$.

47

(1,1)	(1,2)	(1,3)
(2,1)	(2,2)	(2,3)
(3,1)	(3,2)	(3,3)

2-A1

Chapter 3: Nano-Pattern Recognition and Correlation Technique for Sub-Nanometer Deformation Measurement – Part I: Basic Principles[2]

ABSTRACT

An in-plane measurement technique to measure sub-nanometer scale deformations is proposed. The proposed technique called *Nano-Pattern Recognition and Correlation Technique (N-PRCT)* utilizes regularly oriented patterns that are fabricated on the specimen surface as the media to realize the displacement measurement. The regularity offers a special benefit, relative to the random markings used in the existing technique, which makes the proposed technique much less sensitive to the random noise inherent in digital images at extremely high magnifications (a field of view less than 10 μm). The deformation measurement of thermal expansion of nano-hole template is conducted using N-PRCT. Displacements are obtained by tracking the movement of each single pattern in the images taken before and after loading through pattern recognition and correlation. The size and density of regularly oriented patterns determine the measurement accuracy/sensitivity and gauge length. The displacement measurement accuracy of approximately 0.015 nm is demonstrated with the spatial resolution of less than 3.5 nm/pixel.

---

[2] This chapter will be submitted as a research paper to *Experimental Mechanics* under the title "Nano-Pattern Recognition and Correlation Technique for Sub-Nanometer Deformation Measurement – Part I: Basic Principles", by H. Bi and B. Han.

3.1 Introduction

Deformation measurements are needed urgently in the sub-nanometer range. The need for nano-scale measurements becomes imminent as nanoscale components and interconnects are realized in actual devices, most notably in semiconductor devices. The reliability of devices is determined largely by deformations of nanoscale structures during manufacturing and operation. These are inferred by computational analysis, but informed physical analysis is vital to measure the variables and to guide and verify the computations. What is needed is full-field in-plane displacement measurements that are accurate within a fraction of nanometers, together with sub-micron length scale.

In recent years, several techniques have been proposed to document nano-scale deformations. They include electron-beam moiré (EBM) [12-16], SEM/TEM/AFM digital image correlation (DIC) [28-40], and speckle interferometry with electron microscopy (SIEM) [41,42].

The Electron Beam Moiré is a measurement technique based on "phase information," i.e., the output signal contains harmonic functions whose arguments are linearly proportional to displacements. Besides its inherent limitation on accurate determination of shear strains, EBM offers measurement sensitivity only on the order of 200 nm/fringe, which is substantially lower than that required for nano-structural deformations.

On the other hand, there is no theoretical limit in spatial resolution for DIC and SIEM. The displacement measurement sensitivity/accuracy is directly related to the physical dimension of the pixel in the digital image (spatial resolution), and thus the

displacement measurement accuracy/sensitivity can be increased continuously using higher magnifications.

These techniques are amplitude-based measurement techniques, which use the existence of distinct grayscale patterns on an object surface. The amplitude-based measurement techniques are essentially more sensitive to the background noise and are prone to produce random errors in the displacement fields when the original images contain the random noise. In general, the phase-based measurement techniques offer a higher signal-to-noise ratio since the conventional image processing schemes can be used to suppress the background random noise.

Even though SEM can offer the required spatial resolution, the random noise in SEM images is unavoidable at the extreme magnifications (a field of view smaller than 10 μm) [47]. It is important to note that the conventional high frequency random noise reduction schemes such as spatial averaging (low-pass filter) and time averaging cannot be used to suppress the random noise since the frequency of the random noise is typically on the same order of the random patterns used in DIC. A recent study has shown [47] that although the original high frequency noise can be reduced by the schemes, the high frequency signal of the original image is also affected significantly during the noise reduction process and it produces virtually the same level of random noise. Consequently the DIC will suffer from the random noise. The local displacement uncertainties caused by the random noise can be so significant that the SEM based DIC becomes unsuitable for the measurements of deformations with *strain gradients* [47].

The proposed N-PRCT is an amplitude-based technique in principle, but it utilizes pseudo-regularly oriented nano-scale patterns that are fabricated on the specimen surface as the media to realize the displacement measurement. A special benefit accrues from the regularly oriented patterns, relative to the random markings used for DIC and SIEM. The regularity allows to use the conventional filters (low-pass filter combined with Wiener Filter) to suppress effectively the inherent random noise of high-magnification SEM images, which is critically required to achieve the desired displacement measurement sensitivity/accuracy. After obtaining the virtually noise-free SEM images before and after loading (deformation), the fundamental concepts of pattern recognition and correlation are subsequently employed to determine a displacement field. In this paper, the deformation measurement of thermal expansion of nano-hole template is used to demonstrate the N-PRCT procedure.

3.2 Technical Background: Image Processing Schemes

The proposed N-PRCT utilizes numerous existing image processing schemes. They are described briefly in this section.

3.2.1 Low-pass Filter

Low-pass filter is effective to eliminate the high frequency random noise in the digital image evolved during imaging. The low-pass filter can be described in the frequency domain using two-dimensional fast Fourier transform (FFT). The two-dimensional FFT is defined as [50]

$$F(u,v) = \frac{1}{MN} \sum_{i=1}^{M} \sum_{j=1}^{N} g(i,j) e^{-i2\pi \left[\frac{u(i-1)}{M} + \frac{v(j-1)}{N} \right]} \qquad (16)$$

where (i,j) is the pixel coordinate in the spatial domain; $g(i,j)$ is the grey level of the pixel with coordinate (i,j) in the spatial domain; M and N are the number of columns and rows in the digital image; the exponential term $e^{-i2\pi \left[\frac{u(i-1)}{M} + \frac{v(j-1)}{N} \right]}$ is the basis function corresponding to each point (u,v) in the frequency domain; $F(u,v)$ is a complex number that contains the amplitude and phase information of frequency (u,v) in the frequency domain.

The FFT image processed by a low-pass filter in the frequency domain can be described mathematically as [50]

$$G(u,v) = F(u,v)H(u,v) \qquad (17)$$

where $F(u,v)$ is the FFT image of the original image; $H(u,v)$ is the FFT image of the low-pass filter; $G(u,v)$ is the FFT of the image processed by the low-pass filter.

The image processed by the low-pass filter in the spatial domain can be achieved using the two-dimensional inverse Fourier transform, which is defined as [50]

$$g(i,j) = \frac{1}{MN} \sum_{i=1}^{M} \sum_{j=1}^{N} G(u,v) e^{i2\pi \left[\frac{u(i-1)}{M} + \frac{v(j-1)}{N} \right]} \qquad (18)$$

where (u,v) is the coordinate in the frequency domain; (i,j) is the coordinate in spatial domain; $G(u,v)$ is the low-pass filtered signal in the frequency domain that contains the amplitude and phase information; and the exponential term

$e^{i2\pi\left[\frac{u(i-1)}{M}+\frac{v(j-1)}{N}\right]}$ is the basis function corresponding to each point $g(i,j)$ in the spatial domain.

3.2.2 De-blurring process: Wiener filter

Wiener filter [55-57] is an effective filter to de-blur the object boundary. Wiener filter is exceptionally effective when the degradation mechanism is known. This approach makes the filter unique in developing an application-specific restoration algorithm. Another feature of the Wiener filter, which makes the filter more attractive, is its inherent ability of band-pass filtering; which enables its capability of reducing noise. Therefore, Wiener filter executes an optimal trade-off between de-blurring and noise reduction; Wiener filter can further decrease the high frequency random noise while de-blurring.

The Wiener filter for de-blurring process can be expressed as

$$R(u,v) = \frac{X^*(u,v)}{|X(u,v)|^2 + \dfrac{P_n}{P_s(u,v)}} \tag{19}$$

where $X(u,v)$ and $X^*(u,v)$ are Fourier transform of the point-spread function and its complex conjugate, respectively. The points spread function $X(u,v)$ is the main reason that cause the object boundary blurring. $P_s(u,v)$ is the power spectrum of signal, and P_n is the average amplitude of noise frequencies; the term $\dfrac{P_n}{P_s(u,v)}$ is the reciprocal of the signal-to-noise (S/N) ratio.

The Wiener filter defined as Eq. (19) behaves as a band-pass filter during

de-blurring; a high-pass filter when $\dfrac{P_n}{P_s(u,v)}$ is small and a low-pass filter when

$\dfrac{P_n}{P_s(u,v)}$ is large. Consequently, determination of point spread function $X(u,v)$

and P_n is very important to successful implementation of the Wiener filter.

3.2.3 Image Interpolation

A sub-pixel operation is required when higher accuracy is desired. An interpolation function such as cubic-spline and bilinear interpolation functions is needed.
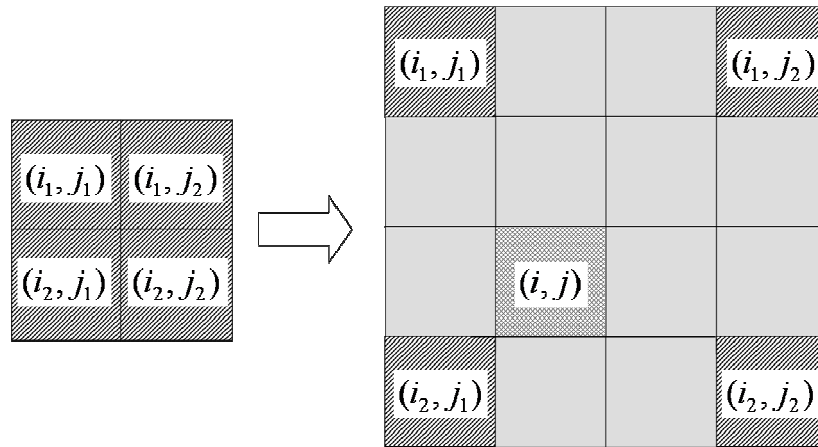
Figure 3-1 Illustration of bilinear interpolation

The sub-pixel interpolation using a bilinear function is illustrated in Figure 3-1, where the grey level of a sub-pixel pixel at (i,j), $g(i,j)$, is obtained from the grey levels of its nearest four integer pixels, $g(i_1,j_1), g(i_1,j_2), g(i_2,j_1)$ and $g(i_2,j_2)$

55

using the following bilinear interpolation function [51,52]:

$$g(i, j) = g(i_1, j_1) \times (1 + i_1 - i) \times (1 - j_1 + j) + g(i_1, j_2) \times (1 - i_1 + i) \times (1 - j_2 + j)$$
$$+ g(i_2, j_1) \times (1 + i_2 - i) \times (1 + j_1 - j) + g(i_2, j_2) \times (1 - i_2 + i) \times (1 - j_2 + j)$$

$$(20)$$

3.2.4 Boundary detection

Numerous boundary detection algorithms [51-54] are available in the literature. One of the most effective algorithms for patterns with simple structure is the pixel grey-level gradient algorithm [51,52]. The concept is expressed mathematically as

$$f(i, j) = \sqrt{\left(\frac{\partial g(i, j)}{\partial i}\right)^2 + \left(\frac{\partial g(i, j)}{\partial j}\right)^2} \qquad (21)$$

where $f(i, j)$ is the grey-level gradient at (i, j); $g(i, j)$ is the grey level at (i, j).

In the digital image, the grey-level changes fast on the object boundary; while it changes smoothly in the areas away from the object boundary. Therefore, the grey-level gradient $f(i, j)$ along the object boundary is much higher than that in other areas. Based on that, a threshold value is set as a criterion for a boundary pixel. The appropriate threshold value can be obtained from the histogram of $f(i, j)$ [51,52]. For this method the grey-level gradient value locates on the farthest peak from the origin in the histogram of $f(i, j)$ is set as the threshold value for the boundary detection.

3.3 Nano-Pattern Recognition and Correlation Technique (N-PRCT)

The image processing procedure of N-PRCT is shown in Figure 3-2. Thermal deformations of a nano-hole template are used to describe each process. The template was fabricated from a thin aluminum plate using two-step anodization processes [48,49]. It is shown schematically in Figure 3- 3(a).

A small field of the template was documented by the SEM (FEI: Quanta 200) at two different temperatures using a thermal conduction cold/hot stage (Gatan: C1002). The photo of the stage and its schematic illustration are shown in Figure 3-3(b). The thermal loading procedure will be described in more details in the companion paper [Part II].
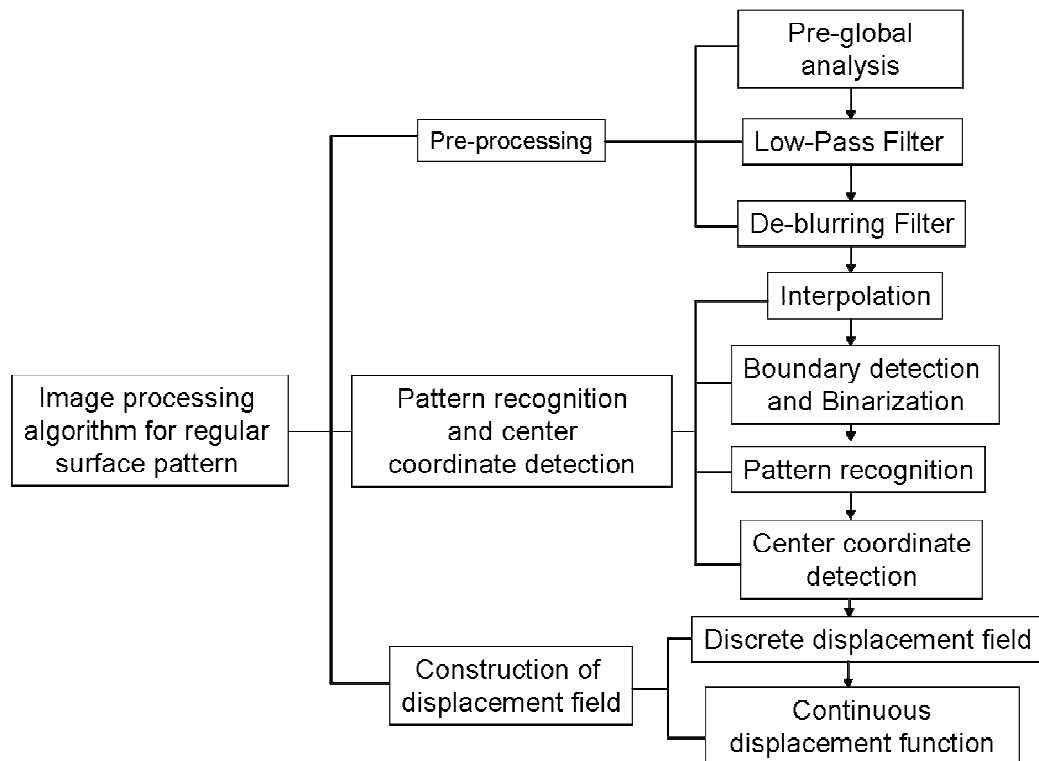
Figure 3-2 Flow-Chart of nano-pattern recognition and correlation technique
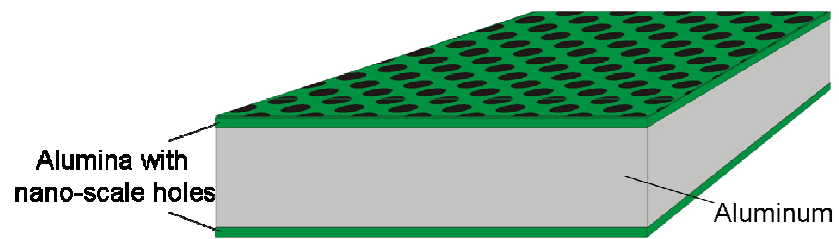
(a)
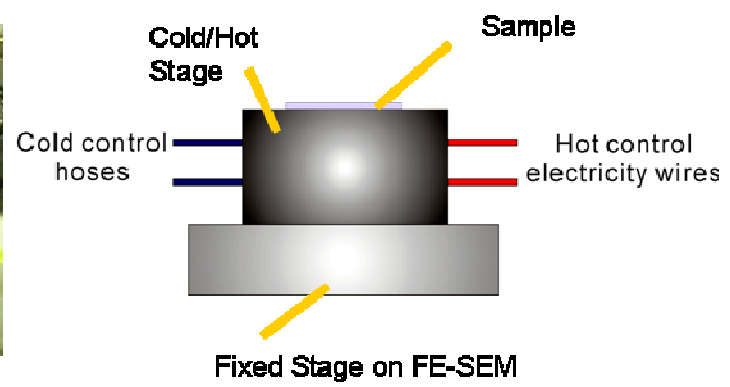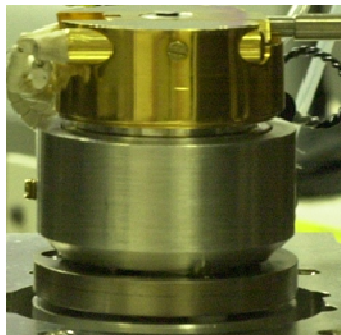
(b)
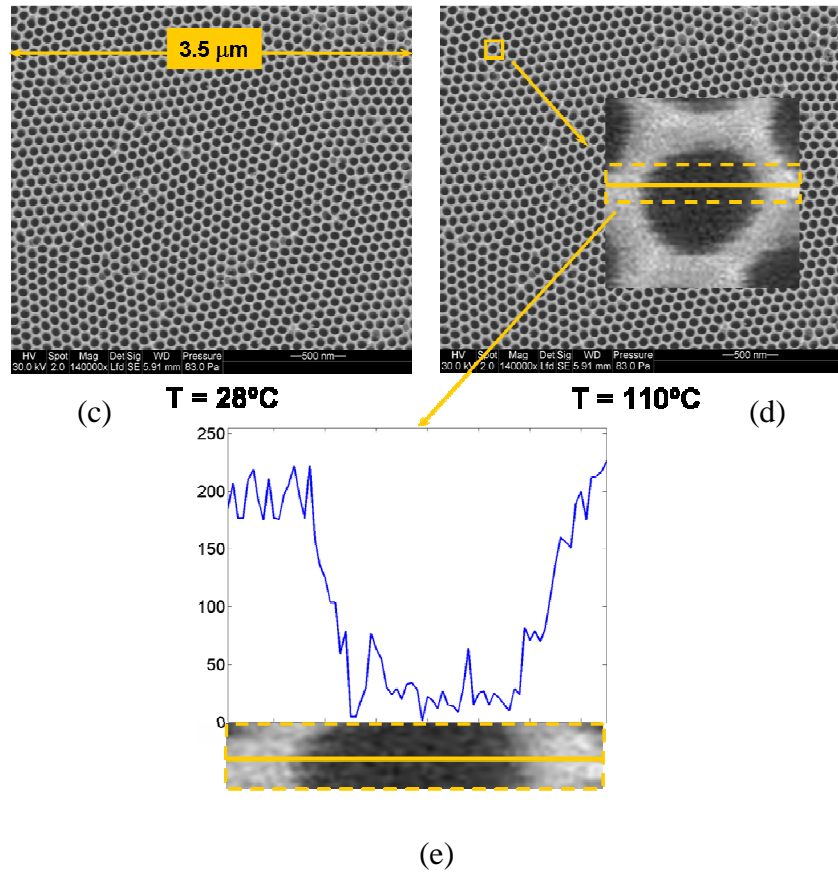
Figure 3-3 (a) Schematic illustration of nano-hole template; (b) thermal loading system; SEM images taken at (c) 28°C and (d) at 110°C ;and (e) intensity plot along the centerline of a pore.

The parameters used for SEM imaging are 30 kV voltage and spot size 2. Figure 3-3(c) and (d) show two SEM images documented at room temperature (28°C) and an elevated temperature (110°C), respectively. An intensity plot along the center line of a single pattern is also shown in (e). The intensity fluctuation caused by the SEM noise is evident.

3.3.1 Pre-Processing

Pre-global analysis

Identifying the same area of a specimen before and after loading (deformation) is not a trivial task, especially for the extremely small field of view of current interest (less than 10 μm), since the rigid-body displacements of specimen caused by loading can be as large as or even larger than the size of the field of view. The regularly oriented patterns offer a unique signature of the region of interest, which can be used to identify the same region after loading for correlation.
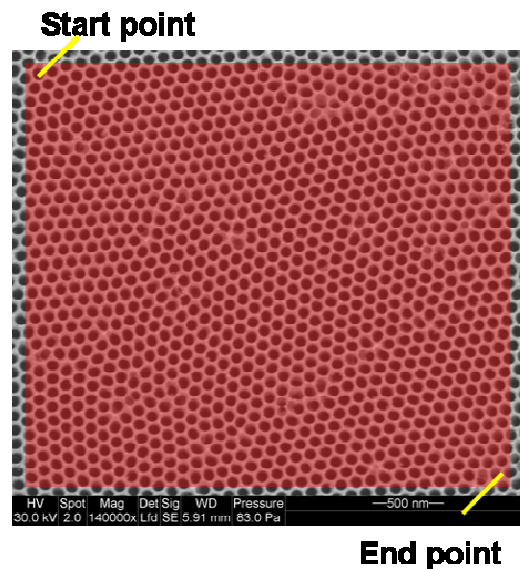
Figure 3-4 Illustration of pre-global analysis.

An example pre-global analysis is illustrated for the pattern in Figure 3-4. In the analysis, patterns that are at least 10% larger or smaller than the averaged size of patterns in the images are chosen as signature patterns. These signature patterns can be found easily from the two images before and after loading. The sub-area that covers the signature patterns in both images (thus the same area) can be identified.

This process can also minimize rigid-body displacements. The upper-left corner is first defined as the origin of digital images.   "Start point" shown in Figure 3-4 is the nearest signature pattern to the origin and "end point" is the farthest signature pattern to the origin.   The area that is diagonal from the start point to the end point encompasses the same region of interest in the images before and after deformation.

Noise elimination: combined low-pass and de-blurring filter

In the N-PRCT, displacement measurement accuracy is directly related to how precisely the pattern boundary can be defined.   Consequently, elimination of the high frequency random noise present in the high magnification SEM image [47] is required prior to the boundary detection process.

The conventional low-pass filter is an effective way to eliminate the high frequency random noise but it also results in inherent boundary blurring, which causes a detrimental effect to the boundary detection.   A de-blurring filter (Wiener filter) is employed subsequently to cope with this problem.   This uniquely combined process of reducing the high frequency SEM noise is discussed below.

The 3-order low-pass filter is applied first to eliminate the high frequency random noise.   The noise elimination process is operated in the frequency domain. Only image before loading/deformation is shown to illustrate the image processing procedure.

The FFT image of the SEM image containing the random noise is shown in Figure 3-5(a), where the color of the image represents the amplitude at each frequency.   The center point of FFT images represents the amplitude of zero

frequency signals.   This notation is used for all the FFT images.   The maximum

frequency in x and y directions are 512 Hz and 442 Hz due to the Nyquist theory

[50,51].

The FFT image processed by the low-pass filter is shown in Figure 3-5(b).   It

should be noted that the amplitude of the FFT of the SEM image (Figure 3-5a and b)

is shown in the base-10-logarithm scale due to the extremely large range of

magnitudes.   It is clear from Figure 3-5(a) that the amplitude of the low frequency

signal is much higher than that of the high frequency signal.   The two-dimensional

inverse Fourier transform (Eq. 18) is performed to produce the filtered image shown

in Figure 3-5(c).
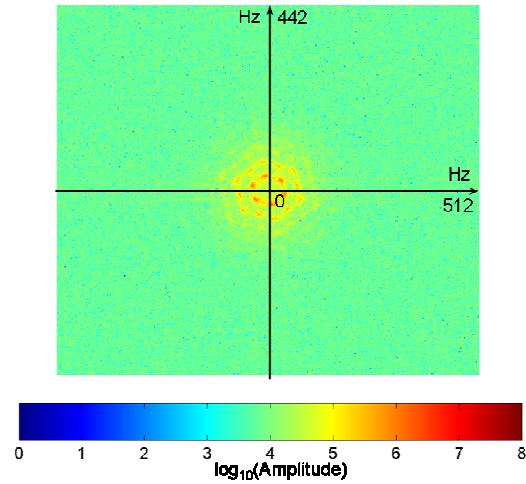
(a)
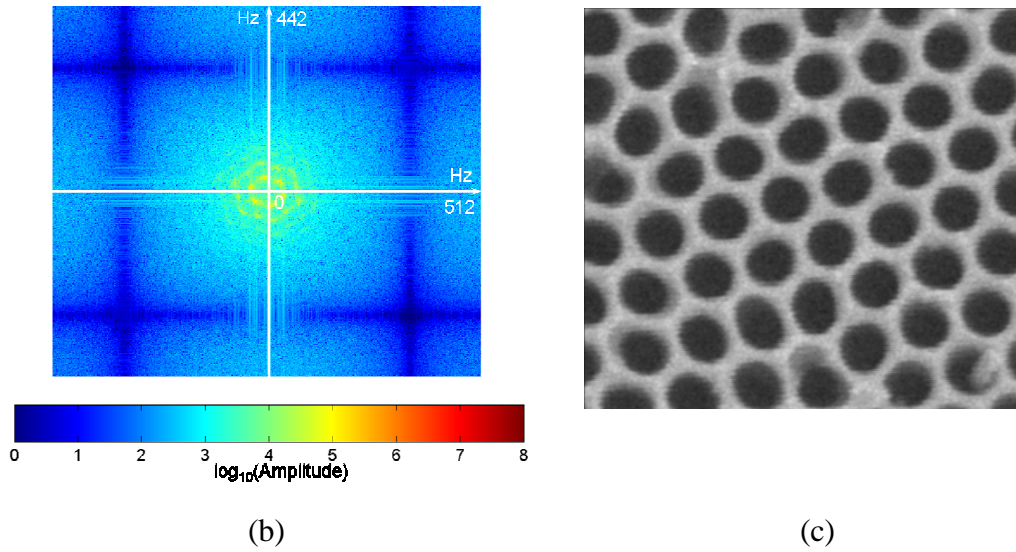
Figure 3-5 (a) FFT plot of the image of Figure 3-3(c), (b) FFT plot after low-pass filter process, (c) image after processed by low pass filter.

Although simple and effective, the low-pass filter cannot eliminate all the high frequency noise.   More importantly, the low-pass filter inherently blurs the boundaries of the objects in the image since some of the middle-range frequency signal required to define clear boundaries are also reduced during the low-pass filter processing.   The boundary blurring can be seen in the image of Figure 3-5(c).   This is precisely the reason why a higher order low-pass filter cannot be considered for further reduction of the random noise.

The boundary bluing may not be so important when fringe patterns obtained by the phase-based measurement techniques are analyzed.   However, it is critically affecting the accuracy of the proposed method.   To cope with the boundary blurring

problem, an additional filtering process is required to negate the blurring and thus to regain the original clear boundary.

For the proposed process, the objective is to reconstruct the digital image in which the object boundary is blurred due to the low-pass filtering process. Therefore, the degradation mechanism is "blurring" induced by the low-pass filter. Then, the Wiener filter for de-blurring process can be expressed as

$$R(u,v) = \frac{H^*(u,v)}{\left|H(u,v)\right|^2 + \dfrac{P_n}{P_s(u,v)}}$$

(19)

where $H(u,v)$ and $H^*(u,v)$ are the low pass filter and its complex conjugate in the frequency domain.

The random noise during SEM imaging was characterized to determine the magnitude of P_n. The SEM signal was recorded from an optical flat coated with a vacuum-deposited gold layer ($\approx$ 2 nm). In the setup, the E-beam was focused first on the specimen surface and then the specimen was translated in the vertical direction to defocus the beam intentionally. In this way, the number of electrons collected by the detector is affected only by the instability of the E-beam regardless of the nano-scale surface anomalies and the amount of drifting [47]. The image and the intensity distribution along the centerline AA' are shown in Figure 3-6(a) and (b), respectively.

The noise was transformed into the frequency domain (Figure 3-6c). Then the amplitudes of all frequencies were averaged to obtain the magnitude of P_n. The magnitude of P_n was estimated to be 236 for the SEM imaging parameter: 30 keV

and spot size 2; which were used to take the image over region of interest.

The signal power spectrum $P_s(u,v)$ is the amplitude of the filtered signal, $G(u,v)$, i.e., $|G(u,v)|$. Accordingly the de-blurring filter designed for the SEM images can be expressed as $R(u,v) = \dfrac{H^*(u,v)}{|H(u,v)|^2 + \dfrac{236}{|G(u,v)|}}$. The amplitude of the de-blurring filter is shown in Figure 3-6(d).

Figure 3-6(e) and (f) are the FFT image processed by Wiener filter and the inverse FFT image in the spatial domain, respectively. The boundary of the pattern in Figure 3-5(f) are clearer compared with the pattern in Figure 3-5(c). To illustrate the effect of each process more quantitatively, the intensity distributions of the single pattern (Figure 3-3c) are shown in Figure 3-6(g). The results clearly indicate accurate restoration of the boundary as well as further reduction of the random noise.

(a)

(b)

(c)

(d)

(e)

(f)

(g)
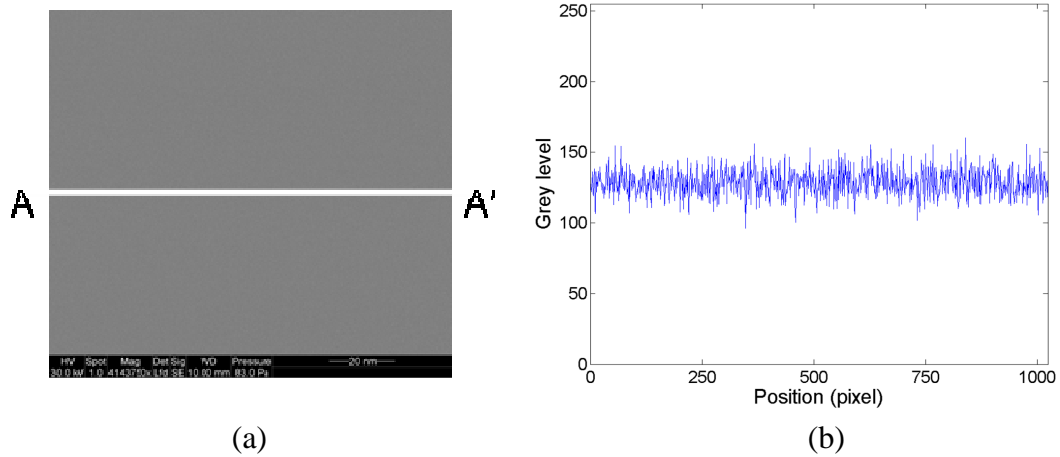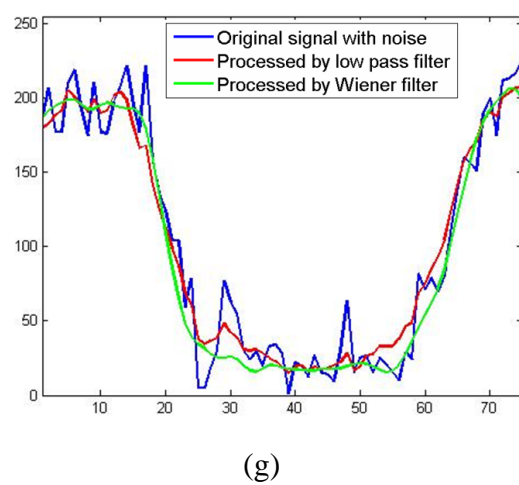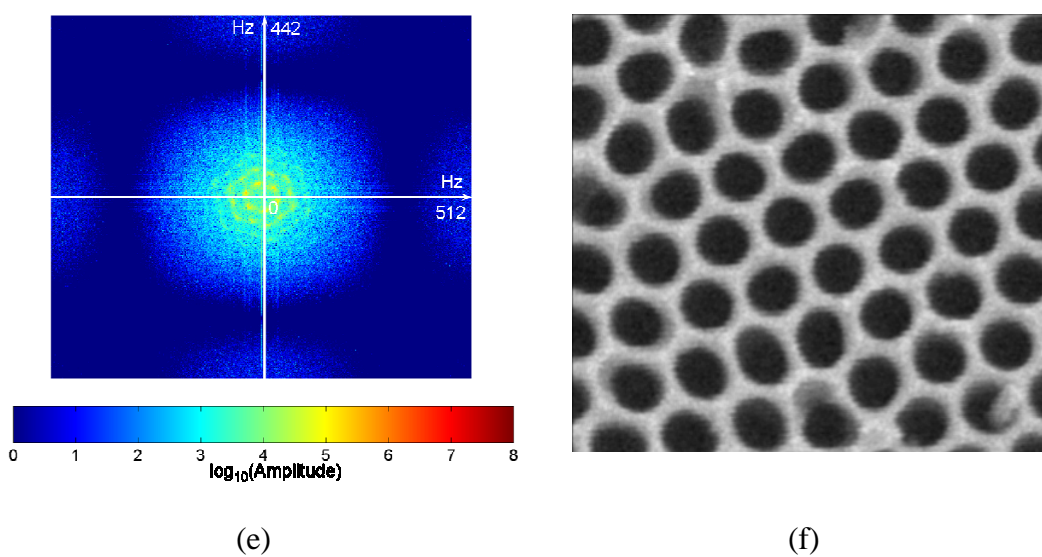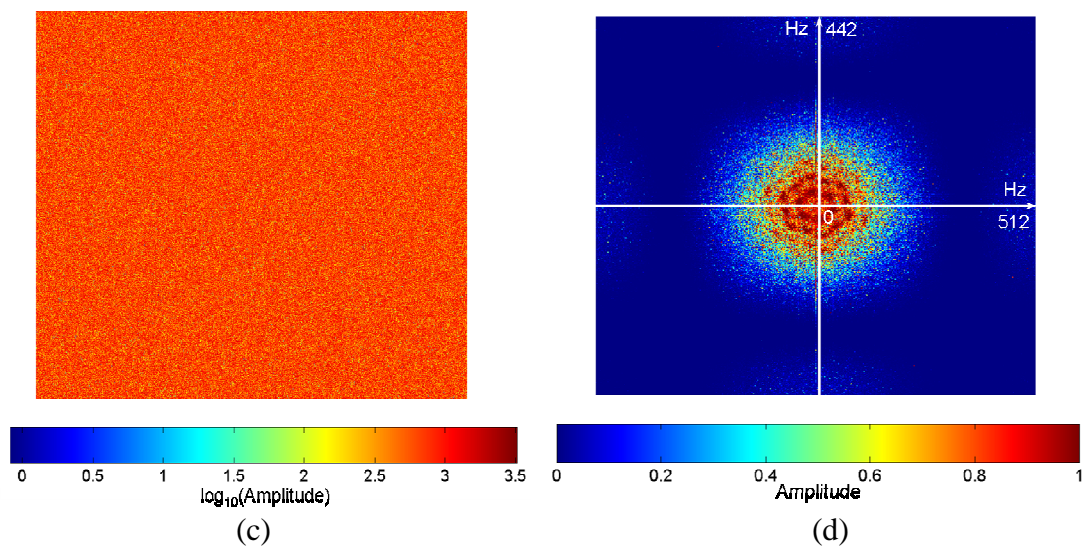
Figure 3-6 (a) SEM image for noise characterization, (b) intensity distribution along the centerline, (c) FFT plot of (a), (d) FFT plot of Wiener Filter, (e) FFT plot of image after Wiener filter process, (f) image after processed by Wiener filter, (g) intensity plots after filtering processes.

3.3.2 Pattern Recognition and Center Coordinate Detection

A series of image processing steps is followed to provide the center coordinates of patterns before and after deformations; they include boundary detection, binarization, pattern recognition, and center coordinate detection [51,52].

Boundary detection and binarization

Supplementary numerical simulations showed both cubic-spline and bilinear interpolation function were able to provide sufficient accuracy for the sub-pixel operation. In the N-PRCT, the bilinear interpolation function was selected due to its simplicity and computational efficiency [51,52]. Supplementary numerical simulations also showed that the accuracy remains virtually the same when the image magnification was larger than 7. To insure high measurement accuracy a magnification factor of 10 was chosen for the sub-pixel calculations.

The boundary detection process proceeds to determine the boundary of individual patterns using the pixel grey-level gradient (Eq. 21). For the SEM image in Figure 3-6, the threshold for detecting boundary is 106.

The result obtained from boundary detections using the sub-pixel operation and the gradient calculation is shown in Figure 3-7(a). Black and white patterns

(Figure 3-7b) are obtained by filling the area inside the boundaries.

(a)

(b)

(c)

$nUP_1(D_1, \alpha_1)$

$nUP_2(D_2, \alpha_2)$

UP
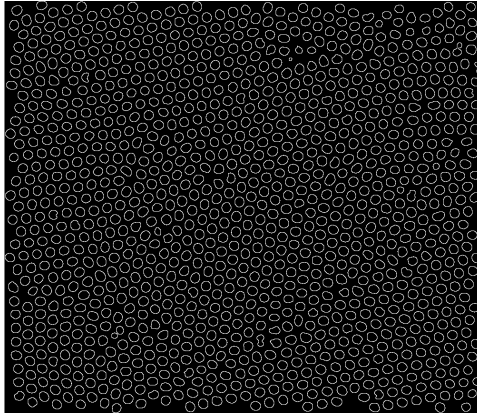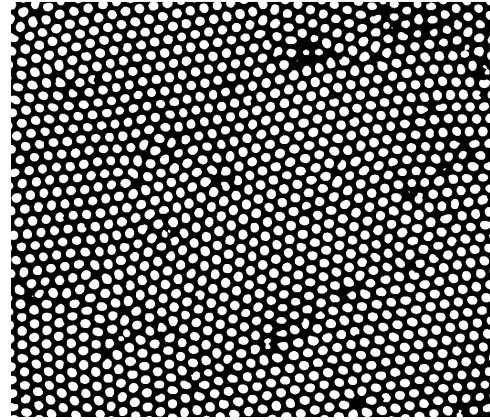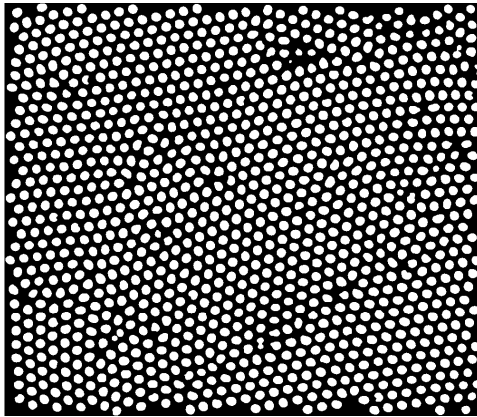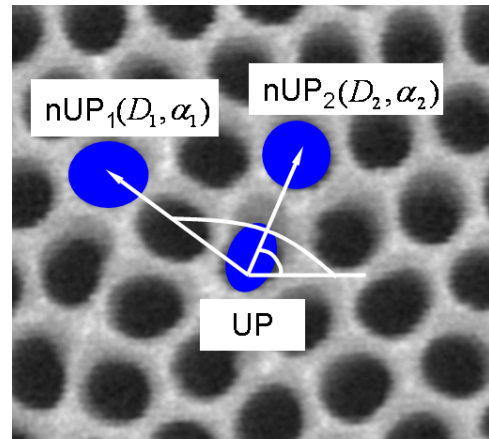
(d)
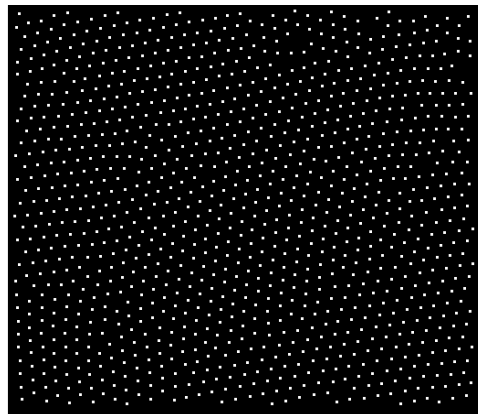
(e)

Figure 3-7 (a) Image after boundary detection using intensity gradient method, (b) black and white image after filling, (c) image after removing partial patterns along the boundary removal, (d) notations used in pattern recognition, (e) points representing the center coordinates.

Pattern recognition and correlation

Partial patterns exist along the image boundary (Figure 3-7b). These partial patterns make automatic pattern recognition and center coordinate detection difficult. Pixels with non-zero grey level are the indicator of partial patterns and they are removed before pattern recognition. The image after removing the partial patterns is shown in Figure 3-7(c).

After partial patterns being removed, the images before and after deformation are ready for pattern recognition. Figure 3-7(d) explicates the process of pattern recognition. As mentioned earlier, pseudo-regularly oriented patterns offer a unique shape signature (abnormal large size, abnormal small size, pseudo-circle, etc.), and pattern recognition is conducted based on this unique signature. The pattern that have a unique shape signature will be referred to as a *unique pattern* (UP) and other similar patterns that cannot be defined uniquely will be referred to as a *non-unique pattern* (nUP).

The UPs can be identified readily by using a general pattern recognition algorithm [51,52]. Each nUP is then recognized uniquely using its relative position to the closest UP. As illustrated in Figure 3-7(d), the relative position can be

represented by a position vector (D, α) of nUP relative to the position of UP. This relative position vector is the unique signature of nUPs. Then the patterns before and after loading can be matched without ambiguity.

Theoretically only one UP is needed for this process. Usually multiple UPs are present, which makes this process more practical. The nano-template used in the experiment has pseudo-regularly oriented structure, which provides many Ups. For the image shown in Figure 3-7(b), there are 66 UPs out of approximately 1200 patterns.

Center Coordinate Detection

After obtaining matching patterns between the images before and after loading, center coordinate detection for each pair of matching patterns proceeds. The first step is to identify to which pattern each pixel belongs. The eight-connected algorithm [51,52] is adopted for this process because of its effective performance for various patterns. Then the center coordinate of the pattern is determined by averaging the coordinates of all pixels in the pattern. It can be expressed mathematically as

$$
\begin{cases}
x_i = \dfrac{\sum\limits_{j=1}^{n} Cor\_x_i(j)}{n} \\
y_i = \dfrac{\sum\limits_{j=1}^{n} Cor\_y_i(j)}{n}
\end{cases} \tag{22}
$$

where (x_i, y_i) is the center coordinate of the ith pattern and $(Cor\_x_i(j), Cor\_y_i(j))$ is the coordinate of the jth pixel of the ith pattern, and n

is the total number of pixels in the ith pattern. Figure 3-7(e) shows the center points of each pattern in the image shown in Figure 3-7(c).

3.3.3 Construction of Displacement and Strain Contour

As a final step, the displacement field can be calculated using the following simple relationship:

$$\begin{cases} D_{i,x}(x_i, y_i) = x_i' - x_i \\ D_{i,y}(x_i, y_i) = y_i' - y_i \end{cases} \tag{23}$$

where $D_{i,x}(x_i, y_i)$ and $D_{i,y}(x_i, y_i)$ are the displacement components in the horizontal and vertical directions, respectively; (x_i, y_i) and (x_i', y_i') are the center coordinates of matching patterns before and after deformations. The displacement components are plotted in Figure 3-8(a) and (b), where the length of arrows indicates the magnitude of the displacements.

(a)   (b)

71

(c)   (d)
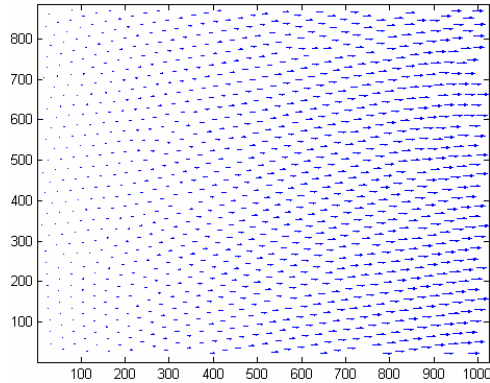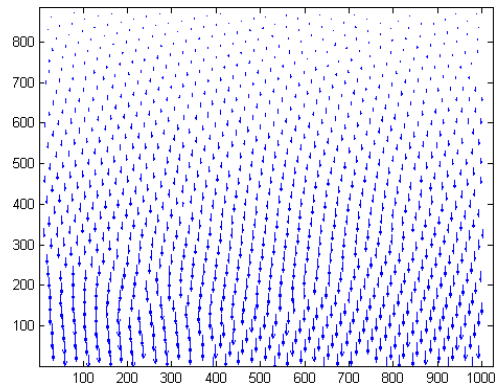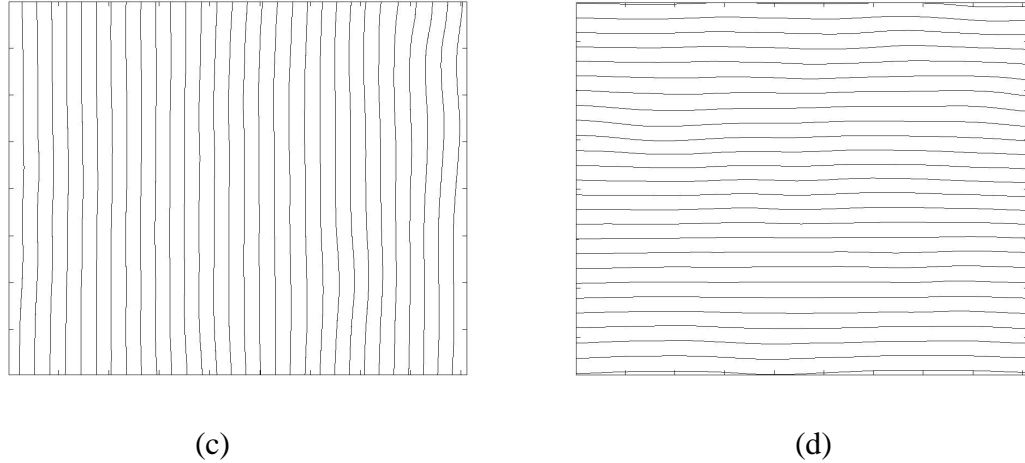
Figure 3-8 Discrete displacement plots in (a) the horizontal and (b) the vertical directions. Displacement contours in (c) the horizontal and (d the vertical directions.

With the N-PRCT, displacements are determined at discrete points (the center positions of each pattern). Furthermore the discrete points are not uniformly distributed. The thin-plate smoothing spline interpolation technique is known to be most effective for randomly distributed discrete data. It is adopted to produce a continues displacement field [59-61], which is shown in Figure 3-8(c) and (d) for horizontal and vertical direction, respectively. Strain components can be determined by the displacement and engineering strain relationship.

The displacement of the template over the whole gage length is approximately 5.94 nm. Using the rule of mixture, the displacement of the composite nano-template can be estimated as:

$$u = \alpha_{eff} \times \Delta T \times L = \frac{\sum \alpha_i V_i E_i}{\sum V_i E_i} \times \Delta T \times L$$

$$= \frac{23.6 \times 327 \times 70 + 6.2 \times 10 \times 410}{327 \times 70 + 10 \times 410} \, ppm \times 82 \times 3509 = 6.03 \, (nm)$$

(24)

where the temperature change ΔT is 82°C; the horizontal dimension of the field of view L is 3.509 μm; the CTE of aluminum is 23.6 ppm; the CTE of Al_2O_3 is 6.2 ppm [62]; the volume of aluminum is 327 μm $\times$ 7 mm $\times$ 7 mm; the volume of alumina is 10 μm $\times$ 7 mm $\times$ 7 mm; Young's modulus of aluminum is 70 GPa; Young's modulus of alumina is 410 GPa [62]. The experimental value matches the estimated value very well, which establishes the global measurement accuracy of the N-PRCT.

3.4 Discussion: Resolution of N-PRCT

Computer simulations using regularly oriented ideal patterns are conducted to address the theoretical displacement measurement accuracy of the N-PRCT. An example of ideal patterns is shown in Figure 3-9. In the figure, the diameter of a single pattern is d_p (in pixel); the distance between two adjacent patterns is r (in pixel); and the gauge length, L_g, defined as the minimum distance between two adjacent data points, is the center to center distance of two adjacent patterns (i.e., $L_g = d_p + r$). The spatial resolution of digital images, R_s, can be defined as

$$R_s = \frac{L}{N}$$

(25)

where L is the physical dimension of a field of view, and N is the number of pixels used to represent the length L; the spatial resolution can be interpreted as the physical dimension that a single pixel represents.
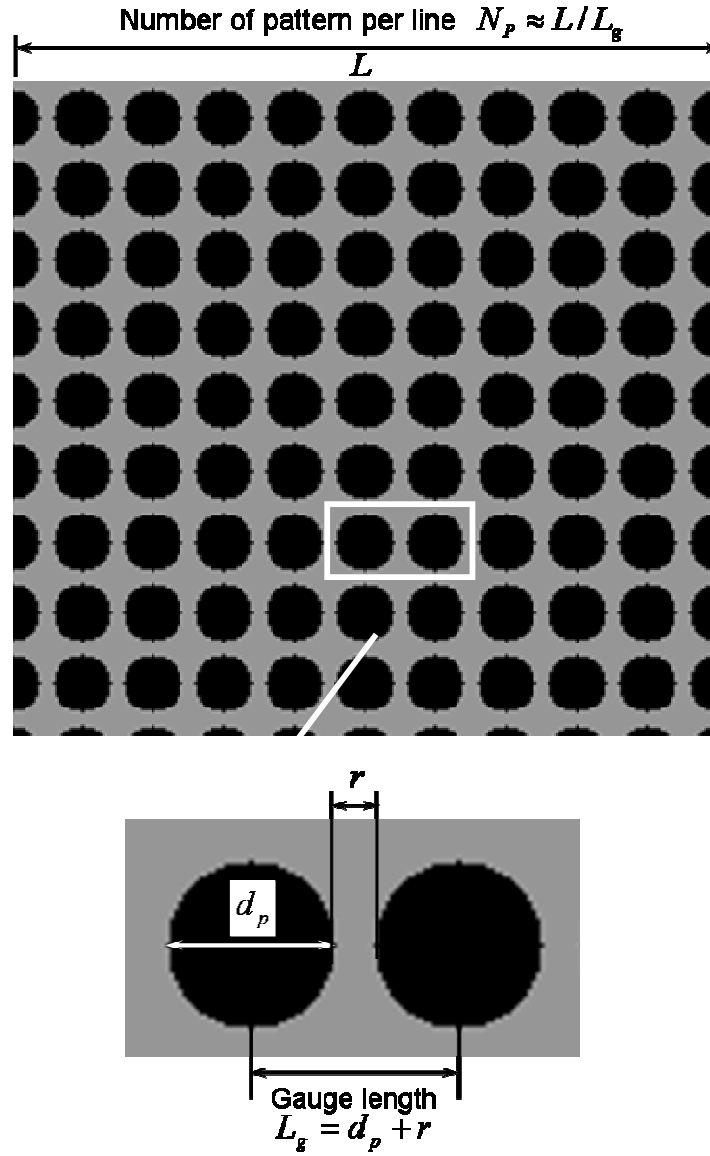
Figure 3-9 Regularly oriented patterns used in the simulation

The displacement measurement accuracy (or sensitivity) is directly related to the accuracy of the center coordinate detection. Consequently, the accuracy increases as the size of a single pattern, d_p, increases. However, it also increases the gauge length and the number of data points in the field of view is reduced, which is not desired for a non-uniform deformation field.

The theoretical relationship among these experimental parameters is summarized in Figure 3-10(a) (in pixel). The plot provides the corresponding displacement accuracy, δ, for a given pattern diameter, d_p (or a given gauge length, L_g). It also provides the number of patterns per line, N_p, which can be estimated as $\dfrac{L}{L_g}$.

It should be noted that the pattern diameter should be smaller than the gauge length. The line in Figure 3-10(a) is the extreme case where the pattern diameter is equal to the gage length (i.e., $r = 0$). The shaded region under the line defines the applicable domain of the N-PRCT. In practice, the domain becomes smaller as r has a finite value.

In the simulation, a uniform deformation field is used to determine the displacement sensitivity/accuracy. For a given computer generated digital image with regular oriented patterns (reference image) the theoretical displacement for each pixel in the image can be calculated. Bilinear interpolation function is employed to add the displacement in the reference image and create the deformed image. Using the N-PRCT, the displacement can be measured using the reference image and

deformed image. Therefore, the accuracy or sensitivity can be obtained by comparing the theoretical displacement and measured displacement.

The application used in the paper has a field of view of about 3.5 μm (in the horizontal direction). The number of pixels in the digital image is 1024 pixels. Using Eq. 25 the spatial resolution is determined as $R_s = 3.42 nm/pixel$. The accuracy plot for the field of view of 3.5 μm can be obtained by converting the pixel into the physical dimensions (multiplying by 3.42 nm/pixel). The results are plotted in Figure 3-10(b). The hole diameter of the nano-hole template and the gauge length are $d_p = 81 \pm 5 nm$ and $L_g = 101 \pm 5 nm$; the corresponding displacement accuracy is $\delta = 0.015 \pm 0.001 nm$ and approximately 34 data points can be obtained per line (Figure 3-10b).

(a)

76
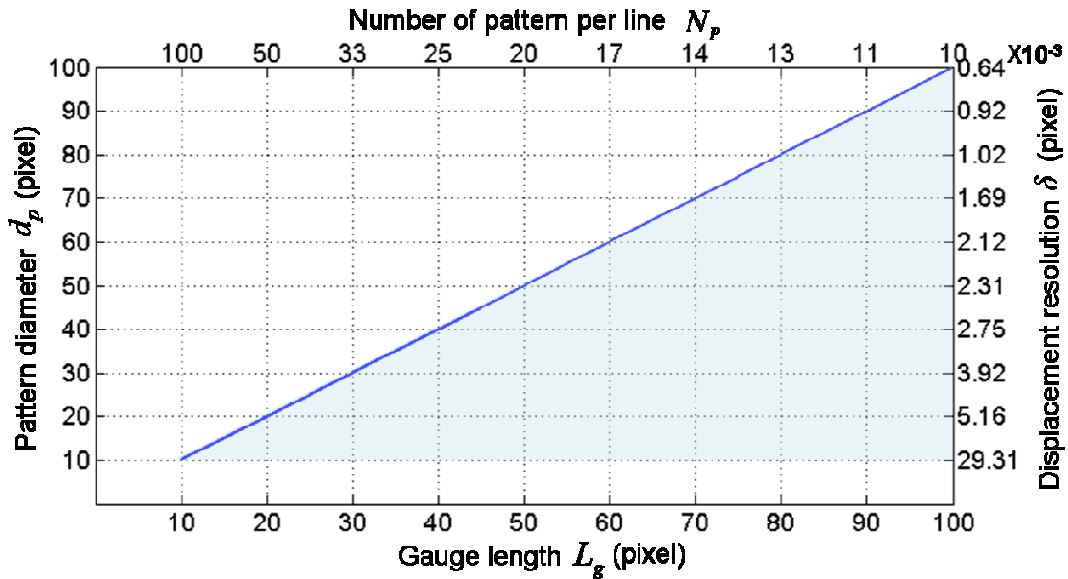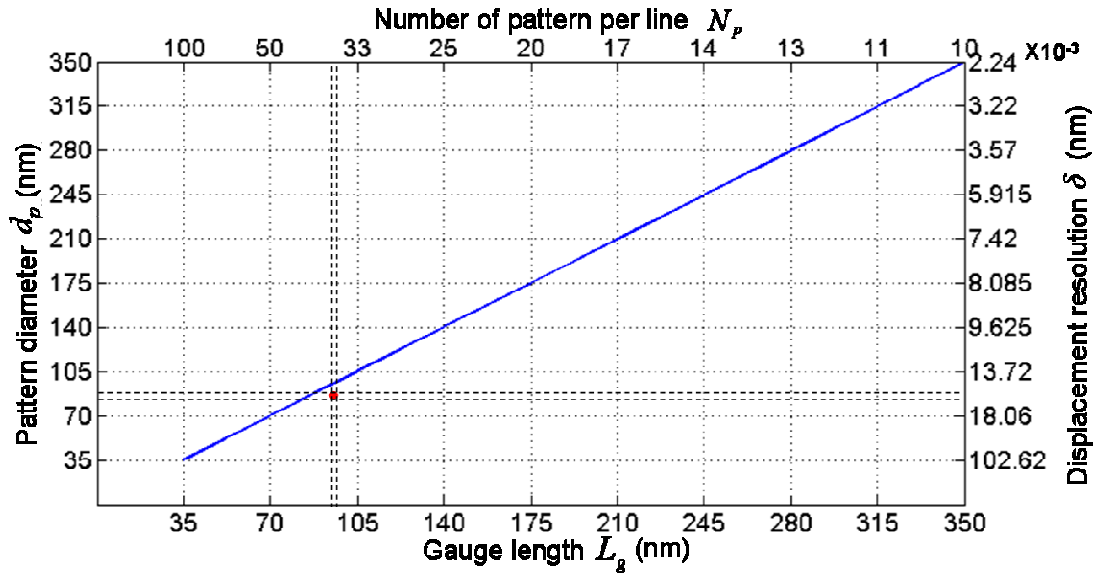
(b)

Figure 3-10 (a) Theoretical relationship among the experimental parameters. The displacement resolution and the gage length used in the experiment is shown in (b).

3.5 Conclusion

An in-plane measurement technique called *Nano-Pattern Recognition and Correlation Technique (N-PRCT)* has been proposed to measure sub-nanometer scale deformations. The detailed procedures of the proposed method were described and illustrated using the SEM images at extreme magnification (3.5 µm region of interest), taken from a nano-hole template. Computer simulations were conducted to address the theoretical displacement measurement accuracy. The preliminary experimental results presented in the paper provided the displacement measurement accuracy of approximately 0.015 nm with the spatial resolution of less than 3.5 nm/pixel.

Chapter 4: Nano-Pattern Recognition and Correlation Technique for Sub-Nanometer Deformation Measurement – Part II: Implementation for Thermal Deformation Measurements of Microelectronics Circuits[3]

ABSTRACT

The Nano-Pattern Recognition and Correlation Technique (N-PRCT) proposed in the first part of the paper is applied to measure thermally-induced nano-scale deformations of microelectronics circuits. A unique practice of E-Beam lithography is proposed and implemented to fabricate regularly oriented patterns required for the N-PRCT technique using PMMA as an E-beam resist. The proposed scheme utilizes the standard SEM for imaging to fabricate the patterns without the need of specially designed E-Beam lithography system, which makes the implementation of N-PRCT practical. Sub-100 nanometers to the micron scale regularly oriented patterns can be produced. The patterns are produced on the well-polished cross-section of a flip-chip package. Thermal deformations with the displacement measurement accuracy of about 0.1 nm are obtained in a field of view of 7 μm. The

---

[3] This chapter will be submitted as a research paper to *Experimental Mechanics* under the title "Nano-Pattern Recognition and Correlation Technique for Sub-Nanometer Deformation Measurement – Part II: Implementation for Thermal Deformation Measurements of Microelectronics Circuits", by H. Bi and B. Han.

results show a shear strain concentration at the interface between the passivation layer and the adjacent metal pad.

4.1 Introduction

An imperative need exists for deformation data from interconnects of silicon devices. The need for nano-scale measurements becomes more urgent as the interconnect technology approaches the 50 nm node and beyond. The reliability of microelectronic devices is determined largely by thermal and mechanical deformations of interconnect layers, which are inferred by computational analysis. Simplifications and uncertainties in the computational analyses are inevitable. Informed mechanical analysis is vital to measure the variables and to guide and verify the computations. Nano-scale deformation measurements are needed on the sub-micron scale with a sub-nano meter displacement resolution.

A new full-field in-plane displacement measurement technique called the *Nano-Pattern Recognition and Correlation Technique (N-PRCT)* [63] has been proposed to achieve the goal. The first part of this study described in detail the principles of N-PRCT. The objective of this second part is to study the thermally-induced deformation of the passivation layer/metal pad interface in a flip-chip package under high-temperature condition using the N-PRCT.

The N-PRCT utilizes regularly oriented patterns that are fabricated on the specimen surface as the media to realize the displacement measurement. A unique practice of E-Beam lithography is proposed and implemented to fabricate the regular patterns on a specimen surface. The proposed scheme utilizes a standard SEM for imaging to fabricate the patterns without the need of specially designed E-Beam

lithography system, which makes the implementation of N-PRCT practical. The detailed N-PRCT procedure to obtain deformation fields using the nano-patterns, and the results will be discussed in the body of the paper.

4.2 E-Beam Lithography for Regularly Oriented Patterns

4.2.1 Background

E-beam lithography (EBL) is a well-established technique for nano-structure fabrication [66-69]. It has been extended successfully to fabricate regularly oriented structures [68,69]. Figure 4-1 illustrates schematically E-Beam lithography. The E-beam is focused on a specimen surface and exposes an E-beam sensitized material coated on the surface. During SEM imaging, the E-beam spot stays at an area for a period of time known as the dwelling time and then moves to the next area. Figure 4-1(a) shows the areas in black where the E-beam remained under dwelling time. The time it takes for the E-beam to move from one area to another is extremely short, and so the exposure is negligible; these areas are shown in grey in Figure 4-1(a).

Figure 4-1(a) shows the areas that have been exposed to E-beams (in black) and the areas that have not been exposed (in grey). After a proper developing process, the regularly oriented patterns can be fabricated. A schematic illustration of the patterns fabricated using the proposed practice of E-beam lithography is shown in Figure 4-1(b).

Two E-beam resists are most widely used; they are SU-8 and PMMA. SU-8 is a negative E-beam resist that is extremely sensitive to electrons; it takes only very small electron doses to fully expose SU-8 [70]. However, the resolution of SU-8 is

in the range of only the sub-micron scale. This limits the region of interest to the range of tens of microns. On the contrary, PMMA can provide resolutions of sub-100 nm [71] but requires much larger doses for full exposure; typically 10 times compared to SU-8.

The most important parameter affecting the pattern size is the E-beam energy and the exposure dose. With the E-beam energy is low (less than 5 keV) and thus the primary electron energy is low, the forward scattering in the resist layer is dominant, which results in the spreading of the electron beam and a consequent loss of resolution [73,74]. The exposure area usually becomes much larger than the E-beam spot. This phenomenon is known as the proximity effect, which often causes features written by the E-beam to be wider in densely patterned areas [74]. With an increased electron energy (higher than 25 keV), most of the forward scattering takes place in the substrate, which helps reduce the proximity effect. Consequently, higher-energy E-beam is desired to fabricate smaller features (sub-100 nm).

In the original approach to produce regular nano patterns [68,69], a special EBL system (RAITH150 EBL system) was utilized. In Ref. [68], a relatively low-energy (5 kV) E-beam was used to fabricate the pattern on PMMA. A pattern size of about 600 nm in diameter with gauge length of 2000 nm over an area of 50×50 by μm was reported. In Ref. [69], SU-8 resist was used for patterning with the same EBL system but with a higher energy (10 kV) E-beam. A final pattern size of approximately 100 nm was obtained over an area 1×1 mm but the gauge length

was nearly twice large as the final pattern size ($\approx$ 200 nm) due to the larger initial

pattern size ($\approx$ 180 nm) [65].

The current applications of interest deal with a region of interest typically less

than 10 μm, and a smaller pattern size (and thus a smaller gage length) is desired.

More importantly, a special EBL system is not readily available for routine practice.

To cope with the problems, a unique practice of E-Beam lithography using a standard

SEM is proposed to fabricate regular patterns smaller than reported in the literature.

(a)

(b)
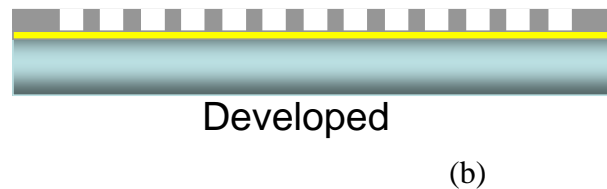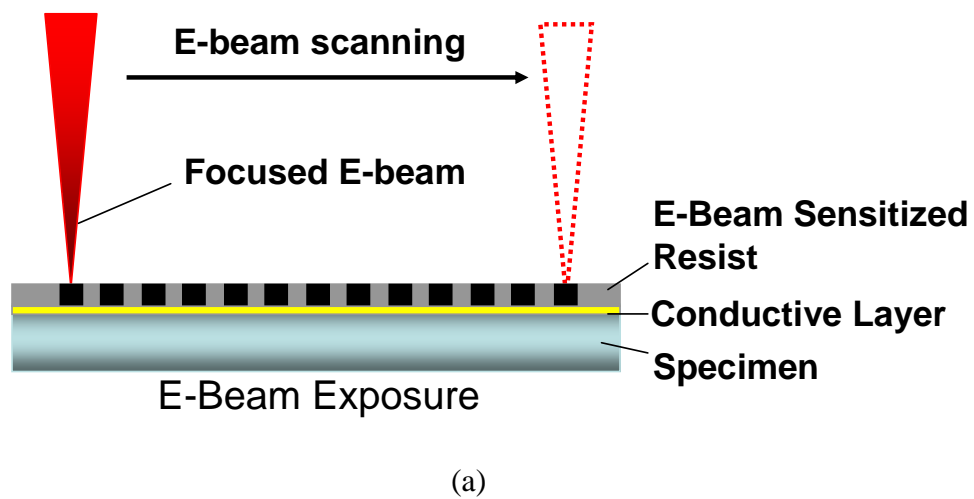
Figure 4-1 Schematic illustration of the proposed unique practice of E-beam lithography: (a) E-beam exposure (b) patterns after developing

4.2.2 E-beam Lithography Using Standard SEM

SEM imaging is actually an E-beam scanning process, which provides E-beam exposure. This standard SEM imaging process is used to fabricate nano-patterns using PMMA.

The smallest pattern can be made at the highest E-beam energy and the smallest exposure dose (or dwelling time) to minimize the proximity effect. The standard SEM used in this study (FEI Quanta 200) offers the maximum energy of 30 keV and the smallest beam size of 0.4 nm.

Figure 4-2 shows the feature size written on the PMMA as a function of exposure time at the condition of the maximum energy and the smallest beam size. As expected, the feature size increased as the dwell time increased. The minimum exposure time of 100 μs was determined as the optimum dwell time.
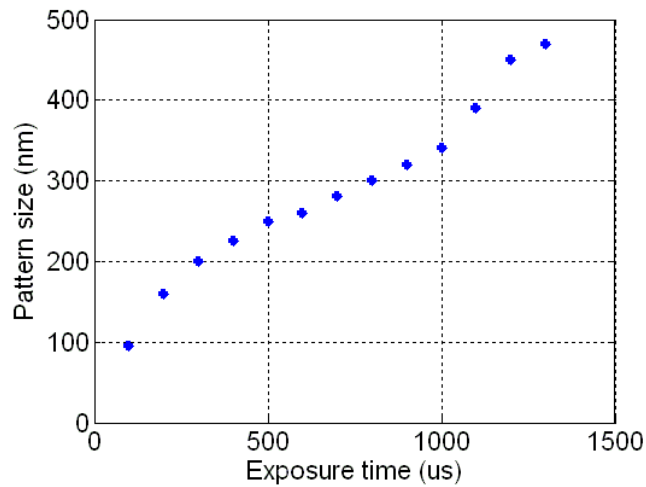
Figure 4-2 Pattern size Vs. Exposure time

It should be noted that a thin gold layer (~ 2 nm) is sputtered using sputtering machine before PMMA is coated on the specimen surface.   This gold layer helps discharge the electrons trapped in the PMMA layer, which reduces electron reflection (also called backscattered electrons) and thus further reduces the proximity effect to fabricate the small pattern.   The smallest pattern fabricated on a glass substrate is shown in Fig. 4-3, which was around 100 nm.   The uniformity is evident.
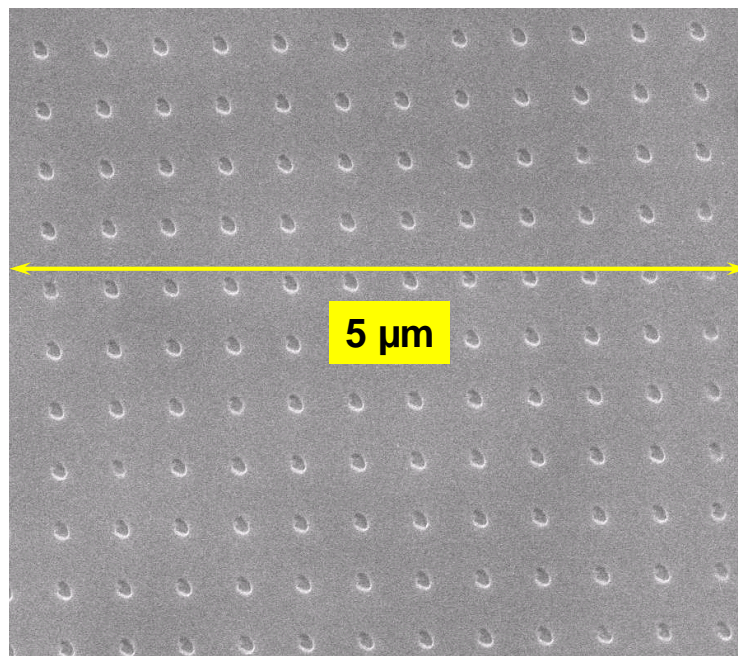
Figure 4-3 Regularly oriented patterns fabricated using proposed unique practice of E-beam lithography: ~100 nm pattern

4.3 Nano Pattern Fabrication for N-PRCT

A flip-chip package is illustrated schematically in Fig. 4-4. A silicon chip (11.94 mm × 11.94 mm × 0.715 mm) is attached to an organic substrate through tiny solder bumps. The gap between the chip and the substrate is filled with an epoxy underfill to reduce the strains of solder bumps. A strip configuration was prepared from the package, containing five central rows of solder bumps. One side was ground to produce a flat, smooth surface. The cross section is illustrated in Figure 4-4(b).

(a)

(b)
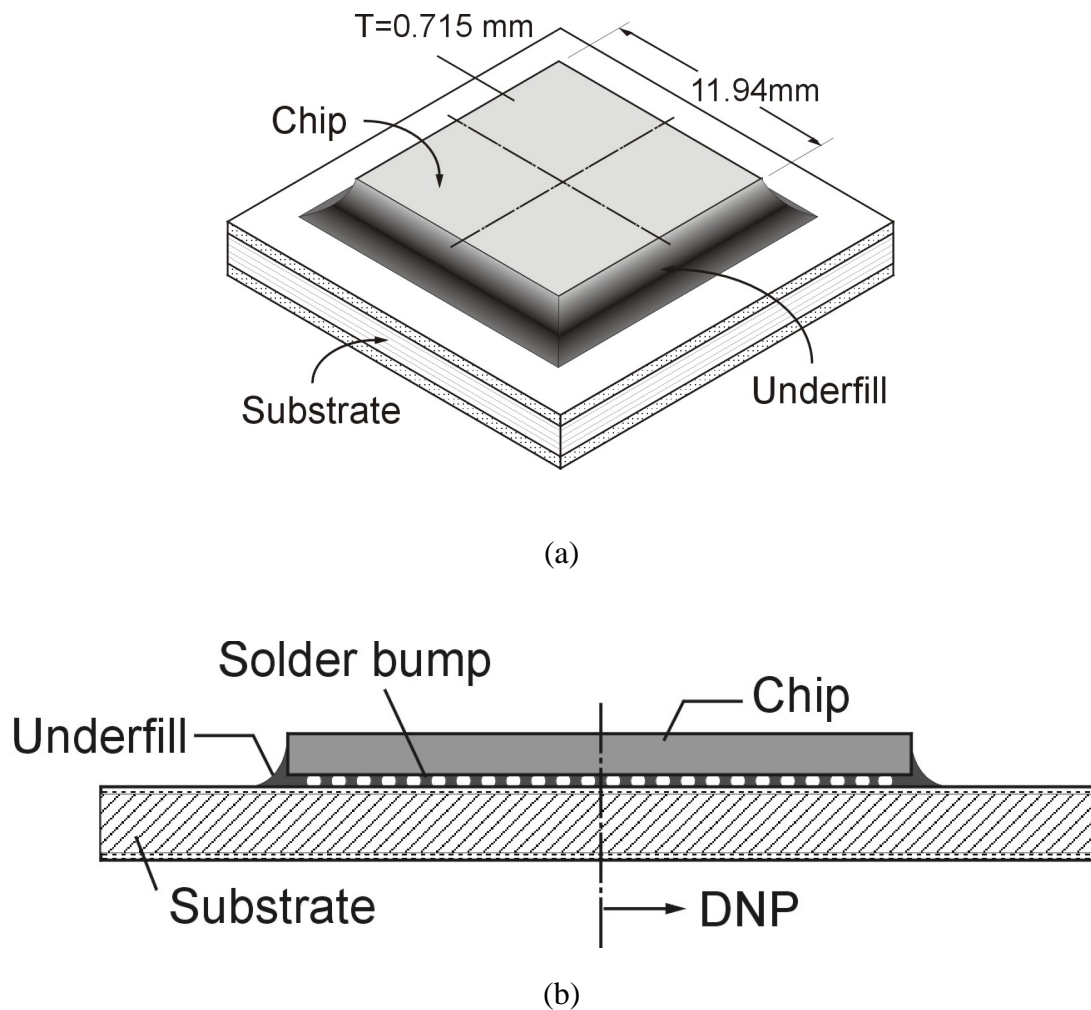
Figure 4-4 (a) 3-D view of flip-chip (b) cross-section view of flip-chip

The surface of the specimen cross-section should be as flat as possible to avoid unevenness in the resist layer during spin coating. Normally, grinding-paper finer than 600 grits/inch is used to grind the specimen cross-section as the first step. Grinding cloths and grinding suspension fluids with finer grinding particles are then used to fine-polish the cross-section. The flip-chip package used in this paper was fine-polished using an Allied 1-micron diamond suspension and 50 nm colloidal silica suspension grinding fluid after coarse-polishing with 600 grits/inch and 1200 grits/inch grinding paper.

Figure 4-5 shows several SEM images of the fine-polished flip-chip package cross-section at various magnifications. No visible scratches are seen in the region where the displacement/deformation will be measured. The final image of Figure 4-5 shows the region of interest on which the regularly oriented nano patterns are fabricated.

As mentioned earlier, a thin gold layer is sputtered on the specimen cross-section surface before spin-coating the PMMA. Besides the discharging function, the layer offers the uniformity of the specimen surface, which contains various conductor and insulators. This layer allows to produce the uniform patterns over the field of view.

A 100 nm-thick PMMA layer was spin-coated an on top of the conductive gold layer using a spinner machine (Specialty Coating System Inc, P-6000 spin coater). The PMMA layer was prebaked at 170 ºC for 30 minutes and was exposed to the condition optimized during the preliminary experiment [72].

86
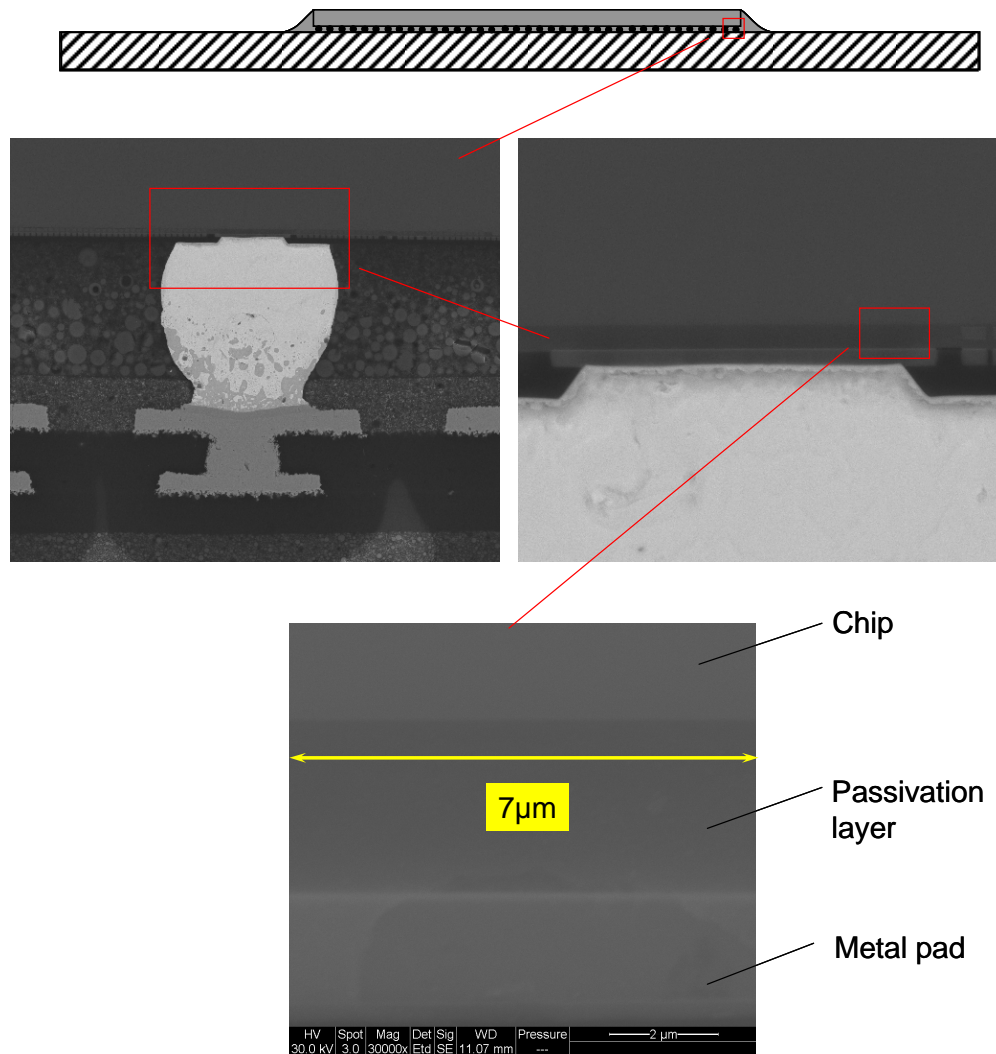
Figure 4-5 Region of interest on which patterns are needed to be fabricated

The exposed PMMA with specimen was immersed in the developer (Microchem 1:3 MIBK to IPA) for 30 seconds for developing the patterns. And the specimen was then post baked at 95 ℃ for 30 minutes [72]. Another conductive gold layer (~ 2 nm) was coated for SEM imaging.

The SEM image of the patterns fabricated on the flip-chip specimen cross-section is shown in Figure 4-6(a).   The pattern size is about 115 nm in diameter.   In the 7µm ×6µm region of interest there are about 55 patterns per line, for a total of about 2600 data points in the whole field.   This region of interest includes chip/passivation layer/aluminum pad.   The SEM image at high temperature (108 ºC) is shown in Figure 4-6(b).   The thermal loading will be discussed in the next section.

(a)   (b)
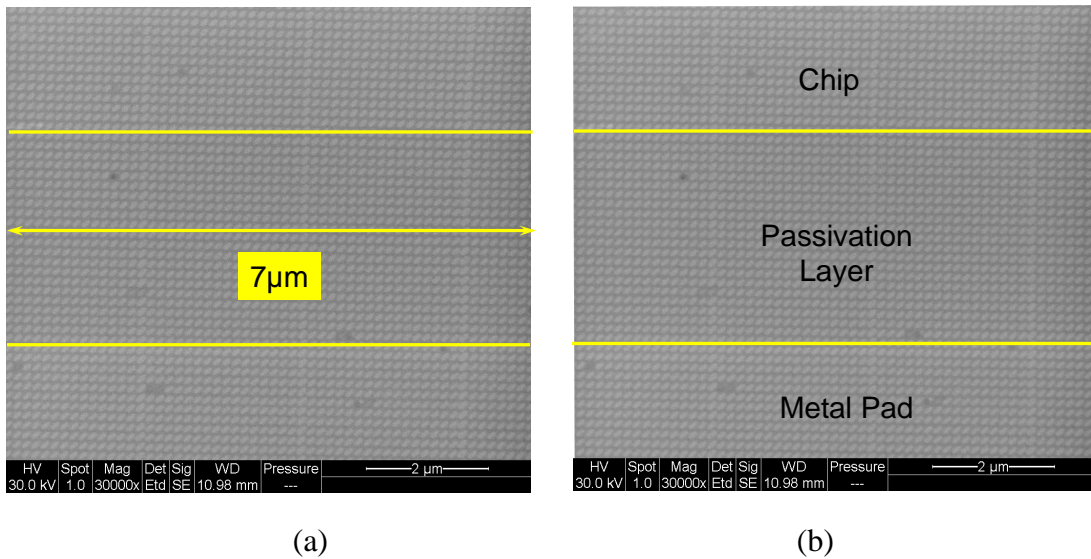
Figure 4-6 SEM images of region of interest (a) before loading (23 ºC) (b) after loading (108 ºC)

4.4 Deformation Measurements

4.4.1 Experimental Setup for Thermal Loading

The specimen was loaded inside the SEM.   Figure 4-7(a) shows an image of a specially designed thermal conduction stage (Gatan C1002) for SEM (on the left side) and its schematic illustration (on the right side).   As shown in the schematic

illustration in Figure 4-7(a), thermal loading was realized through thermal conduction: heating through electrical power and cooling through liquid nitrogen. Through a rear cap on the SEM chamber, the plastic cold control hoses were connected to the liquid nitrogen tank that is positioned outside of the SEM chamber. The electrical connection wires were also linked to the control panel through this rear cap. These plastic hoses for liquid nitrogen can apply enough force on the thermal conduction stage to cause the thermal conduction stage to become unstable or to rotate during SEM imaging. Therefore, during the experiment the plastic cold control hoses were positioned to be as flexible as possible to eliminate the force on the stage.
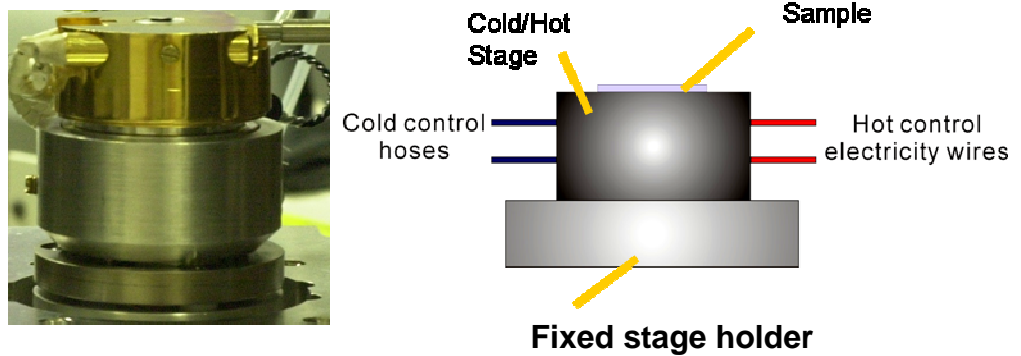
(a)
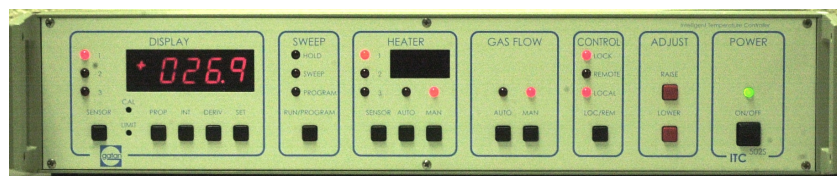
(b)

Figure 4-7 (a) Thermal conduction stage in SEM chamber, (b) Picture of external control panel for thermal conduction stage in SEM chamber

The specimen was positioned on the stage using carbon double-sided tape. To make specimen sit stably on the stage, a small metal block was used as a sample lean holder. The temperature of the thermal conduction stage was controlled through the external control panel, which is shown in Figure 4-7(b).   The temperature for the thermal conduction stage ranged from -200 ^{o}C to +200 ^{o}C.

4.4.2 Experimental Results

Figure 4-6(a) is the SEM image of the region of interest at room temperature (23°C).   Another SEM image of region of interest at a higher temperature (108°C) was taken and is shown in Figure 4-6(b).

The original SEM image with noise involved during SEM imaging is shown in Figure 4-8(a).   To eliminate the high-frequency random noise caused by SEM imaging, the image was then processed by a 3×3 low-pass filter.   The image after being processed by low-pass filter is shown in Figure 4-8(b).   This process, however, also blurred the pattern boundary.

The image processed by the low-pass filter was subsequently processed by a Wiener filter for the pattern boundary de-blurring.   The Wiener filter designed for boundary de-blurring is based on Equation 26 [64]:

$$R(u,v) = \frac{H^{*}(u,v)}{\left|H(u,v)\right|^{2} + \dfrac{P_{n}}{P_{s}(u,v)}} \tag{26}$$

where $H(u,v)$ and $H^*(u,v)$ are the low-pass filter and its complex conjugate in the frequency domain, $P_s(u,v)$ is the power spectrum of the signal, and P_n is the average amplitude of noise frequencies; the term $\dfrac{P_n}{P_s(u,v)}$ is the reciprocal of the signal-to-noise (S/N) ratio.

In this paper, the SEM image of the region of interest was taken using parameters of 30 keV and spot size 1. Given this information, the noise level could be calibrated using the method proposed by Bi et al. [47]. The magnitude of P_n was estimated to be 1465. Then, the Wiener filter was set. Figure 4-8(c) shows an FFT image of the Wiener filter according to $R(u,v) = \dfrac{H^*(u,v)}{\left|H(u,v)\right|^2 + \dfrac{1465}{P_s(u,v)}}$.

(a)   (b)

(c)

(d)

(e)

(f)

(g)

(h)

(i)

(j)

(k)

(l)
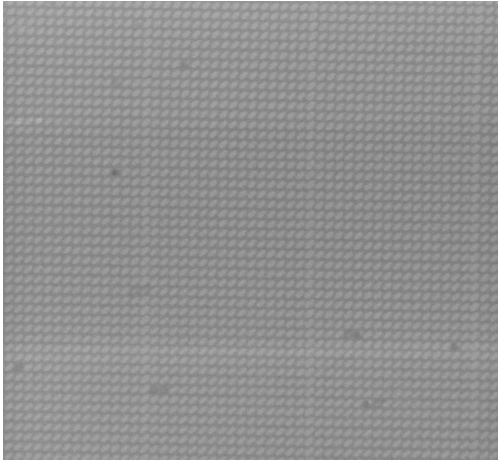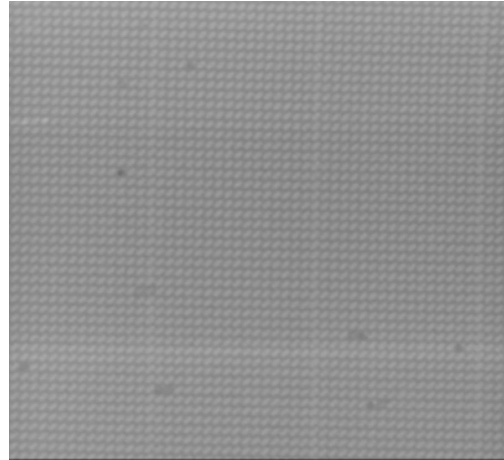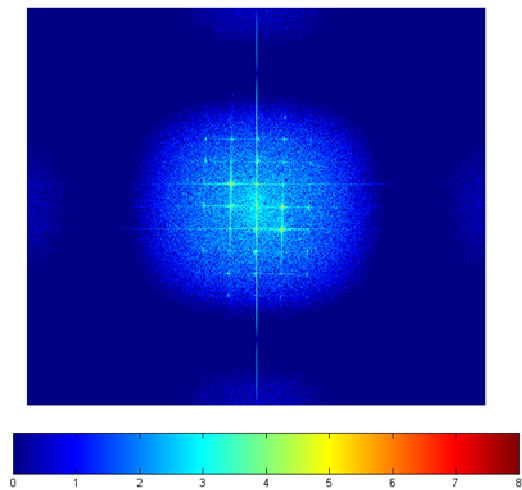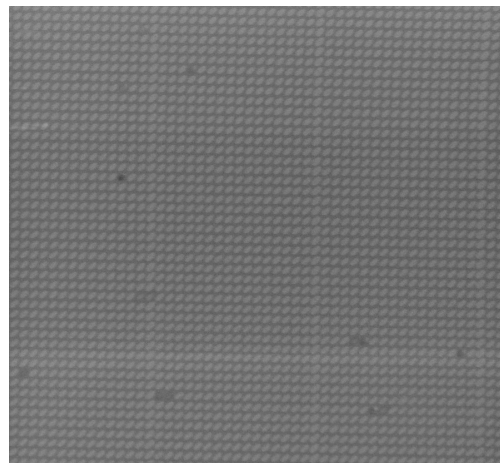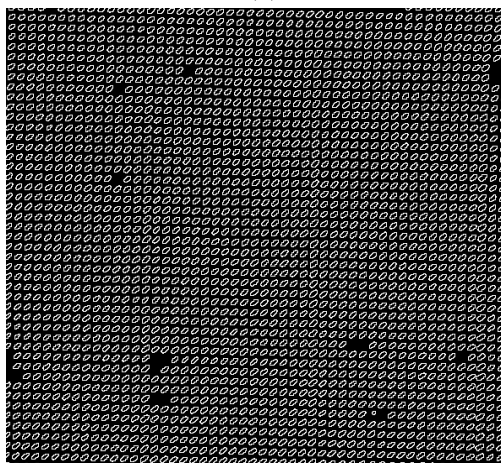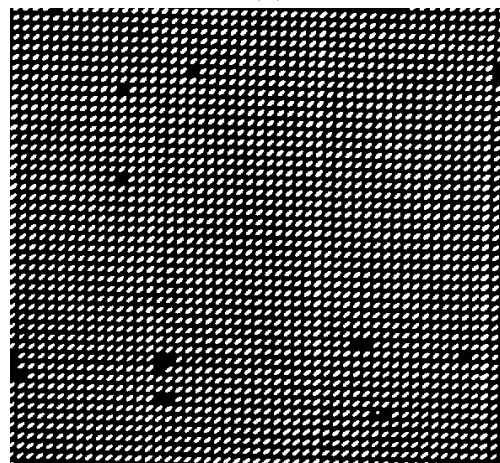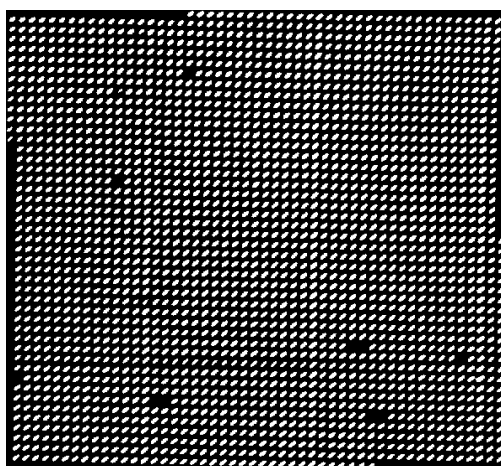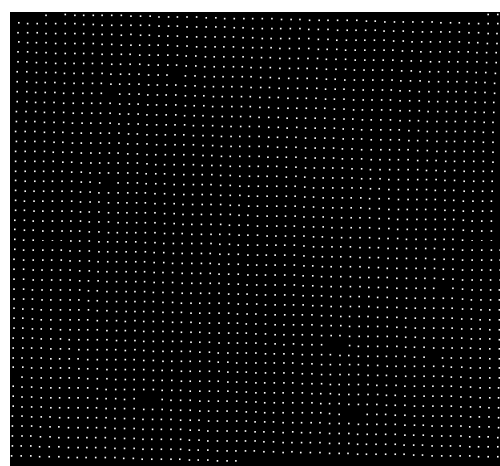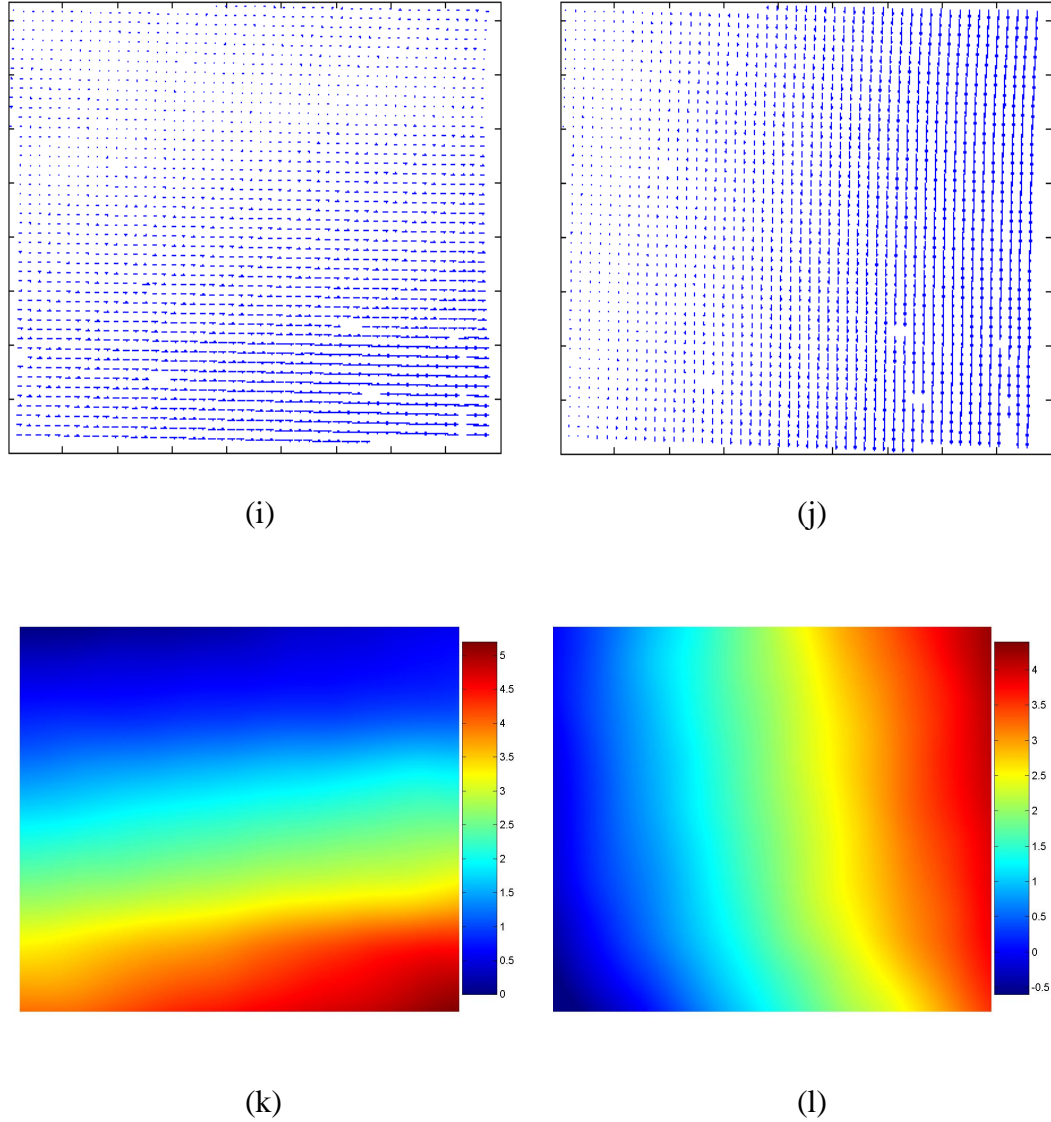
Figure 4-8 Experiment results (a) Original SEM image of region of interest, (b) Image processed by low-pass filter, (c) FFT image of de-blurring filter, (d) Image processed by de-blurring filter, (e) Boundary detection, (f) Binarization, (g) Removal of partial patterns along the boundaries, (h) Pattern recognition and center coordinate detection, (i) Horizontal discrete displacement field, (j) Vertical discrete displacement field, (k) Displacement plot in horizontal direction, (l) Displacement plot in vertical direction

The image processed by the Wiener filter is shown in Figure 4-8(d). The random noise reduction and the restoration of the boundary described in the previous section are evident.

The process proceeded for pattern recognition and center coordinate detection. The results obtained from the deformed pattern (Figure 4-8d) are shown in Figure 4-8(e) for boundary detection, Figure 4-8(f) for binarization by filling the detected boundary, Figure 4-8(g) for removal of partial patterns along the boundaries, and Figure 4-8(h) for pattern recognition and center coordinate detection.

The discrete displacement values were obtained at each individual pattern using the center coordinates of the images before and after thermal loading. The results are shown in Figures 4-8(i) and (j) for the horizontal (x) and vertical (y) displacement fields, respectively, where the magnitude of the vector is proportional to the length of the arrows.

Continuous displacement fields are also obtained using thin-plate interpolation. For better visibility, Figures 4-18(k) and (l) show the displacement plot.

4.5 Numerical Validation

A method is required to validate the experiment. There is no experimental method that is able to provide the displacement measurement with similar accuracy/sensitivity and spatial resolution. To examine the accuracy, we have carried out modeling of the elastic strains using the finite element method since the field of view only contains elastic strain.
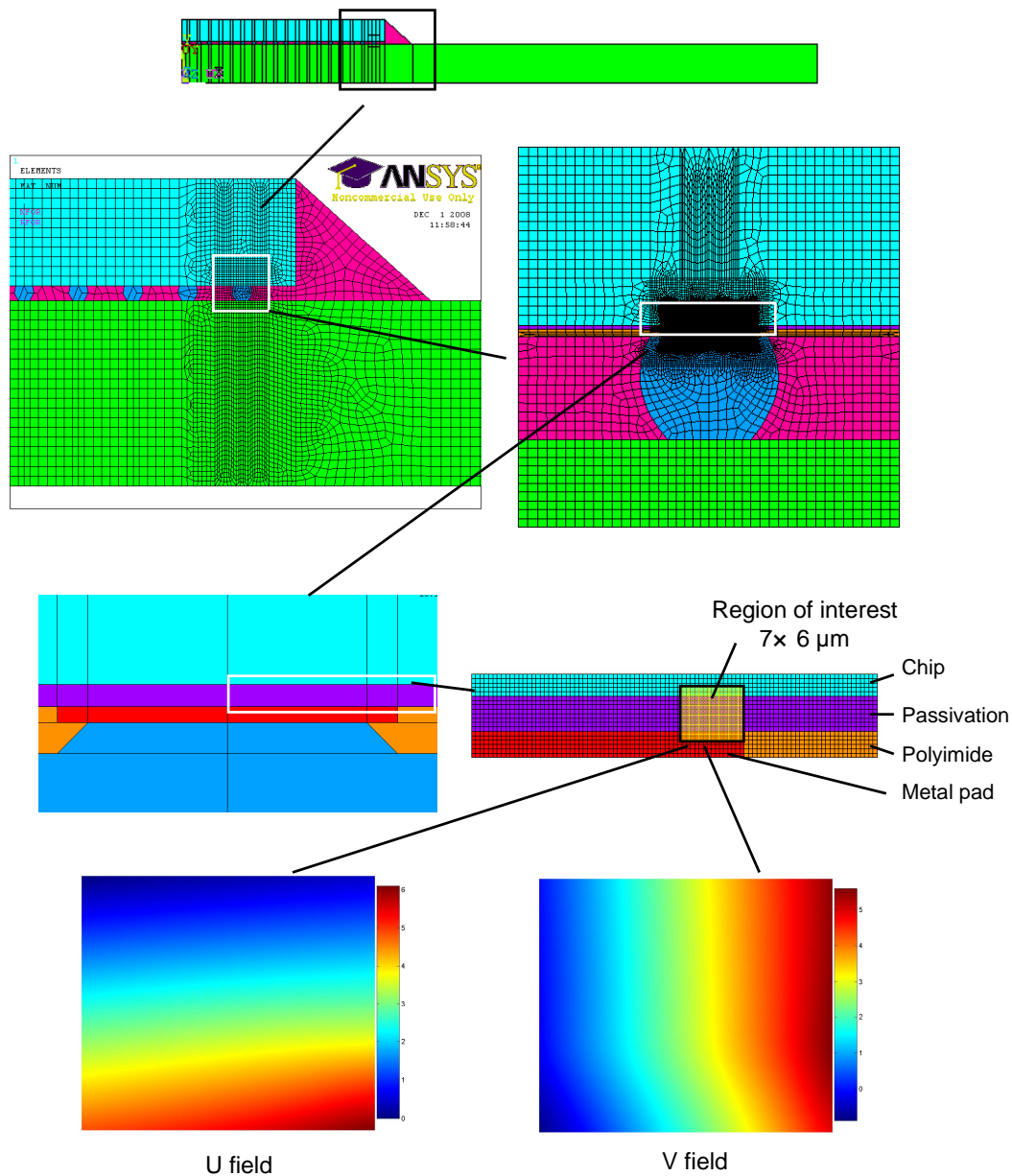
Figure 4-9 Finite element modeling results

In order to accommodate the very small region of interest (7×6μm) within the package structure, a global-local modeling scheme was employed. A 2-D global

model of the entire package was first solved and the result was used as boundary conditions of a local model of the region of interest.   In the local model, the mesh size was 400 nm.   Material properties used in the model are listed in Table 4-1. The temperature loading identical to the experiment ($\Delta T = 85°C$) was applied to the model.   Figure 4-9 shows the result of the local model.

Table 4-1. Material properties used in the finite element model [77]

	E (GPa)	ν	CTE (ppm/°C)
Si	160	0.23	2.6
SiO$_2$	68	0.19	0.75
Al	73	0.35	23
Solder	30.6 at 30°C 20.54 at 60°C 11.96 at 90°C 8.84 at 105°C	0.3	20
Underfill	4	0.3	40
Polyimide	4	0.35	21
Board	22	0.12	15

For better compassion between finite element modeling result and experiment result the displacement contours are shown in Figure 4-10.   The contour interval is 1.5nm/contour.   From the results shown in Figure 4-10, the excellent agreement between the finite element modeling results and experimental results is observed.
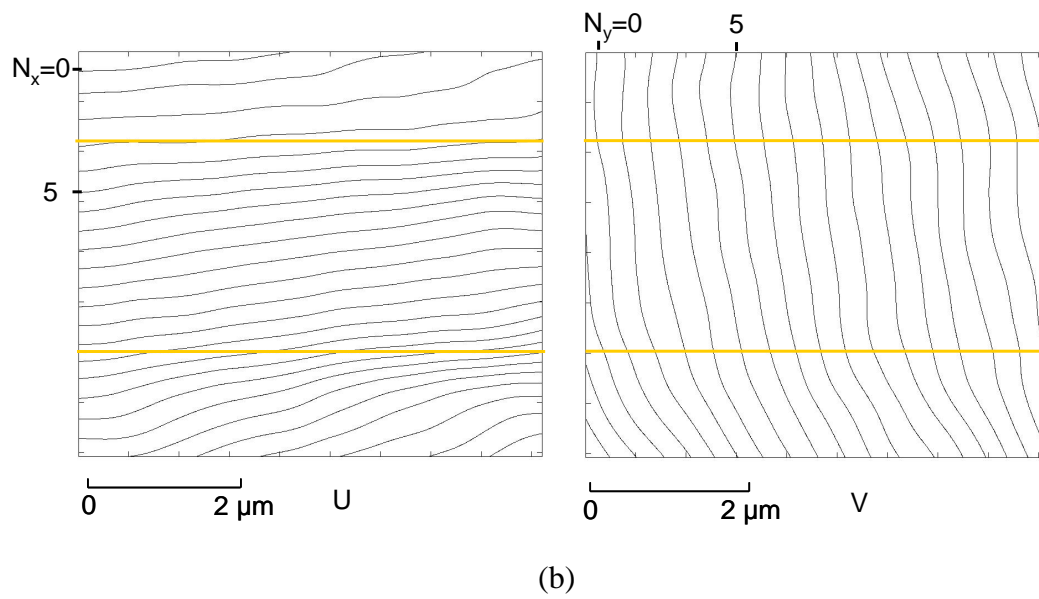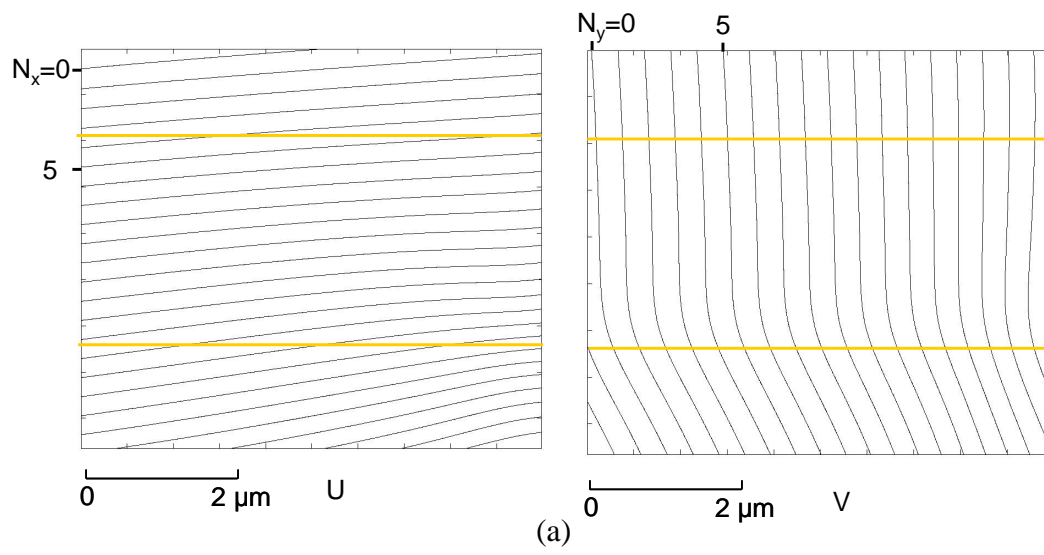
Figure 4-10 Displacement contour (a) finite element modeling results (b)

experimental result

For a quantitative comparison, the strain profiles along the highlighted line AA' in Figure 4-11(a) is calculated.

(a)   (b)

(c)   (d)
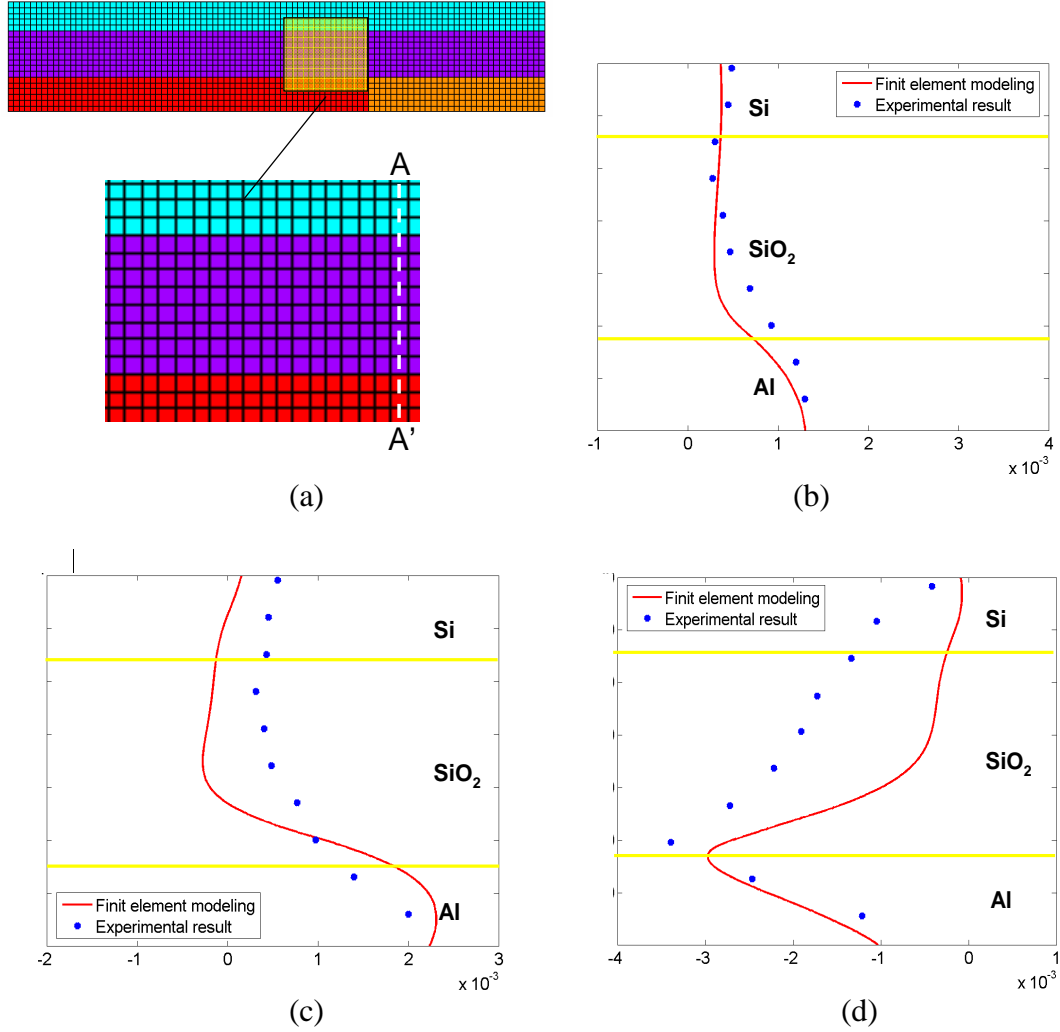
Figure 4-11 (a) Structure of region of interest (b) normal strain ε_x profile along AA' (c) Normal strain profile ε_y along AA'. (d) Shear strain profile γ_{xy} along AA'

Normal strain profiles in horizontal and vertical directions are comparable (Figure 4-11 b and c). In Figure 4-11(d) the shear strain concentration in the passivation layer/metal pad interface is obtained in both FEA modeling result and experimental result. This excellent match validates the experiment.

4.6 Discussion: Displacement Measurement Accuracy/Sensitivity Analysis

Displacement measurement accuracy was analyzed using computer-simulated ideal patterns, for which the units are pixels (refer to Reference [63]). The reference image and deformed image are simulated based on ideal patterns (refer to the insert of Figure 4-12) and theoretical displacement information. Using N-PRCT, displacement can be measured using the reference image and deformed image. Thus, the displacement measurement accuracy/sensitivity δ (in pixel) was obtained through comparing the theoretical displacement with measured displacement. By converting the pixel into physical dimensions (multiplying by spatial resolution), the displacement measurement accuracy for a given size of region of interest can be obtained.

The application used in the paper had a region of interest of about 7 μm (in the horizontal direction). The number of pixels in the digital image was 1024 pixels. Using Equation 27, the spatial resolution was determined as $R_s = 6.8 nm/pixel$. Figure 4-12 shows a summary of the accuracy plot for the region of interest of 7 μm (in the horizontal direction). The pattern size and the gauge length were $d_p = 115 nm$ and $L_g = 135 nm$, respectively; therefore, the corresponding

displacement accuracy is $\delta = 0.105\,nm$, and approximately 55 data points can be obtained per line.
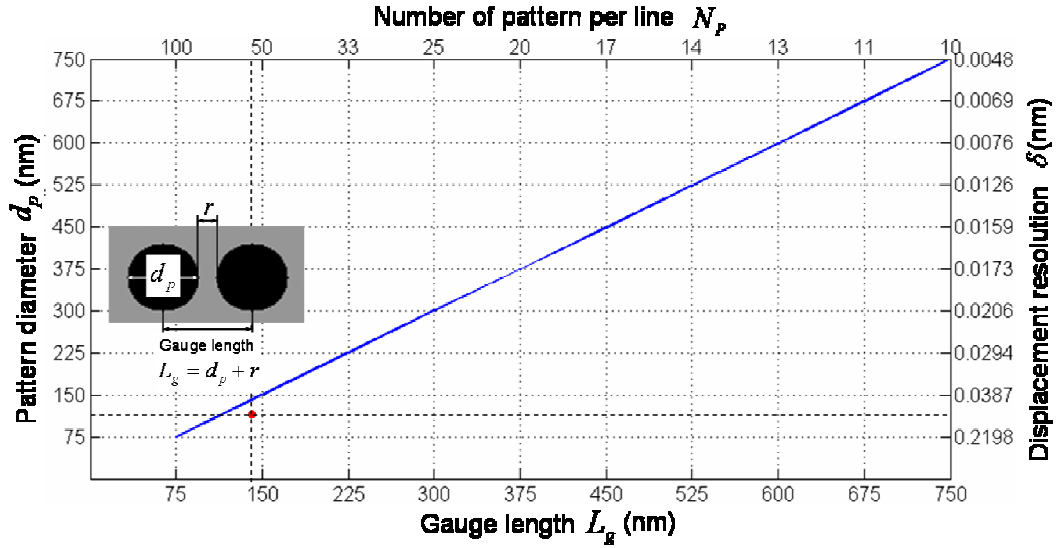
Figure 4-12 Displacement measurement accuracy/sensitivity plot for experiment

4.7 Conclusions

Using the proposed unique practice of E-beam lithography technique, regularly oriented patterns of about 115 nm in diameter were successfully fabricated on the well-polished specimen cross-section. N-PRCT was then implemented to document the displacement in a 7μm ✕ 6μm region of interest for a flip-chip package. Excellent deformation in the region of interest that is crossing the passivation layer is observed. The results show a shear strain concentration at the interface between the passivation layer and the adjacent metal pad. The experiment was validated using

100

finite element modeling method. And the displacement accuracy/sensitivity was about 0.105 nm with spatial resolution about 6.8 nm/pixel.

Chapter 5: Contributions and Future Work

5.1 Thesis Contributions

Full-field in-plane displacement measurement technique: nano-pattern recognition and correlation technique is developed to document the deformation of micro- to nano-structures. The most significant contributions of this work are summarized as follows:

1. Contributions to the experimental mechanics community:

(a) Development of a new experimental technique for deformation measurements of micro- to nano-scale structures. The proposed technique is able to document the deformation on a region of interest of a few microns with displacement measurement accuracy/sensitivity of fraction of nanometer.

(b) Application of the proposed technique to the deformation analyses of micro- and nano-mechanics.

2. Specific technical contributions:

(a) Development of the procedures to calibrate the SEM noise due to inherent instability of the electron beam column during scanning and the signal-to-noise ratio of the detector. This work enables a better understanding of the limitations for current available techniques proposed to document the deformation on small region of interest. More

importantly, this work enables a better understanding of requirements for the new measurement technique using SEM as imaging system.

(b) Propose a unique practice of E-beam lithography, which enables the fabrication of regularly oriented structure on specimen surface. This work utilizes the standard scanning electron microscope for imaging to fabricate the patterns without the need of special E-beam lithography system.

(c) Development of full-field in-plane displacement measurement technique: nano-pattern recognition and correlation technique. The regularly oriented structures are used as the media to realize the displacement measurement. The suitable combination of filters is identified; they are able to effectively eliminate the noise of digital images evolved during SEM imaging without losing clear object boundary features. This capability is obtained through fully understanding the image blurring mechanism and accurately calibrating the noise level of SEM imaging. The proposed N-PRCT technique is proved to be insensitive to the SEM noise. Therefore, combined with SEM, N-PRCT is capable of measuring the in-plane displacement on a few microns region of interest with displacement accuracy/sensitivity of fraction of nanometer.

5.2 Proposed Future Work

As mentioned above, enhancement of performance is the ever-existing effort in microelectronic field. Smaller feature size of transistors and higher density of

circuitry are the important factors to realize this. The deformation of microelectronic devices during manufacturing and operating will continue to be critical information for the reliability analysis. The contributions made by this thesis can be extended; some of which are summarized as followings:

(a) Operate N-PRCT technique on smaller (sub-micron) region of interest. N-PRCT is an amplitude-based displacement measurement technique. Theoretically, it has no limitations with imaging devices. Regularly oriented patterns with smaller size (tens of nanometers scale or less in diameter) are required to realize the deformation measurement on sub-micron region of interest. Therefore, the new pattern fabrication method is a direction to extend the work. A technique called electron beam projection lithography [75,76] can be considered.

(b) Develop a more advanced image processing algorithm to realize a higher displacement measurement accuracy/sensitivity. This can be achieved through the development of advanced noise elimination algorithm; which should be able to remove the noise very effectively from the original signal.

(c) Develop a user-friendly program interface. This will enable the data analysis process more easily and effectively.

Bibliography

1. Darveaux R., and Mawer A., "Thermal and Power Cycling Limits of Plastic Ball Grid Array (PBGA)," Proceedings of Surface Mount International, pp. 315–325 (1995)

2. Darveaux R., Banerji K., Mawer A., and Doddy G., "Reliability of Ball Grid Array Solder Joints," Ball Grid Array Technology J. H. Lau, ed., McGraw-Hill (1994)

3. Syed A., "A Review of Finite Element Methods for Solder Joint Analysis," B. Han, R. Mahajan and D. Barker, eds., Experimental/Numerical Mechanicsin Electronics Packaging, Vol. 1, Society for Experimental Mechanics,Bethel, CT (1997)

4. Han B., and Guo Y., "Thermal Deformation Analysis of Various Electronic Packaging Products by Moiré and Microscopic Moiré Interferometry," ASME J. Electron. Packag., Vol. 117, pp. 185–191 (1995)

5. Han B., Guo Y., Lim C., and Caletka D., "Verification of Numerical Models Used in Microelectronics Packaging Design by Interferometric Displacement Measurement Methods," ASME J. Electron. Packag., Vol. 118, pp. 157–163 (1996)

6. Han B., and Guo Y., "Determination of Effective Coefficient of Thermal Expansion of Electronic Packaging Components: A Whole-field Approach," IEEE Transactions on Components, Packaging and Manufacturing Technology-Part A, Vol. 19, pp. 240-247, (1996)

7. Han B., Chopra M., Park S., Li L., and Verma K., "Effect of Substrate CTE on Solder Ball Reliability of Flip-Chip PBGA Package Assembly," Journal of Surface Mount Technology, Vol. 9, pp. 43–52 (1996)

8. Han B., "Deformation Mechanism of Two-Phase Solder Column Interconnections Under Highly Accelerated Thermal Cycling Condition: An Experimental Study," ASME J. Electron. Packag., Vol. 119, pp. 189–196 (1997)

9. Han B., and Guo Y., "Photomechanics Tools as Applied to Electronic Packaging Product Development," B. Han, R. Mahajan and D. Barker, eds., Experimental/Numerical Mechanics in Electronics Packaging, Vol. 1, Society for Experimental Mechanics, Bethel, CT. (1997)

10. Han B., "Recent Advancement of Moiré and Microscopic Moiré Interferometry for Thermal Deformation Analyses of Microelectronics Devices," Exp. Mech., Vol. 38, pp. 278–288 (1998)

11. Cho S., Han B. and Joo J., "Temperature Dependent Deformation Analysis of Ball Grid Array Package Assembly under Accelerated Thermal Cycling Condition,"

Journal of Electronic Packaging, Transaction of the ASME, Vol. 126, pp. 41-47 (2004).

12. Dally, J.W. and Read, D.T., "Electron-beam Moiré," Experimental Mechanics, Vol. 33, pp. 270-277 (1993)

13. Read D.T. and Dally J.W., "Theory of Electron Beam Moiré", Journal of Research of the National Institute of Standards and Technology, Vol. 101, No. 1, pp. 47-61 (1996)

14. Chen H. and Liu D. "Advances in Scanning Electron Microscope Moiré", Experimental Mechanics, Vol. 41,   pp. 165 – 173 (2001)

15. Xie H., Liu Z., Fang D., Dai F., Gao H. and Zhao Y., "A study on the digital nano-moiré method and its phase shifting technique", Meas. Sci. Technol. Vol. 15, pp. 1716–1721 (2004)

16. Xing Y., Kishimoto S., and Shinya N. "Multiscanning Method for Fabricating Electron Moiré Grating", Experimental Mechanics, Vol. 44, pp. 562-566 (2004)

17. Post, D. Han, B. and Ifju, P., "High sensitivity Moire: Experimental Analysis for Mechanics and Materials", Springer-Verlag, New York (1994)

18. Lu H. and Cary P.D., "Deformation Measurements by Digital Image Correlation: Implementation of a Second-order Displacement Gradient", Experimental Mechanics, Vol. 40, pp. 393-400 (2000)

19. Sutton, M.A., McNeill S. R., Helm J. D. and Chao Y. J., "Advances in Two-Dimensional and Three-Dimensional Computer Vision", Photomechanics, Topics Appl. Phys. Vol. 77, pp. 323–372 (2000)

20. Chen, J., Xia, G., Zhou, K., Xia, G., Qin, Y., "Two-step digital image correlation for micro-region measurement", Optics and Lasers in Engineering, Vol. 43, pp. 836-846 (2005)

21. Rugar D., H. J. Mamin, and P. Guethner. "Improved Fiber-optic Interferometer for Atomic Force Microscopy". Appl. Phys. Lett. Vol.55 (25), pp. 2588-2590 (1989)

22. Meyer E., "Atomic Force Microscopy". Prog. Surf. Sci. Vol.41 (1), pp. 3-49, (1992)

23. Betzig E. and J. K. Trautman. "Near-field Optics: Microscopy, Spectroscopy, and Surface Modification Beyond the Diffraction Limit". Science Vol. 257, pp.189-195 (1992)

24. Silva T. J., Schultz S., and Weller D.. "Scanning Near-Field Optical Microscope for the Imaging of Magnetic Domains in Optically Opaque Materials." Appl. Phys. Lett. Vol.65 (6), pp. 658-660 (1994).

25. Flegler S.L., J.W. Heckman, K.L. Klomparens, "Scanning and Transmission Electron Microscopy: An Introduction,", Oxford Univ. Press (1993)

26. Ludwig Reimer, P.W. Hawkes, "Scanning Electron Microscopy : Physics of Image Formation and Microanalysis", Springer; 2 edition (1998)

27. Hung P. and Voloshin A. S., "In-plane Strain Measurement by Digital Image Correlation", J. of the Braz. Soc. of Mech. Sci. & Eng., Vol. XXV, No. 3, pp. 215-221 (2003)

28. Cho S., Chasiotis I. , Friedmann T. and Sullivan J. P., "Young's modulus, Poisson's ratio and failure properties of tetrahedral amorphous diamond-like carbon for MEMS devices", J. Micromech. Microeng. Vol. 15 pp. 728-735 (2005)

29. Vendroux G., Knauss W. G., "Submicron Deformation Field Measurements: Part I, Developing a Digital Scanning Tunneling Microscope", Experimental Mechanics, Vol. 38, pp. 18-25 (1998).

30. Vendroux G., Knauss W. G., "Submicron Deformation Field Measurements: Part II, Improved Digital Image Correlation," Experimental Mechanics, Vol. 38, pp. 86-92, (1998).

31. Vendroux G., Knauss W. G., "Submicron Deformation Field Measurements: Part III, Demonstration of Deformation Determination," Experimental Mechanics, Vol. 38, pp. 154-160, (1998)

32. Zhu Y., Francois B., Paul E. L., Nicolaie M., and Horacio D. E., "Nanoscale Displacement and Strain Measurement", Proceedings of the 2003 SEM Annual Conference and Exposition on Experimental and Applied Mechanics, June 2-4, Charlotte, North Carolina, Session 77, Paper 155, (2003)

33. Collette S., Sutton M., Miney P., Reynolds A., Li X., Colavita P., Scrivens W., Luo Y., Sudarshan T., Muzykov P., and Myrick M., "Development of patterns for nanoscale strain measurements: I. Fabrication of imprinted Au webs for polymeric materials," Nanotechnology, Vol. 15, pp.1812-1817 (2004).

34. Sutton M., Li N., Garcia D., Cornille N., Orteu J., McNeill S., Schreier H., and Li X., "Metrology in a scanning electron microscope: Theoretical developments and experimental validation," Measurement Science and Technology, Vol. 17, pp. 2613-2622 (2006).

35. Li N., Sutton M., Li X., and Schreier H., "Full-field Thermal Deformation Measurements in a Scanning Electron Microscope by 2D Digital Image

Correlation," Experimental Mechanics, Experimental Mechanics, Vol. 48, pp.635-646 (2008)

36. Sutton M., Li N., Joy D., Reynolds A., Li X., "Scanning Electron Microscopy for Quantitative Small and Large Deformation Measurements Part I: SEM Imaging at Magnifications from 200 to 10,000," Experimental Mechanics, Vol.47, pp.775–787 (2007)

37. Sutton M., Li N., Garcia D., Cornille N., Orteu J., McNeill S., Schreier H., Li X. and Reynolds A., "Scanning Electron Microscopy for Quantitative Small and Large Deformation Measurements Part II: Experimental Validation for Magnifications from 200 to 10,000," Experimental Mechanics Vol.47, pp. 789–804 (2007)

38. Lagattu F., Bridier F., Villechaise P., and Brillaud J., "In-plane strain measurements on a microscopic scale by coupling digital image correlation and an in situ SEM technique," Materials Characterization, Vol. 56, pp. 10-18 (2006)

39. Sabate N., Vogel D., Gollhardt A., Marcos J., Gracia I., Cane C., and Michel B., "Digital image correlation of nanoscale deformation fields for local stress measurement in thin films," Nanotechnology, Vol. 17, pp. 5264-2270 (2006).

40. Schreier H., Garcia D., and Sutton M., "Advances in light microscope stereo vision," Experimental Mechanics, Vol. 44, pp. 278-288 (2004).

41. Chen D., Chiang F., Tan Y., and Don H., "Digital speckle-displacement measurement using a complex spectrum method", Appl. Opt, Vol. 32, pp. 1839-1849 (1993)

42. Chang S., Chiang F., and Guo Y.," Measurement of thermal deformation of interconnect layers using SIEM," Journal of Electronic Packaging, Transactions of the ASME, Vol. 124, pp. 310-313 (2002)

43. Mermer C., Kim D., and Kim Y., "Efficient 2D FFT implementation on mediaprocessors," Parallel Computing, Vol. 29, pp. 691-709 (2003)

44. Lee S., Mitchell D., Trofin L., Nevanen T., Soderlund H., and Martin C., "Antibody-based bio-nanotube membranes for enantiomeric drug separations," Science, Vol. 296, pp. 2198-2200 (2002).

45. Timoshenko S., and Goodier J., "Theory of Elasticity," McGraw-Hill (1970).

46. Sutton M., Garcia D. and McNeill S., "Introduction to Digital Image Correlation: Theory and Practice", Workshop material, 2004 Society for Experimental Mechanics Annual Conference on Experimental and Applied Mechanic (2004).

47. Bi H. and Han B., "On the Effect of SEM Noise at Extreme Magnifications on the Accuracy of Displacement Fields Obtained by DIC," Experimental Mechanics, (submitted for publication in July 2008).

48. Lee, S., Mitchell D., Trofin L., Nevanen T., Soderlund H., and Martin C., "Antibody-based bio-nanotube membranes for enantiomeric drug separations," Science. Vol. 296, pp. 2198–2200 (2002).

49. David T., Lee S., Trofin L., Li N., Nevanen T., Soderlund H. and Martin C., "Smart Nanotubes for Bioseparations and Biocatalysis," J. Am. Chem. Soc., Vol. 124. pp. 11864-11865 (2002).

50. Watson K., "A 2D FFT filtering program for image processing with examples," U.S. Dept. of the Interior, Geological Survey (1992).

51. Gonzalez R., Woods R., "Digital image processing", Addison-Wesley Pub, (1992)

52. Blanchet G., and Charbit M., "Digital Signal and Image Processing using MATLAB," ISTE Ltd, 2006.

53. Ma W., and Manjunath B., "EdgeFlow: a technique for boundary detection and image segmentation," IEEE Transactions on Image Processing, Vol.9, pp. 1375-1388 (2000)

54. Wang S., Ge F., and Liu T., "Evaluating edge detection through boundary detection," Eurasip Journal on Applied Signal Processing, Vol. 2006, pp. 1-15 (2006)

55. Guo Z., Richard W., "Parallel thinning with two-subiteration algorithms," Communications of the ACM, Vol. 32, pp. 359–373 (1989).

56. Murli A., D'Amore L., Simone V., "The Wiener Filter and Regularization Methods for Image Restoration Problems," ICIAP, pp. 394-401 (1999)

57. Tan S., Young C., Budgett D., Richardson J., Chatwin C., "A pattern recognition Wiener filter for realistic clutter backgrounds," Optics Communications, Vol. 172, pp. 193-202 (1999)

58. Oshiki, M., Shinomura, R., Mitake T. Sakurai T. Matasuura S. and Harada J., "Boundary detection method for ultrasound diagnostic images using region-growing approach," Jpn. J. Appl. Phys., Vol. 43, pp. 4411-4416 (2004).

59. Hutchinson, M. F. "On thin plate splines and kriging," Computing Science and Statistics, Vol. 25. pp. 55-62 (1993).

60. Hutchinson, M. F. "Interpolation of Rainfall Data with Thin Plate Smoothing Splines - Part I: Two Dimensional Smoothing of Data with Short Range

Correlation," Journal of Geographic Information and Decision Analysis, Vol. 2, pp. 139-151 (1998).

61. Hutchinson, M. F., "Interpolation of rainfall data with thin plate smoothing splines: II analysis of topographic dependence," Journal of Geographic Information and Decision Analysis, vol. 2, pp. 152 -167 (1998).

62. Marchi C. San, Kouzeli M., Rao R., Lewis J.A., Dunand D.C., "Alumina–aluminum interpenetrating-phase composites with three-dimensional periodic architecture," Scripta Materialia, Vol. 49, pp. 861–866 (2003).

63. Bi H. and Han B., "Nano-Pattern Recognition and Correlation Technique for Sub-Nanometer Deformation Measurement – Part I: Basic Principles," Experimental Mechanics, (ready for submission)

64. Bi H., and Han B., "Nano-Pattern Recognition and Correlation Technique for Sub-Nanometer Deformation Measurement – Part II: Implementation for Thermal Deformation Measurements of Microelectronics Circuits", ready for submission, Journal of Strain Analysis for Engineering Design

65. Bi H., Hartsough C. and Han B., "Nano-Pattern Recognition and Correlation Technique for Nano-scale Deformation Measurement," Proceedings of IPACK 2007, IPACK2007-33717, Vancouver, British Columbia, Canada (2007).

66. Utsumi T., "Low energy e-beam proximity projection lithography," Proceedings of SPIE - The International Society for Optical Engineering 3676, pp. 117-125 (1999)

67. Verhaar R., Bartsen J., Dil J., Juffermans C., Klerk J., and Lifka H., "E-Beam Lithography For Sub-Micron MOS-Devices.," Microelectronic Engineering 3 (1985) 511-518.

68. Martiradonna L., Stomeo T., Giorgi M., Cingolani R., and Vittorio M., "Nanopatterning of colloidal nanocrystals emitters dispersed in a PMMA matrix by e-beam lithography" Microelectronic Engineering, Vol 83, pp. 1478-1481 (2006)

69. Salerno M., and Cingolani R., "High throughput electron beam lithography on insulating substrates for photonic devices," Journal of Micromechanics and Microengineering, Vol 17, pp. 2414-2419 (2007)

70. Product specification, SU-8 2000 Permanent Epoxy Negative PhotoresistPROCESSING GUIDELINES FOR:SU-8 2100 and SU-8 2150

71. Chen Y., Peng K., and Cui Z., "A lift-off process for high resolution patterns using PMMA/LOR resist stack," Microelectronic Engineering, Vo. 73-74, June 2004, pp. 278-281 (2004)

72. Product specification, "NANO PMMA and Copolymer"

73. Yasuda M., Morimoto K., Kainuma Y., Kawata H., and Hirai Y., "Analysis of Charging Phenomena of Polymer Films on Silicon Substrates under Electron Beam Irradiation," Japanese Journal of Applied Physics, Vol. 47, pp. 4890−4892 (2008)

74. Ren L., and Chen B., "Proximity effect in electron beam lithography," 7th International Conference on Solid-State and Integrated Circuits Technology Proceedings, ICSICT pp. 579-582 (2004)

75. Nam S., Lee T., Wi J., Lee D., Lee H., Jin K., Lee M., Kim H., and Kim K., "Electron-beam lithography patterning of Ge2Sb2 Te5 nanostructures using hydrogen silsesquioxane and amorphous Si intermediate layer," Journal of the Electrochemical Society, Vol. 154, pp. 844-847 (2007)

76. Lee H., Kim B., Kim H., Wi J., Nam S., Jin K., Arai Y., and Kim K., "Electron beam projection nanopatterning using crystal lattice images obtained from high resolution transmission electron microscopy," Advanced Materials, Vol. 19, pp. 4189-4193 (2007)

77. Ochiai M., Akamatsu T. and Ueda H., "Reliability of Solder Joint Assembled with Lead Free Solder," Fujitsu Sci. Tech. J., Vol. 38, No. 1, pp. 96-101 (2002)